

Dissertation

**Remote ion traps for quantum networking:
Two-photon interference and correlations**

Felix Rohde

July 15, 2009

Prof. Jürgen Eschner
ICFO - The Institute of Photonic Science
Universitat Politècnica de Catalunya

Abstract

The field of quantum information processing (QIP) has evolved rapidly in the last decade. Strings of single trapped ions have proven to be one of the most promising candidates for the implementation of quantum information processing tasks such as universal gate operations or teleportation. Besides the challenge of scaling up these quantum processors to a larger number of ions, another important problem is to interconnect different processors on a macroscopic scale and integrate them into a quantum network.

This thesis describes the construction of a new experiment dedicated to the study of quantum communication and quantum networking with laser cooled single ions and first experiments carried out with it. Two linear Paul traps for $^{40}\text{Ca}^+$ have been set up at a distance of one meter. Two-photon interference of the fluorescence light of two remotely trapped single ions could be observed with a contrast of 80 %. This proves the suitability of the setup for the creation of remote entanglement, an important building block for quantum networking.

The first part of the thesis describes the experimental setup that was constructed from scratch. It consists of a newly designed trap apparatus and the laser setup. The apparatus was designed to fulfill the requirement of interferometric stability, which is a prerequisite for one remote entanglement protocol. Another important feature are two high numerical aperture in-vacuum lenses that optimize the collection efficiency of photons scattered by the ions. In order to frequency-stabilize the laser systems, a transfer stabilization scheme referenced to a transition in atomic Cs has been developed. The stabilization chain comprises low-cost open transfer cavities and offers very good long term stability.

The second part of the thesis presents the experimental results starting with the calibration of the two traps through excitation spectra. After that, the realization of two-photon interference from single ions under continuous excitation is presented. The model analysis of the data using eight level Bloch equations reveals the individual coherence properties of the interfering single photons. The coherence time of the fluorescence light does not exceed 20 ns, indicating that incoherent scattering is dominant.

An analysis of the efficiency of methods for remote entanglement relying on two-photon and single-photon interference, focussing on the role of the detection efficiency is discussed. It is revealed that single-photon schemes are more efficient if the detection efficiency is low (like in present experiments). The created setup is suitable for the realization of both types of protocols, based on single- and two-photon interference.

The conditioned dynamics of photon emission of a single ion are studied using correlation functions. The engineering of second order correlation functions used as a tool which relies on conditional dynamics, might have interesting applications in probabilistic quantum information processing.

Single-atom single-photon interfaces are an important application in quantum networks. As opposed to the emission of single photons by single atoms, the absorption of single photons by single atoms cannot be controlled in a similar way. With the future goal of realizing a heralded absorption of a single photon by a single atom, one of the ion traps was linked to a Spontaneous Parametric Down Conversion source. Quantum jump spectroscopy on a single ion using single photons from this source is shown.

Finally the reported two-photon interference could be extended also to pulsed excitation. This marks an important technological step towards remote entanglement.

Resumen

El campo de procesamiento de información cuántica (QIP por sus siglas en inglés) ha evolucionado rápidamente en la última década. Se ha demostrado que los iones individuales atrapados formando una cadenas son uno de los candidatos más prometedores para la ejecución de tareas de QIP, como pueden ser operaciones de tipo puerta lógica que sea universales o para realizar teletransportación cuántica. Además del desafío de aumentar el número de iones en estos procesadores cuánticos, otro problema importante es la interconexión de diferentes procesadores a escala macroscópica y la integración de ellos en una red cuántica.

Esta tesis describe la construcción de un nuevo experimento dedicado al estudio de las comunicaciones y redes de comunicación cuánticas usando iones individuales enfriados por láser y los primeros resultados obtenidos con él. Para ello se han construido dos trampas lineales de iones (Paul traps) para $^{40}\text{Ca}^+$ a una distancia de un metro. Mediante estas trampas, se ha podido observar la interferencia de dos fotones procedentes de la fluorescencia de los dos iones atrapados en lugares distantes con un contraste del 80 %. Esto demuestra la idoneidad del aparato construido para la generación de entrelazamiento a distancia, un elemento crucial para la construcción de redes cuánticas.

La primera parte de la tesis describe el desarrollo del experimento, que se empezó a construir desde cero. La trampa de iones se basa en un diseño novedoso. La descripción del sistema de láseres para operar la trampa completa esa primera parte de la tesis. Todo el diseño se realizó teniendo en cuenta los requisitos de estabilidad interferométrica necesarios en un protocolo de entrelazamiento a distancia. Otra característica importante son dos lentes de alta apertura numérica instaladas en la cámara de vacío que optimizan la eficiencia de colección de los fotones dispersados por los iones. Con el fin de estabilizar la frecuencia del sistema de láseres, se desarrolló un sistema de transferencia de estabilización referenciado mediante una transición de átomos de Cs. La cadena de estabilización comprende cavidades abiertas de transferencia de bajo coste y ofrece muy buena estabilidad a largo plazo.

La segunda parte de la tesis presenta los resultados experimentales comenzando con la calibración de las dos trampas a través de los espectros de excitación. Acto seguido se presentan los datos de la interferencia de dos fotones provenientes de iones individuales bajo excitación continua. El análisis de estos datos mediante ecuaciones de Bloch de ocho niveles revela las propiedades individuales de coherencia de los fotones que interfieren. El tiempo de coherencia de la luz de fluorescencia no excede los 20 ns, lo que indica que la dispersión incoherente es dominante.

En la tesis se analiza además la eficiencia de los métodos de entrelazamiento re-

moto, basados tanto en la interferencia de dos fotones como en la interferencia de fotones individuales, centrándose en el papel de la eficiencia de detección. Se pone de manifiesto que, si la eficiencia de detección es baja (como en los experimentos actuales) los esquemas con fotones individuales son superiores. El montaje experimental es adecuado para los dos tipos de protocolos, basados en interferencia de fotones individuales y de dos fotones.

La tesis estudia a su vez la dinámica condicional de la emisión de fotones por un ion individual utilizando funciones de correlación. La ingeniería de funciones de correlación de segundo orden utilizado como una herramienta que se basa en la dinámica condicional, podría tener aplicaciones interesantes en el procesado probabilístico de información cuántica.

Las interfaces de átomos y fotones individuales son una aplicación importante en redes cuánticas. La absorción de fotones individuales por átomos individuales no se puede controlar de manera similar al caso de la emisión. Con el objetivo futuro de realizar una absorción predeterminada de un fotón individual por un átomo individual, una de las trampas de iones se ha conectado con una fuente de fotones entrelazados. Esta fuente está basada en la creado por división de frecuencia paramétrica espontánea (SPDC, en sus siglas en inglés). Se presentan los resultados espectroscópicos de los saltos cuánticos de un ion individual mediante los fotones de esta fuente.

Por último, la interferencia de dos fotones aquí observada pudo ser ampliada también a un esquema de excitación pulsado. Esto marca un paso tecnológico importante hacia el entrelazamiento a distancia.

Contents

| | |
|---|-----------|
| 1. Introduction | 1 |
| 2. Paul Traps | 7 |
| 2.1. Linear Paul traps | 7 |
| 3. Characterization of frequency noise | 11 |
| 3.1. Time domain | 12 |
| 3.2. Allan variance | 13 |
| 3.3. Frequency domain | 13 |
| 4. Experimental setup | 17 |
| 4.1. Trap apparatus | 17 |
| 4.1.1. Trap design | 17 |
| 4.1.2. HALO Lenses | 19 |
| 4.1.3. Vacuum vessel | 20 |
| 4.1.4. Magnetic field coils | 24 |
| 4.1.5. Helical resonator | 26 |
| 4.1.6. Combined Setup | 29 |
| 4.2. Laser Setup | 34 |
| 4.2.1. Lasers | 34 |
| 4.2.2. Doppler-free saturated absorption spectroscopy | 35 |
| 4.2.3. Pound-Drever-Hall technique | 36 |
| 4.2.4. Stabilization scheme | 37 |
| 4.2.5. Cavities | 41 |
| 4.2.6. Cavity Locker | 42 |
| 4.2.7. Transfer lock | 45 |
| 4.2.8. Systematic errors | 48 |
| 4.2.9. Locking procedure | 51 |
| 4.2.10. Radio Frequency Drive | 53 |
| 4.2.11. Cs spectroscopy | 54 |
| 4.2.12. Characterization of the individual stabilizations | 56 |
| 4.2.13. Characterization of the transfer lock | 57 |

| | |
|---|------------|
| 5. Light-matter interaction | 67 |
| 5.1. The Ca ion | 67 |
| 5.2. Three level system interacting with two light fields | 69 |
| 5.3. Master equation | 71 |
| 5.4. Bloch equations | 72 |
| 5.5. Excitation spectra | 72 |
| 5.5.1. Dark resonances | 73 |
| 5.5.2. Eight-level system | 73 |
| 5.5.3. Modeling excitation spectra | 74 |
| 5.6. Correlation functions | 75 |
| 6. Preparation of the two traps | 79 |
| 6.1. Trapping procedure | 79 |
| 6.2. Micromotion compensation | 80 |
| 6.3. Excitation spectra | 82 |
| 7. Two-photon interference | 85 |
| 7.1. Introduction | 85 |
| 7.2. Theory | 87 |
| 7.3. Setup | 90 |
| 7.4. Experimental results | 91 |
| 8. Methods for remote entanglement | 95 |
| 8.1. One-photon schemes | 96 |
| 8.2. Two-photon schemes | 97 |
| 8.3. Comparison of one- and two-photon schemes | 97 |
| 9. Conditioned dynamics of photon emission | 101 |
| 9.1. Model | 103 |
| 9.2. Experiment | 108 |
| 10. Towards networking | 113 |
| 10.1. Single-ion single-photon interaction | 113 |
| 10.1.1. The Down-Conversion source | 114 |
| 10.1.2. Quantum jump spectroscopy | 116 |
| 10.2. Pulsed two-photon interference | 120 |
| 11. Summary and Outlook | 125 |
| A. Transmission of cavity mirrors | 129 |
| B. Practical advice | 131 |
| C. Matlab code for Allan variance | 133 |

| | |
|--|------------|
| D. Derivation of PDH fit function | 135 |
| E. Matlab codes for fit to PDH error signal | 137 |
| E.1. find_b0.m | 137 |
| E.2. $K(\omega, \Omega)$ | 137 |
| E.3. fit_PDH.m | 138 |
| E.4. slope.m | 139 |
| Bibliography | 141 |
| Acknowledgements | 153 |

1. Introduction

Quantum information science studies the information-processing capabilities of quantum systems. Richard Feynman was one of the first to propose the use of quantum systems to simulate quantum phenomena [1, 2]. He realized that a classical Turing machine would experience an exponential slowdown when simulating quantum phenomena, while his hypothetical universal quantum simulator would not. Feynman's ideas were developed further by David Deutsch, who in 1985 published a paper describing a universal quantum computer [3, 4]. Deutsch proved that a two-state system could be made to simulate any physical system by the use of a set of simple operations. Functionally similar to binary logical gates in classical computers, these operations became known as "quantum gates". Together with Richard Jozsa, Deutsch also found one of the first examples for a quantum algorithm, the Deutsch-Jozsa algorithm [5, 6], that is more efficient than any other classical algorithm in determining if a function is balanced or constant.

It took until 1994, when Peter Shor discovered an algorithm that is capable of factorizing large numbers with an exponential speed up compared to the best known classical protocol, until also experimental research got interested on a broad scale [7]. The realization of Shor's factoring algorithm would threaten public key encryption systems, wildly used in the transmission of sensitive information, for example by internet protocols or in bank transfers. Another very useful algorithm is a search algorithm found by Lov Grover [8]. It searches elements in unordered databases and offers a quadratical speedup over its classical counterpart.

Today it is generally acknowledged that entanglement is the crucial element that makes quantum computing more efficient than classical computing for these algorithms [9]. In an experimental realization of a quantum processor, the execution of algorithms is implemented by the controlled interactions between qubits. Inevitably the qubits also interact with their environment, since they can not be fully isolated while maintaining the coupling between them. This leads to decoherence that tends to destroy the information in the superposition states of a quantum computer, and thus makes long computations impossible.

For a realistic implementation of quantum computation, the discovery of quantum error correction by Andrew Steane [10] and Peter Shor [11] was thus vital. Quantum error correction works with the help of several ancilla qubits that are encoded with the same information as the logical qubit. By measuring the state of the ancilla qubits an appropriate correction for the logical qubit is found, thus making fault-tolerant quantum computing possible [12]. Recently a quantum gate with a fault-tolerant fidelity has been shown for the first time [13].

Many different possible physical realizations of a quantum computer are currently

1. Introduction

being investigated, and the elementary building blocks of such a device could already be demonstrated. The wide range of different candidates for the implementation of the qubit with matter starts with atomic systems like neutral atoms [14] or ions [15], or nuclear magnetic resonances in molecules [16, 17], and ends with solid-state implementations like superconducting Josephson junctions [18, 19], quantum dots [20, 21], or color centers. Each system has its own advantages regarding different aspects. The solid-state solutions have the advantage of better integration, but they exhibit rather short coherence times. Atomic qubits can have much longer coherence times and show near-ideal quantum behavior, thus they fulfill more easily the criteria for building a quantum computer. These five requirements are often referred to as "DiVincenzo Criteria" [22]:

1. A scalable physical system with well characterized qubits.
2. The ability to initialize the state of the qubits to a simple fiducial state, eg. $|000\dots\rangle$.
3. Long relevant decoherence times, much longer than the gate operation time.
4. A "universal" set of quantum gates.
5. A qubit-specific measurement capacity.

So far no other system fulfills these criteria as well as trapped, laser cooled ions. State initialization [23], readout [24, 25, 26] and long coherence times [27] had been demonstrated in metrology experiments, when Ignacio Cirac and Peter Zoller realized the potential of cold ions for Quantum Information Processing. Their proposal for the realization of a quantum computer relies on cold strings of ions that interact with laser beams. Quantum gates can be realized by coupling the ions through their collective quantized motion [28]. The first experimental implementation of a rudimentary "Cirac-Zoller-gate" could be shown during the same year [29]. This can be considered the beginning of QIP with cold ions.

From then on all of the fundamental building blocks of a quantum computer could be shown in different research groups and different ion species. Universal gate operation were shown using ${}^9\text{Be}^+$ in Boulder [30, 31, 32] and Michigan [33], and using ${}^{40}\text{Ca}^+$ in Innsbruck [34, 35] and Oxford [36]. The first teleportation of the quantum state of massive particles was realized simultaneously in Boulder and Innsbruck [37, 38]. The implementation of a quantum error correction protocol [39], state purification [40] and multi particle entanglement of up to eight ions [41, 42, 43] constitute other important achievements. Besides the mentioned Deutsch-Jozsa algorithm also Grover's search algorithm could be realized in 2005 [44].

It is clear that despite the enormous progress in the last years, the fidelity of gate operations has to be further increased in order to perform useful computations. Another remaining problem is the scalability of the ion approach. Although the number of ions in a strings trapped in a single harmonic well is in principle scalable, this is not very practical. Currently much effort is put into the development of

micro trap arrays in which ions could be moved around from interaction to storage zones [45, 46]. The biggest problem with this miniaturization of ion traps is the heating induced by the vicinity of the trap electrodes and shuttling of the ions. However, the obstacles to overcome in order to realize an array of fifty or hundred ions, a number that would be interesting for quantum simulations, are of mere technological nature. To summarize, the basic functionality of a quantum processor could be proven experimentally in the last years. The remaining task is to improve the basic building blocks and to integrate them into a single device.

A natural further goal after the realization of small scale quantum computing is to interconnect two quantum processors and build a macroscopic quantum network. Such a network could also be used for long distance quantum communication or cryptography. Since all requirements for an elementary quantum computer have been fulfilled with trapped ions, the next logical step is to construct the fundamental building blocks of such a quantum network with these systems. In order to account for this "networkability", the DiVincenzo criteria can be extended by two additional criteria [47]:

6. The ability to interconvert stationary and flying qubits

Some implementations of qubits are good quantum memories while long distance transmission of quantum information requires other physical systems. Furthermore, the architecture of a quantum computer might require the storing and processing of information at different places, like it happens in current digital computers, where the CPU processing the data and the hard drive used as a mass storage device are separated and distinct components. A working quantum computer may therefore involve distributed quantum computing within the architecture of one device. This can be seen as a local quantum network and leads to the next criteria.

7. The ability to faithfully transmit flying qubits between specified locations.

The faithful transmission of flying qubits is not only important for distributed quantum computing but also for long distance quantum communication and quantum key distribution [48, 49, 50, 51]. Trapped ions could be used as quantum memory for photonic flying qubits in cryptography applications. Quantum cryptography tasks involve only a few consecutive computational steps and alleviate thus the efforts to adequately compensate unwelcome decoherence effects. At present the main limitation of photon based quantum communication is the loss of photons in the quantum channel. This limits the bridgeable distance to about 100 km with present technology. A solution to this problem is to subdivide larger distances into smaller sections over which entanglement can be teleported. A quantum repeater situated at each of the nodes of the quantum network could then transfer entanglement over longer distances [52]. To accomplish this a fully coherent and efficient state transfer between flying and stationary qubits, as well as a faithful transmission between the specific locations is necessary. The joint European effort towards quantum information processing and communication is summarized in a strategic report that defines a road

1. Introduction

map for the goals of the next five to ten years [53]. The report states the development of quantum interfaces and repeaters as an integral part of full scale quantum information systems and identifies their realization as one of the most challenging tasks for the future. First progress was achieved using atomic ensembles as quantum memory [54, 55, 56, 57, 58]. Compared to ions these systems have the disadvantage of shorter coherence times.

The smallest building block of a quantum network would thus be a quantum repeater capable of teleporting information over a macroscopic distance. The essential resource for such a repeater is remote entanglement. To entangle two remote quantum systems is fundamentally different from ordinary entanglement, since the qubits usually do not interact with each other. Single trapped ions in one and the same trap for example, interact via coulomb repulsion which can be used to establish entanglement [37, 38]. This interaction is absent if the two ions are trapped in different trapping potentials.

To overcome this difficulty several probabilistic schemes for remote entanglement with atoms have been proposed. The proposals can be divided into schemes relying on single- and two-photon interference. In the first case, two indistinguishable scattering paths of a single photon interfere, such that its detection leads to entanglement of the atoms [59, 60]. In the latter case, coincident detection of two photons, each being entangled with one atom [61], projects the two atoms into an entangled state [62, 63, 64]. Remote entanglement using two-photon interference has very recently been established between two independently trapped $^{171}\text{Yb}^+$ ions [65, 66]. Furthermore, with the same setup quantum teleportation between distant matter qubits has been reported for the first time [67].

Besides the described applications for quantum information processing, another motivation for the presented experiments is to study fundamental interactions between quantum systems. Present technology offers the possibility to control the quantum dynamics of single atoms. It is of fundamental interest to explore these possibilities and push their limits, possibly discovering new applications. The interaction of single atoms and single photons is one of the most fundamental processes in our physical environment. Studying and controlling it under ideal lab conditions leads to a deeper understanding of the principles of this environment.

This thesis describes the construction and the first results of a new experiment that is designed to study the feasibility of quantum networks with single trapped $^{40}\text{Ca}^+$ ions. The work presented focuses on two different approaches towards quantum networking. On the one hand the double ion trap setup presented is constructed in a way that it allows for the realization of remote entanglement through single- as well as through two-photon interference. Although remote entanglement has been shown before, the perspective of realizing it with the only ion species for which fault tolerant gate operations have been shown so far [13], and using a possibly more efficient scheme relying on single-photon interference [68], justifies the effort of realizing it with $^{40}\text{Ca}^+$. And on the other hand, the use of high numerical aperture in vac-

uum lenses, that maximize the ion-photon coupling, allows to study single-photon single-ion interaction. This single-photon single-ion interface can be used for a future entanglement transfer from the photon-photon entanglement of a Spontaneous Parametric Down-Conversion source to the remote entanglement of two single ions in the two traps.

The report starts with a short introduction into the trapping principle of Paul traps (chapter 2) and into the statistical tools that are used to characterize the frequency stability of the laser system (chapter 3). In chapter 4 the experimental setup consisting of two parts, the trap apparatus and the laser setup, is described. Based partially on previously established technology [35], a new apparatus has been constructed with the goal of maximizing the collection efficiency of the scattered photons while at the same time permitting optimal optical access to the trap center. A laser stabilization scheme with an atomic reference, that is based on transfer cavities, was implemented. Chapter 5 introduces the theoretical background that is used for model calculations throughout the following chapters. Chapter 6 addresses the calibration procedures that are performed prior to any measurement. As proof for the suitability of the setup for the creation of remote entanglement, the observation of two-photon interference under continuous excitation is presented in chapter 7. Theoretical considerations about the efficiency of methods for remote entanglement are summarized in the following chapter (chapter 8). The investigation of conditional dynamics of photon emission from a single ion is presented in chapter 9. Chapter 10 reports on further experiments for quantum networking that have been accomplished. This comprises the observation of the absorption of a single photon by a single ion and the realization of pulsed two-photon interference. Finally chapter 11 gives an outlook on the experiments to be performed with the setup in the near future.

1. Introduction

2. Paul Traps

The first cage for ions and electrons was developed by Wolfgang Paul in the mid-50's while he was preparing the construction of a synchrotron [69]. The principle became known as Paul trap and was honored with the nobel price in 1989. Paul traps permitted for the first time to isolate few or single particles from their environment to study their properties [70].

Nowadays Paul traps play an important role in ultra high precision spectroscopy and are considered to be one of the most promising candidates for the implementation of quantum computation. A very general treatment of Paul traps can be found in [71].

The linear Paul trap used in our experiments is a slight variation of a design developed in the group of Rainer Blatt in Innsbruck. The details of this trap and ion traps in general have been described extensively in several publications [35, 72, 73, 74, 75, 76, 77]. Here the basic trapping mechanism necessary to understand the working principle will be described. The specifications of the trap apparatus are described in chapter 4.1.1.

2.1. Linear Paul traps

Ion traps achieve a very good decoupling of charged particles, including atoms and molecular ions, from their environment without altering the internal degrees of freedom. In linear Paul traps the rotational symmetry is broken in order to align the ions in a linear string. This allows for individual addressing of each ion which is necessary for some quantum information tasks.

The trapping potential is generated by two pairs of electrodes that are parallel to the trap axis (see figure 4.1). A rf potential U_{rf} is applied to two opposite electrodes while the other two are grounded. This gives rise to a two-dimensional radial quadrupole potential Φ , defined as

$$\Phi(x, y, z, t) = \frac{U_{rf}}{2r_0} \cos(\Omega_{rf} t)(x^2 - y^2). \quad (2.1)$$

Where Ω_{rf} is the radio frequency and r_0 the minimum distance from the trap axis to a trap electrode. The radio frequency is necessary because with electro static fields alone it is not possible to confine a charged particle in three dimensions. Theoretically this can be expressed by the Laplace equation

$$\Delta\Phi = 0. \quad (2.2)$$

2. Paul Traps

For a quadratic potential

$$\Phi = a_x x^2 + a_y y^2 + a_z z^2 \quad (2.3)$$

this yields the condition

$$2a_x + 2a_y + 2a_z = 0 \quad (2.4)$$

The potential can thus not be attractive in all directions. The solution is to create a quadrupole potential like 2.1 and to switch the polarity fast enough (with radio frequency), so that the ion effectively sees a harmonic potential.

The axial confinement is done by a static potential U_{cap} applied to two end tips on both ends of the trap (see fig. 4.1). Figure 4.1 shows only one of many possible realizations of this geometry [72, 75, 74].

The equations of motion of a charged particle in such a potential are given by the Mathieu equation

$$\frac{d^2x}{d\zeta^2} + (a - 2q \cos(2\zeta))x = 0 \quad (2.5)$$

$$\frac{d^2y}{d\zeta^2} + (a + 2q \cos(2\zeta))y = 0 \quad (2.6)$$

$$\frac{d^2z}{d\zeta^2} + 2az = 0, \quad (2.7)$$

where

$$\zeta = \frac{\Omega_{rf} t}{2}, \quad a = \frac{|e| \alpha U_{cap}}{m L^2 \Omega_{rf}^2}, \quad q = \frac{2 |e| U_{rf}}{m r_0^2 \Omega_{rf}^2}. \quad (2.8)$$

The numerical factor α (≈ 0.075 in our trap) depends on the trap geometry and L is the distance between the two end caps. Stable solutions of the equations of motion can be found in regions defined by the stability parameters a and q . Plotting a over q yields a stability diagram that reveals the possible trapping parameters for a given trap architecture. A stable solution refers to a stable trajectory of the particle in the potential. In the limit of $a, q^2 \ll 1$ and for a single ion, an effective harmonic pseudopotential, decoupling the axial and radial motion, is a good approximation [78]. In this regime the motion of an ion in the linear trap potential separates into a slower *secular motion* around the trap center and a superimposed faster *micro motion* driven by the radio frequency Ω_{rf} . It is possible to minimize the fast oscillations by the use of static potentials applied to additional compensation electrodes. Once the secular motion was reduced using lasercooling techniques, this static potentials move the ion to the minimum of the pseudopotential, where no micro motion is introduced. Micro motion shall therefore be neglected in the following.

The axial and radial trap frequencies in the harmonic pseudopotential read

$$\omega_z = \sqrt{\frac{|e| \alpha U_{cap}}{2mL^2}} \quad (2.9)$$

2.1. Linear Paul traps

and

$$\omega_r = \omega_x = \omega_y = \frac{\Omega_{rf}}{2} \sqrt{\frac{1}{2}q^2 - a}. \quad (2.10)$$

Interestingly, the factor a which strongly depends on the end cap voltage U_{cap} , influences the radial trap frequency and vice versa Ω_{rf} enters into ω_z . The higher U_{cap} is, the lower is the radial confinement. This defocussing effect [78] implies that U_{cap} should not be set too high with respect to the rf potential U_{rf} in order to maintain a one-dimensional trapping potential. The "pure" radial frequency can be found at very low end cap voltages ($U_{cap} \approx 0$)

$$\omega_{r0} = \frac{q\Omega_{rf}}{2\sqrt{2}}. \quad (2.11)$$

Whereas increasing the end tip voltage, the radial frequency reduces to

$$\omega_r = \sqrt{\omega_{r0}^2 - \frac{1}{2}\omega_z^2}. \quad (2.12)$$

Thus for $\omega_z \ll \omega_{r0}$ the defocussing is negligible and a linear trapping potential (more details in [75]) is achieved.

This section serves as introduction into the working principle of linear Paul traps. The definitions of the trap frequencies dependent on the trap dimensions and radio frequency parameters provide the theoretical background for the actual trap design presented in chapter 4.1.1. The next chapter introduces the statistical tools that are used to characterize the laser systems in chapter 4.2.13

2. Paul Traps

3. Characterization of frequency noise

Even the frequency of the most stable oscillator is not really constant in time but fluctuates. Many physical processes can influence the frequency and phase of an oscillator in a very complicated way. A big fraction of these processes are not under control of the experimenter and lead to fluctuations in time. In diode lasers, for example, the spontaneous emission of photons leads to random frequency fluctuations and thereby to a broadening of the linewidth. These unwanted irregular fluctuations can not be described by analytical functions. The statistical measures that have to be applied to understand and characterize the frequency noise in laser systems are treated in the following section. The formalism developed here follows the description in [79]. A reader interested in a more detailed treatment and further knowledge about frequency standards may find more information there.

The instantaneous electric output field of a diode laser can be written as follows

$$E(t) = [E_0 + \Delta E_0(t)] \cos(2\pi\nu_0 t + \phi(t)). \quad (3.1)$$

$\Delta E_0(t)$ and $\phi(t)$ represent random amplitude and phase fluctuations that are considered only small perturbations of the constant amplitude E_0 and phase $2\pi\nu_0 t$ of a perfect oscillator. Furthermore, it is assumed that no fluctuations are transferred from amplitude to phase and vice versa. It is convenient to define the instantaneous frequency

$$\nu(t) \equiv \frac{1}{2\pi} \frac{d\varphi(t)}{dt} = \frac{1}{2\pi} \frac{d}{dt}[2\pi\nu_0 t + \phi(t)] = \nu_0 + \frac{1}{2\pi} \frac{d\phi}{dt} \quad (3.2)$$

which differs from ν_0 by the derivative of the phase fluctuations

$$\Delta\nu(t) \equiv \frac{1}{2\pi} \frac{d\phi}{dt}. \quad (3.3)$$

For easier comparison between oscillators operating at different frequencies the instantaneous fractional (or normalized) frequency deviation is defined as

$$y(t) \equiv \frac{\Delta\nu(t)}{\nu_0} = \frac{dx(t)}{dt}. \quad (3.4)$$

Here $x(t) \equiv \frac{\phi(t)}{2\pi\nu_0}$ represents the normalized phase fluctuations and 3.3 has been used to derive the latter equation.

3. Characterization of frequency noise

3.1. Time domain

The fractional frequency deviation of a fluctuating quantity can be measured as a continuous function in time $y(t)$ or as a series of discrete readings y_i . The data set of discrete values y_i can for example be obtained by measuring $y(t)$ with a frequency counter. A sequence of measurements of duration τ reduces $y(t)$ to a discrete series of values averaged over τ ,

$$\bar{y}_i = \frac{1}{\tau} \int_{t_i}^{t_i + \tau} y(t) dt, \quad (3.5)$$

referred to as normalized frequency deviation. The experimental determination of \bar{y}_i averaged over the duration τ is described in chapter 4.2.13.

Because discrete data sets y_i coming from repeated measurements in general differ from each other, it is useful to analyze such data sets determining the mean value

$$\bar{y} = \frac{1}{N} \sum_{i=1}^N y_i \quad (3.6)$$

and standard deviation

$$s_y = \sqrt{\frac{1}{N-1} \sum_{i=1}^N (y_i - \bar{y})^2} = \sqrt{\frac{1}{N-1} \left[\sum_{i=1}^N y_i^2 - \frac{1}{N} (\sum_{i=1}^N y_i)^2 \right]}. \quad (3.7)$$

s_y is then a measure of the spread of the data set around the mean value \bar{y} .

If the fluctuations of $y(t)$ are the result of a statistical process and the mean value or variance are independent in time, then this spread evolves into a Gaussian probability density $p(y)$ for $T \rightarrow \infty$.

$$p(y) = \frac{1}{\sigma \sqrt{2\pi}} \exp \left(-\frac{(y - \bar{y})^2}{2\sigma^2} \right) \quad (3.8)$$

The denominator σ^2 denotes the variance

$$\sigma^2 = \int_{-\infty}^{\infty} (y - \langle y \rangle)^2 p(y) dy \quad (3.9)$$

and $\langle y \rangle$ the expectation value of the statistical process.

$$\langle y \rangle \equiv \int_{-\infty}^{\infty} y p(y) dy \quad (3.10)$$

With 3.9 and 3.10 the variance can be written as

$$\sigma^2 = \langle (y - \langle y \rangle)^2 \rangle = \langle y^2 - 2y\langle y \rangle + \langle y \rangle^2 \rangle = \langle y^2 \rangle - \langle y \rangle^2. \quad (3.11)$$

In practice only finite sequences of $y(t)$ can be measured. In that sense the mean value 3.6 is to be regarded as an estimate for the expectation value 3.10 of the Gaussian process and the square of the standard deviation 3.7 is an estimate of its variance σ^2 .

3.2. Allan variance

The use of mean value and standard deviation as discussed in the previous section is becoming problematic for data sets where adjacent data points are not independent from each other. This can be understood considering a set of data with random fluctuations superimposed with a slow long term drift. It is obvious that the data within each subset scatter less than the data of the whole set. Consequently also the calculated experimental standard deviation of any subset of this data will be smaller than the one calculated from the entire data set. The evaluation of standard deviations from different subsets can therefore deliver information about the existence of correlations in the data set. In other words, the adjacent data points are not fully independent from each other but are somehow correlated.

This problem can be circumvented by the use of the Allan variance [80, 81]. In contrast to the usual variance 3.11 from section 3.1, where the fluctuation of the data with respect to the mean is calculated, the Allan variance $\sigma_y^2(\tau)$ is based on the differences of adjacent frequency values.

$$\sigma_y^2(\tau) = \left\langle \sum_{i=1}^2 \left(\bar{y}_i - \frac{1}{2} \sum_{j=1}^2 \bar{y}_j \right)^2 \right\rangle = \frac{1}{2} \langle (\bar{y}_2 - \bar{y}_1)^2 \rangle \quad (3.12)$$

From the squared normalized frequency difference of two adjacent frequency values the mean is computed and divided by two. It is important that there is no dead time between the two subsequent measurements \bar{y}_i and \bar{y}_j , which are the time averages over the measurement time τ as defined in 3.5. The Allan variance is a function of this measurement time τ and is usually displayed as a graph rather than a single number. A low $\sigma_y^2(\tau)$ is a characteristic of a good oscillator stability over the measurement time τ . The fact that $\sigma_y^2(\tau)$ is normalized to the overall frequency makes it a suitable figure of merit for comparison of oscillators at different frequencies, such as for example frequency standards in the optical and the microwave domain.

3.3. Frequency domain

Like in equation 3.2 we can assume that the frequency of our laser is stable enough so that the instantaneous frequency deviates only slightly from the mean frequency in time

$$\Delta\nu(t) \equiv \nu(t) - \bar{\nu} \ll \bar{\nu} \quad (3.13)$$

The autocorrelation function of the frequency deviations is defined by the temporal average of the product of the frequency fluctuations $\Delta\nu(t)$ at the instant t with the frequency fluctuations $\Delta\nu(t + \tau)$ at the instant $t + \tau$.

$$R_\nu(\tau) \equiv \lim_{T \rightarrow \infty} \frac{1}{2T} \int_{-T}^T \Delta\nu(t + \tau) \Delta\nu(t) dt \quad (3.14)$$

3. Characterization of frequency noise

It can be interpreted as a measure of the distribution of $\Delta\nu(t)$. From the autocorrelation function $R_\nu(\tau)$ one can derive the power spectral density of the frequency deviations using the Wiener-Khintchine theorem [79]

$$S_\nu(f) = \int_{-\infty}^{\infty} R_\nu(\tau) \exp(-i2\pi f\tau) d\tau. \quad (3.15)$$

Using 3.4 and 3.15, the power spectral density of the fractional frequency deviations can be found as

$$S_y(f) = \frac{1}{\nu_0^2} S_\nu(f) \quad (3.16)$$

The power spectral density of phase fluctuations $S_\phi(f)$ is defined in a similar fashion. Frequency fluctuations are essentially the time derivative of the phase fluctuations 3.3. By comparison with 3.14 and 3.15 one obtains

$$S_\nu(f) = f^2 S_\phi(f). \quad (3.17)$$

And from 3.16 and 3.17 it follows that

$$S_y(f) = \left(\frac{f}{\nu_0}\right)^2 S_\phi(f). \quad (3.18)$$

The power spectral density can be easily measured in the laboratory. From measurements of $S_y(f)$ on various sources as quartz-crystals, masers, atomic frequency standards and other microwave oscillators it is known that the experimental results can be modeled quite well by the power law

$$S_y(f) = \sum_{\alpha=-2}^2 h_\alpha f^\alpha. \quad (3.19)$$

The exponent α takes integer values from $-2 \leq \alpha \leq 2$ and is characteristic for the kind of noise present in the signal. The constant h_α is a measure of the noise level.

The power spectral density describes the frequency fluctuations in the Fourier domain as the Allan variance does in the time domain. It is possible to convert from the Fourier-frequency domain to the time domain by the following expression

$$\sigma_y^2(\tau) = 2 \int_0^\infty S_y(f) \frac{\sin^4(\pi\tau f)}{(\pi\tau f)^2} df. \quad (3.20)$$

A detailed derivation of the above term can be found in [82, 79].

The power laws are classified using the classical terminology of "white noise" for noise whose spectral density is independent of f , "flicker noise" when it varies as f^{-1} and "random walk" when it varies with f^{-2} . In table 3.1 the different types of noise are listed together with their respective spectral densities, the corresponding

3.3. Frequency domain

| $S_y(f)$ | $S_\phi(f)$ | Type of noise | $\sigma_y^2(\tau)$ | τ^n |
|-----------------|-------------------------|--|---|--------------|
| $h_2 f^2$ | $\nu_0^2 h_2 f^0$ | White phase noise | $\frac{3h_2 f_h}{4\pi^2 \tau^2}$ | -2 |
| $h_1 f$ | $\nu_0^2 h_1 f^{-1}$ | Flicker phase noise | $\frac{h_1(1.038+3\ln 2\pi f_h \tau)}{4\pi^2 \tau^2}$ | ≈ -2 |
| h_0 | $\nu_0^2 h_0 f^{-2}$ | White frequency noise (Random walk phase noise) | $\frac{h_0}{2\tau}$ | -1 |
| $h_{-1} f^{-1}$ | $\nu_0^2 h_{-1} f^{-3}$ | Flicker frequency noise | $2 \ln 2 h_{-1}$ | 0 |
| $h_{-2} f^{-2}$ | $\nu_0^2 h_{-2} f^{-4}$ | Random walk of frequency noise | $\frac{2\pi^2 h_{-2} \tau}{3}$ | 1 |

Table 3.1.: Power laws of fractional frequency fluctuations $S_y(f)$ and phase fluctuations $S_\phi(f)$. The corresponding Allan variance $\sigma_y^2(\tau)$ holds for a low-pass filter with cut-off frequency f_h when $2\pi f_h \tau \gg 1$.

Allan variances and their dependence on τ . If the Allan variance is displayed in a double logarithmic plot, the exponent of τ corresponds to the slope of the variance vs. time.

In general, white and flicker noise are always present in electric components and show up either as phase or frequency modulation depending on if they originate from an external or in-loop component, respectively.

- Random walk frequency noise can be assigned to the environment of the oscillator. Common causes are temperature and pressure variations, vibration and shocks. Important for low frequencies.
- Flicker frequency noise is related to electronics and the environment but not yet fully understood. If this so-called $\frac{1}{f}$ noise is dominant, the linewidth depends strongly on the measurement time and the spectrum is Gaussian.
- White frequency noise arises from electronic elements inside the feedback loop of the oscillator, such as amplifiers. Thermal noise in components is a typical source. Spontaneous emission is also known to cause white frequency noise.
- Flicker phase noise is added again by noisy electronics such as output amplifiers or frequency multipliers.
- White phase noise is usually caused by white noise sources outside the feedback loop of the oscillator. It can be reduced by bandpass filtering the output signal.

The terminology developed here will be applied in the characterization of our diode laser system (chapter 4.2.13). The laser stabilization scheme, developed as part of this thesis, is presented at the end of the following chapter about the experimental setup.

3. Characterization of frequency noise

4. Experimental setup

The first part of this thesis describes the construction of the setup of two independent ion traps. The two linear traps, placed at a macroscopic distance of 1m, were build up from scratch and are intended to be used to study single-ion single-photon interaction, quantum networking and distant entanglement. The whole experimental setup can be divided into two areas, the trap apparatus and the laser setup. These two parts are described in this chapter. Due to the great extent of work and the high level of complexity that the construction of such a project imposes, it was pursued in a team, and some aspects are described in more detail in the reports of other team members [83, 84].

4.1. Trap apparatus

The two identical apparatuses consist each of a vacuum chamber, a linear Paul trap and two in-vacuum lenses. The experiment can be seen as a further development of earlier experiments with $^{138}\text{Ba}^+$ also involving high numerical aperture in-vacuum lenses [85]. The new design is also based on previous experiments with $^{40}\text{Ca}^+$ at the University of Innsbruck [75] and has been build in close cooperation with the group of Prof. Rainer Blatt [77]. Since one of the two vacuum chambers turned into a much darker color than the other one after the first bake out ($350\text{ }^\circ\text{C}$), the two devices will be referred to as "dark" and "bright" chamber, respectively.

4.1.1. Trap design

The design of the linear traps is almost identical to the one described in [75]. The original idea behind the design was to obtain a trade-off between down-scaling of the trap dimensions, in order to achieve high trap frequencies, and the best possible optical access. Only slight modifications concerning the compensation electrodes and the atomic ovens have been made. The trap consists of two endtips defining the trap axis and four blade electrodes which are arranged symmetrically around the axis (figure 4.1). The distance r_0 between trap axis and the blades is 0.8 mm, the distance between the two endtips L is 5 mm. The bright chamber is operated at a drive frequency of $\Omega_{rf}/2\pi = 26.4\text{ MHz}$ and the dark chamber at $\Omega_{rf}/2\pi = 25.792\text{ MHz}$ (see chapter 4.1.5).

With the Innsbruck trap [75], radial trap frequencies of $\omega_{r0} = 4.35\text{ MHz}$ with 12 W of RF power and a drive frequency of 23.4 MHz could be achieved. With equation 2.11 the stability parameter can be found to be approximately $q \approx 0.5$. The amplitude of the RF field is thus $U_{rf} = 1500\text{ V}$. The axial trap frequency could

4. Experimental setup

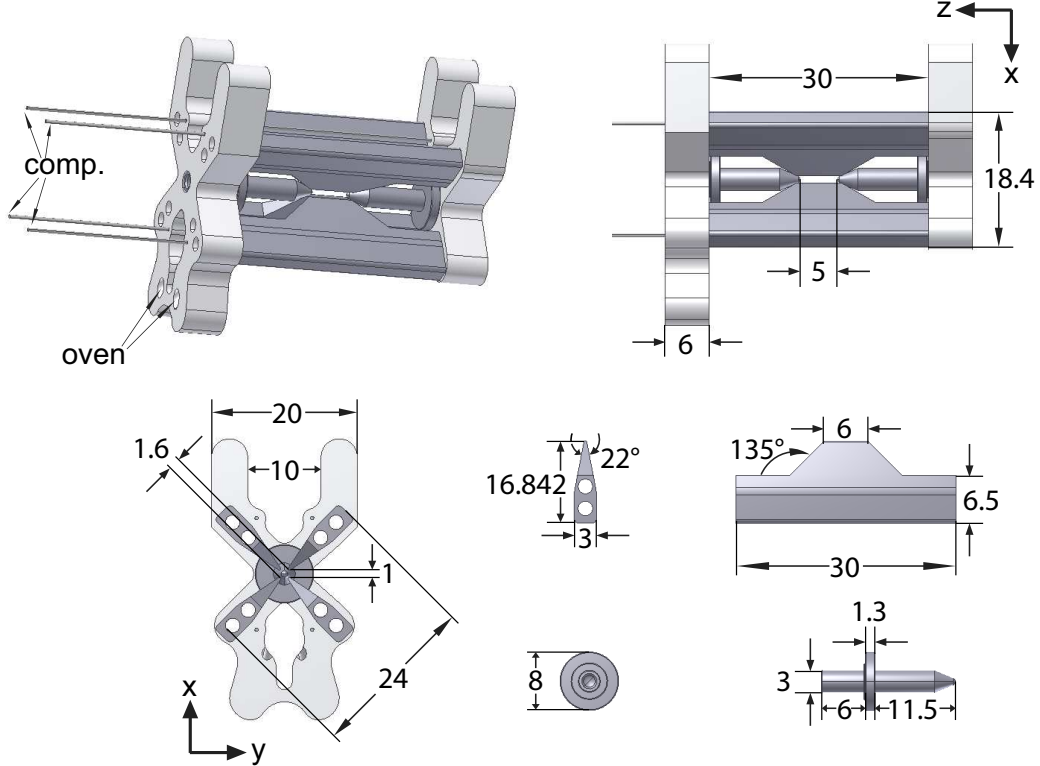


Figure 4.1.: Projections of the trap structure under different angles. One blade and one end tip are shown separately. The dimensions of each part are indicated in mm.

be measured to be $\omega_z = 1.7 \text{ MHz}$ for an end tip voltage $U_{cap} = 2000 \text{ V}$. Equation 2.8 delivers the numerical factor $\alpha \approx 0.075$. For the axial confinement a Lamb-Dicke parameter [86, 87] of $\eta \sim 7\%$ is measured.

Figure 4.1 shows a sketch of the trap and its projections under different angles as well as a blade and an end tip separately. The brighter parts are made out of Macor, all the dark parts are stainless steel. The Macor holder has been modified with respect to the trap used in [75]. In the new version it serves also as a holder for the Ca ovens. Each trap contains two ovens, little steel tubes that contain an atomic Ca granulate (figure 4.4), which are stuck into two holes in one of the two Macor pieces. On the side facing the trap center the Macor holder has little holes that collimate the atomic beam and direct it towards the center of the trap. The second modification was to place the compensation electrodes at the top and the bottom of the trap rather than at the top and the side. These electrodes are indicated with *comp* in figure 4.1. The optical access from the side can thus fully be used for lenses. In the course of the first measurements it turned out that this configuration is not ideal and that it is difficult to completely compensate micro motion (see chapter 6.2). The compensation electrodes are thin stainless steel wires with 0.5 mm diameter that are mounted through holes in the Macor pieces. The

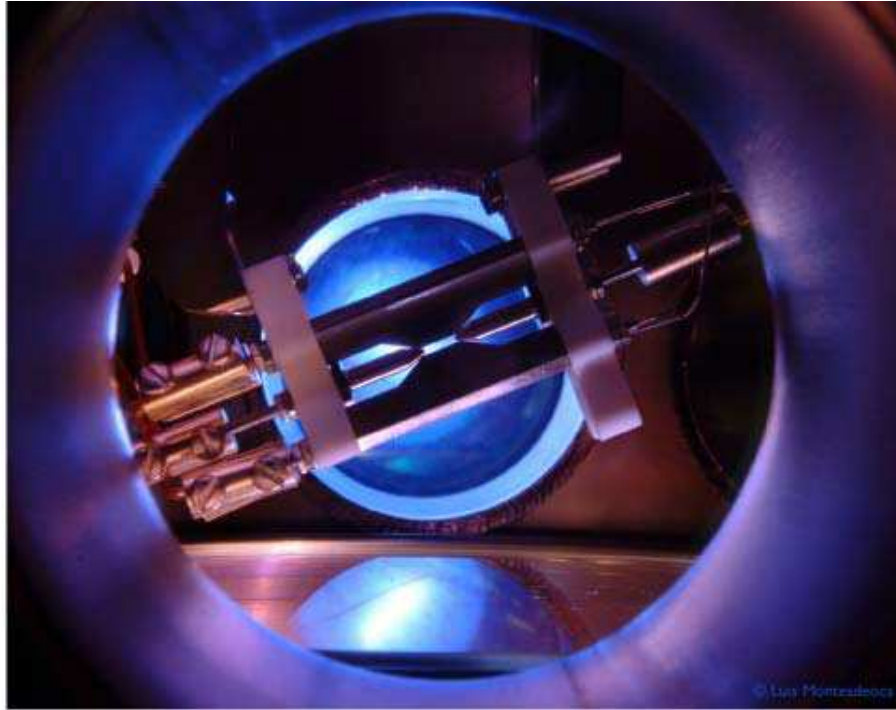


Figure 4.2.: Linear Paul trap inside a vacuum chamber. The HALO lenses are not mounted in this picture. The connections to the electrodes are done through the insulating Macor pieces. The window of a big viewport can be seen at the bottom.

coordinate system x,y,z is introduced as a reference frame for the trap.

Figure 4.2 shows a photograph of the trap through a side port of the vacuum chamber. It is mounted on two posts hanging from the top flange. It is rotated by 22.5° out of the horizontal plane, in order to also have optical access along the horizontal. All connections are done with copper-beryllium inline clamps and Kapton-insulated copper cables are used for the wiring.

4.1.2. HALO Lenses

The lenses are commercial custom-designed High Aperture Lens Objectives¹ (HALOs) with $\text{NA} = 0.4$ numerical aperture and 25 mm focal length, thus collecting light from $\frac{1}{4}\text{NA}^2 = 4\%$ solid angle. The back focal length for light at 400 nm wavelength is 15.1 mm. This leaves several millimeters of space between the radio frequency electrodes of the ion trap and the front surfaces of the lenses. The objectives are designed to be diffraction limited and consist of 4 anti-reflection coated lenses.

The HALOs are mounted on vacuum-compatible slip-stick piezo translation stages² (fig. 4.3). These xyz-positioners have a travel of 5 mm and 400 nm resolution which

¹by Linos

²Attocube xyz-positioner, ANPxz 100

4. Experimental setup

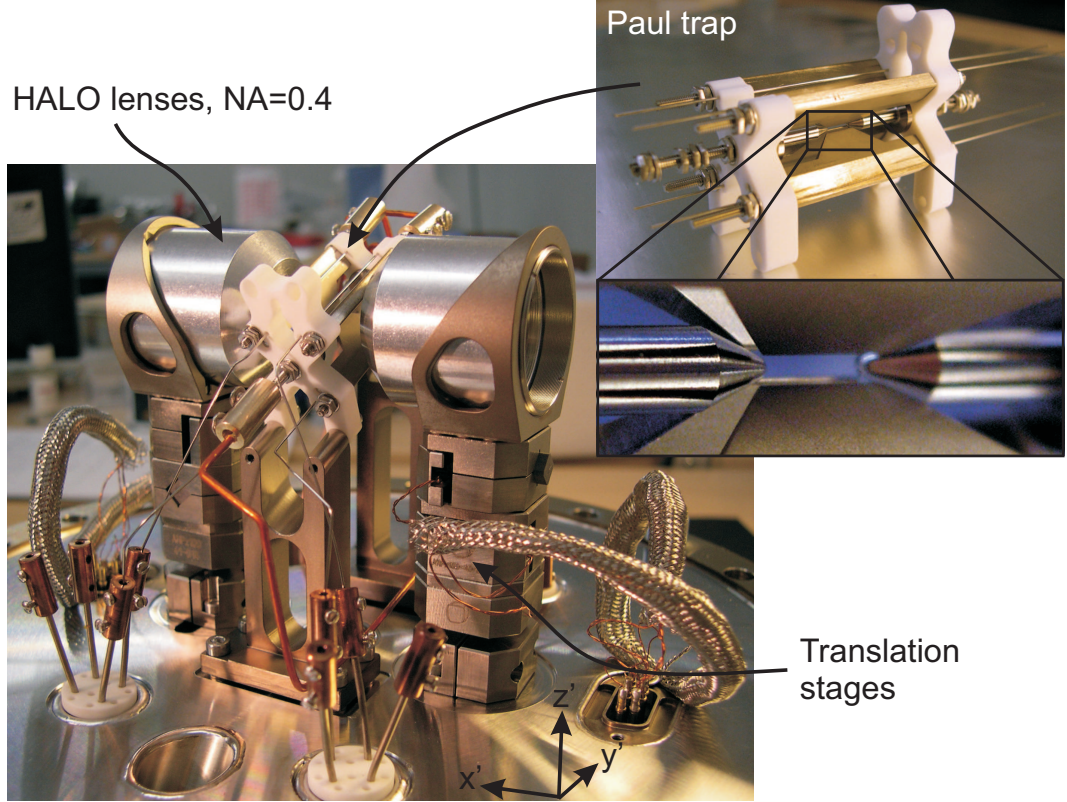


Figure 4.3.: Photograph of the linear Paul trap mounted in between the two HALO objectives. The HALOs are mounted on vacuum compatible slip-stick piezo translation stages which are attached to the CF-200 top flange of the chamber. In the picture the assembly is shown upside down before it was mounted. A grounded braided shielding mesh from stainless steel is guiding the cables for the translation stages to the feedthroughs. In the front, the feedthroughs and connections for the trap and compensation electrodes as well as a through hole for optical access under 52° to the flange (see fig. 4.5) can be seen. The CF-200 top flange is attached to the main chamber, placing the trap at the very center of the latter. The smaller picture shows the trap alone and a zoom into the center trapping region.

allow to maximize the collection efficiency of emitted resonance fluorescence and to address single ions individually when loading the trap with a string of ions. Further details, including a characterization of the wavefront accuracy, can be found in [83] and [88].

4.1.3. Vacuum vessel

The main chamber has octagonal symmetry with eight CF-63 UHV windows and CF-200 ports at the top and bottom. For the bottom port a custom made inverted

CF-200 flange has been purchased³. Figure 4.4 shows a cut through a technical drawing of the main chamber together with a photograph of the real chamber without bottom flange. The original idea was to place an objective for monitoring purpose below the chamber. To be able to place this objective as close as possible to the trap, the CF-200 bottom flange has been inverted. In the present setup however this port is used for the photoionization laser and the LED.

Each Paul trap is mounted in between two HALO lenses as depicted on the photograph in figure 4.3. The coordinate system $x'y'z'$ indicated in figure 4.3 will be used as a reference frame of the chamber throughout the following chapters. The tilt of 22.5° of the traps with respect to the $x'y'$ -plane assures optical access also from the y' -direction as well as effective cooling with light along the same direction, due to non-vanishing projections onto all trap axes. The translation stages and the traps are hanging from the top flange into the vacuum chamber. Figure 4.3 shows the top flange upside down.

Ca ovens

In figure 4.4 the two ovens and an electron gun are indicated in purple. The ovens are stainless steel tubes of 6 cm length, 3 mm diameter and 0.2 mm wall thickness. As shown in the photograph and the sketch of figure 4.4 both of them are electrically contacted at the end facing the chamber wall. The tubes are filled with Ca from the electrical contact up to a little tantalum flag that connects both ovens to a common ground. To operate an oven, a current of about 4.5 A is sent through it (if a cloud of ions is to be trapped this current can be up to 6.5 A). The tantalum flags purpose is to conduct the heat away from the tubes. The part of the tube closer to the trap does not heat up and collimates the atomic beam [89]. A hole in the Macor piece directs the atoms to the center of the trap. There the calcium is ionized either by an electron beam or by photoionization.

Photoionization

While in early ion traps, ionization was obtained with the help of an electron beam colliding with the neutral atoms in the trapping volume, nowadays the most common way to ionize neutral Ca consists of a two-step photoionization process. From the ground state $4s4s^1S$ the population is transferred to the excited state $4s4p^1P_1$ by the use of a 423 nm laser. From the 1P_1 state, light at 389nm transfers the population to high-lying Rydberg states from where the atoms are field-ionized in the Paul trap potential. At the time of construction of the experiment no laser diodes at these wavelengths were available. For this reason, a novel two-step photoionization method has been developed, which involves a single-pass frequency-doubling source of 423 nm light and a high-power LED at 389 nm. Although photoionization is cleaner and much more efficient, an additional electron gun has been built in for

³diffusion bonded by UKAEA

4. Experimental setup

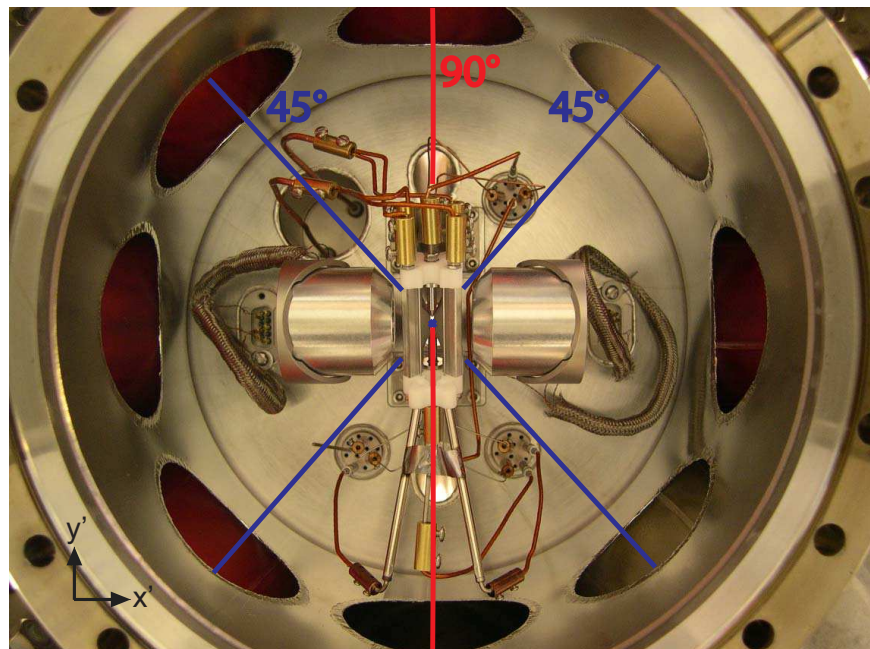
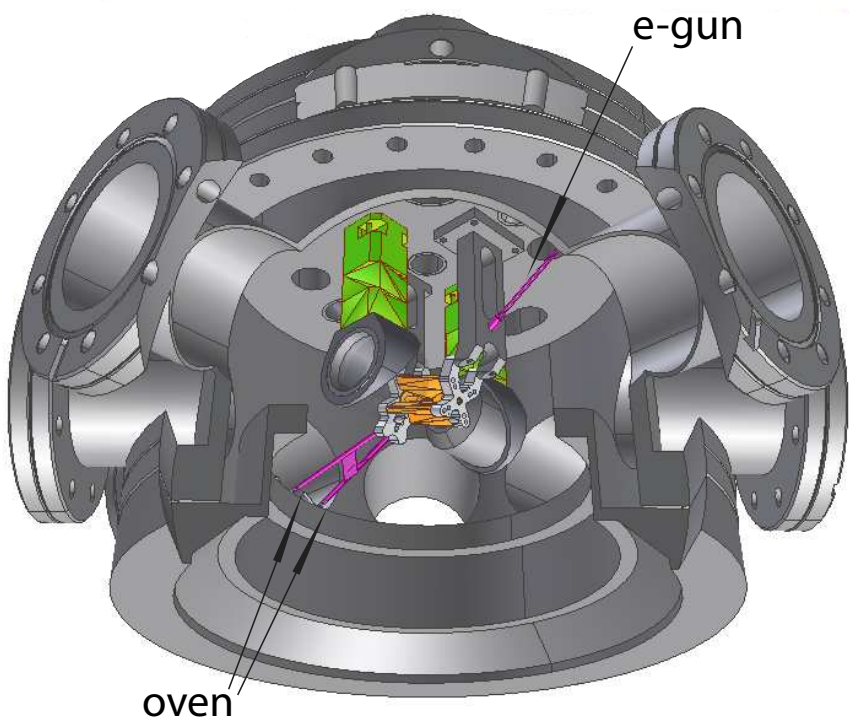


Figure 4.4.: Top: Cut through the octagonal main chamber. The Paul trap and the HALO lenses are at the center of the chamber. Ovens and electron gun are purple. One lens has been made transparent to clear the view onto the trap. Bottom: Photograph of the inside of a chamber with bottom CF-200 flange taken off.

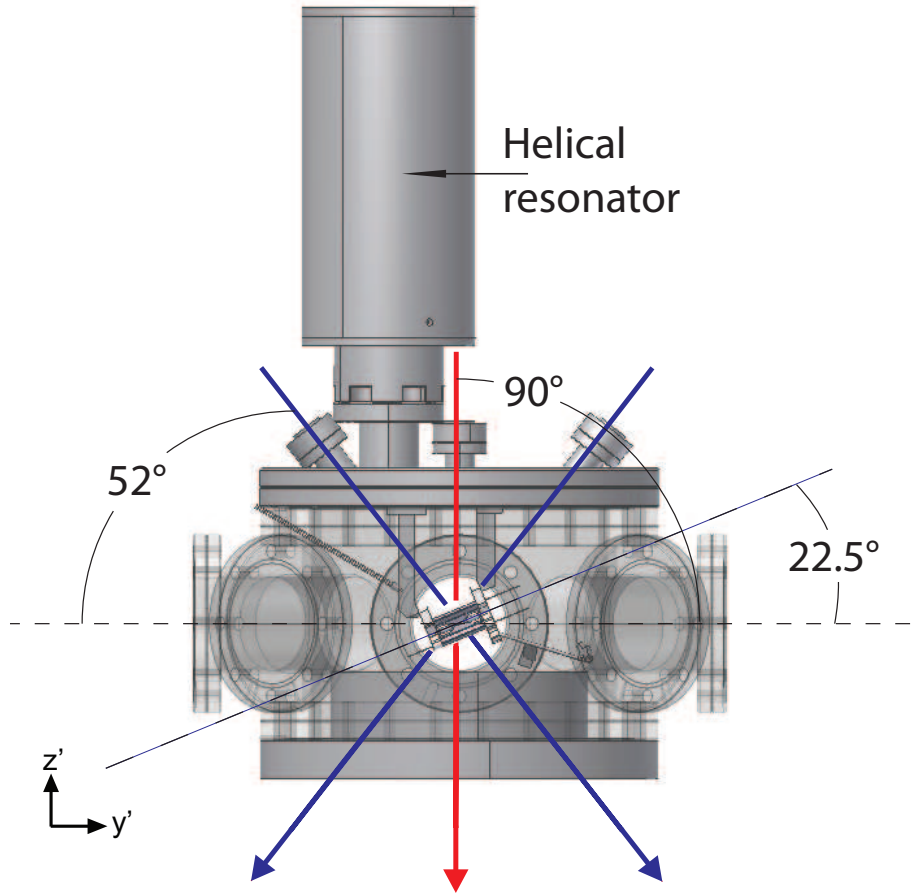


Figure 4.5.: Projection of the chamber onto the vertical plane. The top flange offers three additional viewports, one under 90° with respect to the y' -axis and two under 52° .

security reasons. A detailed description and analysis of the photoionization scheme can be found in [83].

Laser beam geometry

In the photograph in figure 4.4 three laser beams are indicated, two under 45° to the x' -axis and one under 90° . Figure 4.5 shows a projection of the chamber onto the vertical plane. The top CF-200 flange has three additional CF-16 windows, one at the center of the flange and two under 52° with respect to the y' -axis. These ports offer additional optical access from the top or the bottom of the chamber under different (in figure 4.5 indicated) angles with respect to the trap.

The chamber has been designed with the idea to bring the HALO lenses as close as possible to the trap center, but at the same time to allow for optimal optical

4. Experimental setup

access from all directions. The HALO lenses had to be tapered to fulfill these requirements. The most important considerations that lead to the final arrangement of trap, HALOS and quantization axis are:

- For the transition from the $4^2S_{1/2}$ to the $4^2P_{1/2}$ level, the Clebsch-Gordan coefficients are twice as big for σ polarized light than for π polarized light. The directional dipole emission probability for σ polarized light is maximal along the quantization axis, while for π polarized light it is maximal perpendicular to the quantization axis. Because for many entangling protocols polarization selective detection of photons is necessary [61, 59], higher count rates can be achieved detecting σ polarized light along the quantization axis than π polarized light perpendicular to it. This is why the quantization axis has been chosen along the axis of observation, i.e. the x' -axis (see chapter 4.1.4).
- To achieve full control over the polarization, optical access perpendicular to the quantization axis is necessary (90° beam figure 4.4 Bottom). At the same time it is convenient to have a beam with a projection onto the quantization axis in order to excite σ and π transitions simultaneously (45° beams figure 4.4 Bottom).
- Beams with projections onto all trap axes (x,y,z) should be available. This assures efficient Doppler cooling in all three directions and the possibility to excite vibrational modes.
- For micromotion compensation in a linear trap two independent beams with respective projections onto the x - and y -axis of the trap are necessary. A combination of two beams, one in the $x'y'$ -plane and one in the $y'z'$ -plane, fulfills this requirement.

4.1.4. Magnetic field coils

The magnetic field in the center of each trap is defined by 5 coils. Two pairs of small coils are attached to the opposed CF-63 flanges on the x' - and y' -axis of the main chamber (see figure 4.9). One bigger coil is mounted on the upper CF-200 flange. The small coils have 300 windings on an inner diameter of 117 mm. A wire with a diameter of 1.4 mm is used, which results in a resistance of 1.4Ω . At the maximum current $I_{max} = 3\text{ A}$ a power of 12 W is dissipated and the coils heat up to 32°C . For I_{max} two small coils on the x' -axis generate a magnetic field of 6.2 G in the center of the trap. The big coil has 168 windings on an inner diameter of 257.5 mm. The same wire as for the small coil yields a resistance of 1.2Ω . The magnetic field in the trap center for I_{max} is 12.5 G.

The coils' purpose is to compensate the earth magnetic field and defining a quantization axis. The earth magnetic field in Barcelona is of the order of 0.45 G and is therefore easily compensated in all directions. Higher magnetic fields are used to control the Zeeman splitting of the electronic levels. In principle the configuration

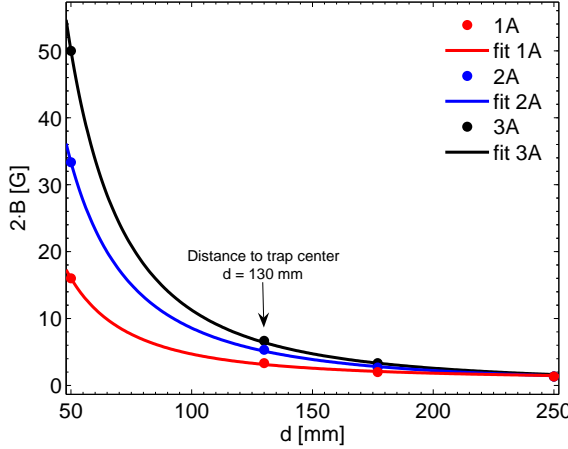


Figure 4.6.: Twice the magnetic field depending on the distance d on the axis of one small coil for different currents. The data points are fitted with $1/x^2$.

allows to set the quantization axis to any desired direction. In the experiments presented here, it was set along the observation channel, i.e. the x' -axis. The 6.2 G that the two small coils generate for I_{max} at the site of the ions correspond to a Zeeman splitting of the $S_{1/2}$ ground state of 17.4 MHz. The splitting can thus be tuned over almost the full natural linewidth of the P-states.

The magnetic field generated by a small coil was measured to check the consistency with a simulation according to the Biot-Savart law. The field was measured with a Hall probe before mounting the coil on the chamber. Figure 4.6 shows the magnetic field depending on the distance from the coil center on the x' -axis as a function of the current. The data was multiplied by two to simulate the magnetic field created at the trap center. The data points are fitted with $1/x^2$ and show good agreement with the theory. Also the big coil delivers the expected field.

The current through the coils is controlled by self-build coil-drivers that are described in detail in [84]. The accuracy of the generated magnetic field depends on the precision of the driver. It contains a control loop where the current is measured by a resistor and regulated accordingly. The precision is limited by the accuracy of the resistor. The main source of errors are temperature fluctuations. Under usual lab conditions the temperature is constant up to 1 °C. Calculated from the specifications of the resistor, this corresponds to a fractional current uncertainty of 65 ppm/°C or an uncertainty of the magnetic field of 400 μ G for 2.74 A. The resulting shift of the $S_{1/2}$ ground state of $^{40}\text{Ca}^+$ in frequency is 1.2 kHz. Compared to the natural linewidth of the P-states and the laser linewidth from chapter 4.2.13, this is negligible.

4. Experimental setup

4.1.5. Helical resonator

The high-voltage radio frequency of the Paul trap is resonantly enhanced and impedance matched by a helical resonator. The trap electrodes are connected to the open end of the helical resonator [90]. Figure 4.7 shows a sketch and a photo of the resonator which is driven at its resonance frequency by a Direct Digital Synthesizer (DDS)⁴. Before the RF-signal is coupled into the resonator it passes through a variable gain sine-wave amplifier, a high power amplifier⁵ and a cross needle power meter⁶. The sine-wave amplifier has an additional TTL output which is used in the micromotion compensation. The variable gain is used to change the RF power coupled into the resonator and therefore the radial trap frequency. The cross needle meter measures the power coming from the high power amplifier as well as the back reflected power from the resonator. By minimizing the back-reflection the resonance frequency of the combined resonator-trap-system is determined (see further down in this section). Due to a capacitive coupling between the trap and the HALO lenses the resonance frequency varies slightly depending on the position of the lenses along the x'-axis. On one side this effect is inconvenient since the frequency of the drive has to be changed every time the HALOs are moved. On the other side this can be used to reference the position of the HALO to a certain frequency. The Attocube driver does not provide an absolute position read out. Once the HALO has been aligned to a prominent position, such as the focal position for 866 nm or 397 nm, the resonance frequency can be used to come back to the same position again. Changing between red and blue focal position becomes a straightforward procedure once the HALOs are calibrated in this way.

The biggest challenge designing a helical resonator is to hit the desired resonance frequency [75]. All the requirements for the design parameters of the bare resonator are well described in ref. [90]. However the expressions in [90] do not take into account the influence of the trap itself onto the resonance frequency. To derive the resonance frequency ν_h for the combined system, the resonator with the trap as a load, one has to solve the Telegrapher's equation [91]. The load impedance

$$z_l(\nu_h) = \frac{1}{i \cdot 2\pi \cdot \nu_h C_l} \quad (4.1)$$

(z_l can be assumed to be pure capacitive as the inductance of the trap is negligible with respect to the inductance of the coil) defines the boundary conditions for this set of linear differential equations. C_l is the load capacitance. Solving the equations leads to the expression

$$\arctan \left[\frac{i \cdot z_l(\nu_h)}{z_0} \right] = \frac{2\pi \cdot \nu_h}{v \cdot b_{eff}}. \quad (4.2)$$

Where $z_0 = \sqrt{\mathcal{L}/\mathcal{C}}$ is the characteristic impedance with \mathcal{L} and \mathcal{C} being the inductance and conductance per unit length respectively. The phase velocity v is defined by

⁴Analog Devices AD9858

⁵Mini-Circuits LZY-1, 50 W, 50 Ω

⁶DAIWA CN-801 H-type

4.1. Trap apparatus

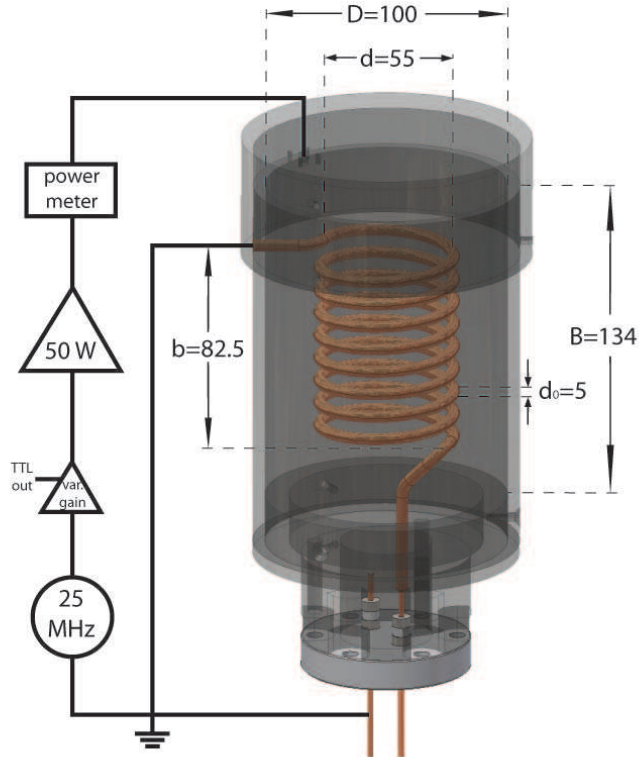


Figure 4.7.: Top: Sketch of the helical resonator consisting of a copper helix that is shielded by a tube, a UHV feedthrough and a cap with inductive in-coupling. Before the RF-signal is coupled into the resonator it passes through a variable gain sine-wave amplifier, a high power amplifier and a cross needle power meter. The most important design parameter are indicated. The values are given in mm. Bottom: Photograph of the polished open helical resonator.

4. Experimental setup

$v = \frac{1}{\sqrt{\mathcal{L} \cdot \mathcal{C}}}$ and b_{eff} is the effective length of the helix of the resonator [90]. If C_l is known, it is possible to numerically solve equation 4.2 and predict the resonance frequency ν_h for a particular load capacitance.

\mathcal{L} and \mathcal{C} can be calculated according to [90] from the design parameters of the helical resonator. For our helical resonator these parameters are shown in figure 4.7. The diameter of the cylinder is $D = 100$ mm, the diameter of the coil is $d = 0.55 \cdot D = 55$ mm, the length of the helix is $b = 1.5 \cdot d = 82.5$ mm, the total length of the resonator is $B = D/2 + b \approx 134$ mm, the diameter of the wire is $d_0 = 5$ mm and the number of windings of the helix is $n = 8.5$.

The load capacitance was measured with two different methods. One possibility is to measure C_l directly with a very sensitive multimeter. The second method measures C_l via a resonant circuit determining its resonance frequency. Both methods were applied and agree to $C_l = 18$ pF.

With the measured capacitance and the values listed above, the theoretical loaded resonance frequency results to $\nu_{theo,l} = 25$ MHz, and the unloaded frequency to $\nu_{theo,u} = 57$ MHz. A measurement with a tracking generator⁷ for the unloaded frequency delivers a slightly lower frequency $\nu_{exp,u} = 54.1$ MHz. The loaded resonance frequency was measured via the reflection on the power meter and yields a frequency of $\nu_{exp,l} = 26.4$ MHz. After aligning the HALOs, the final resonance frequencies are: 26.04 MHz for the bright trap and focal position for 397 nm, 26.117 MHz for the bright trap and focal position for 850 nm, 25.792 MHz for the dark trap and focal position for 397 nm.

All parts shown in figure 4.7 are made of copper. Instead of contacting the helix directly, an inductive coupling into the resonator has been implemented. The photograph of figure 4.7 shows the cap of the resonator. A coil with one winding connects the input with the wall of the cap (ground). The coupling can be optimized by lowering or lifting and rotating of the cap, which is fixed to the main tube with three screws.

The quality factor of the unloaded resonator ($Q_{unload} = 700$) measured with the tracking generator differs by a factor of 2 from the theoretical value ($Q_{theo} = 1480$). The reason for this could be higher resistance of the circuit, e.g. due to a non perfect weld between the helix and the tube or other imperfections. According to [90] the quality factor scales with the resonance frequency. The measured quality factor $Q_{load} = 380$ for the loaded resonator confirms this ratio. The quality of a helical resonator depends strongly on the conductivity of the inner surface of the main tube and the helix. In an attempt to improve the conductivity one of the two resonators was polished, but no significant improvement of the quality factor could be observed.

One helical resonator is attached to each chamber via a CF-35 flange welded to the top CF-200 flange (figure 4.5). The feedthroughs are specified for a maximum voltage of $U = 5$ kV.

⁷Rohde & Schwarz FS315 Spectrum Analyzer

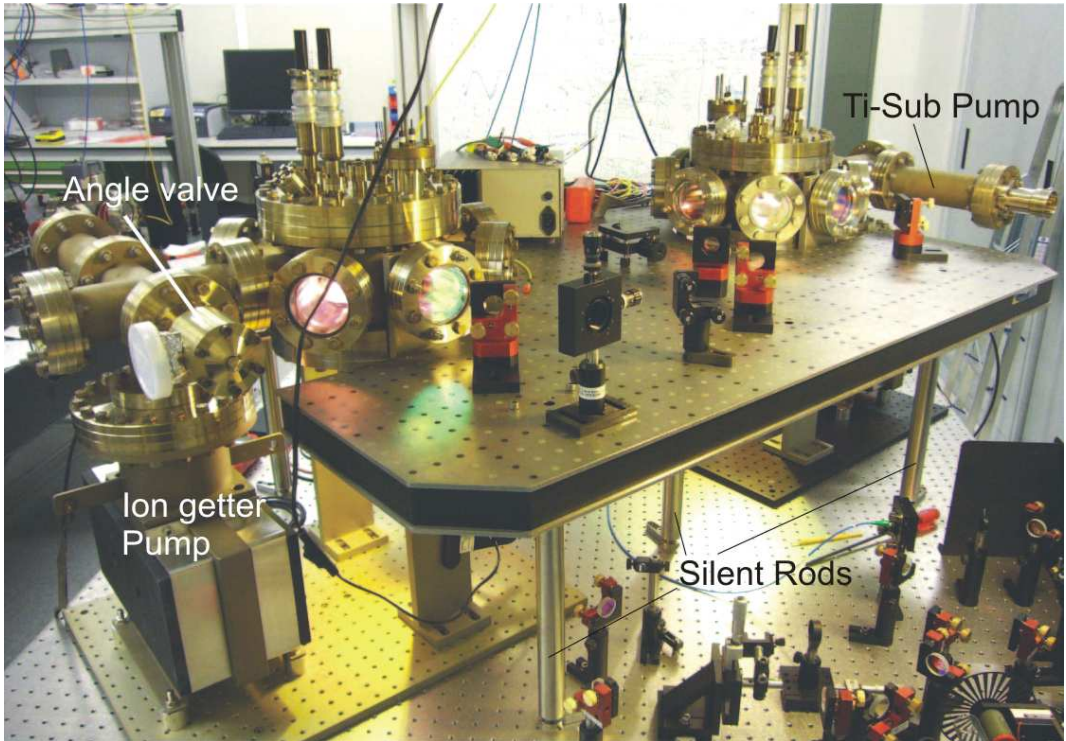


Figure 4.8.: The two vacuum chambers with ion getter and Ti-sublimation pumps on the optical table. A custom made honeycomb bread board is mounted on vibration-damping posts (silent rods) and connects both chambers forming a rigid construction. The photograph shows an early stage of the experiment without helical resonators and electric connections.

4.1.6. Combined Setup

Both vacuum chambers are mounted to the optical table by two strong aluminium posts. To stabilize the construction a third base is formed by a 50 l ion getter pump⁸. The pump is connected to the main chamber by a five-way cross. A titanium sublimation pump⁹ and a UHV angle valve to connect a turbo pump during bake out are also attached to the five-way cross (see figure 4.8). The fifth port of the cross is closed with a viewport to keep the optical access along the y'-axis free.

Figure 4.9 shows a sketch of the combined setup of the two traps and all the optics on the breadboard as it was mounted on the optical table at the time of the completion of this thesis. Traps and lasers have been separated on two different tables to avoid RF-noise in the laser stabilization and for space reasons. Fiber connections to the lasers and the detection setup are also shown in figure 4.9.

⁸Thermionics IP-050

⁹Thermionics SB1020

4. Experimental setup

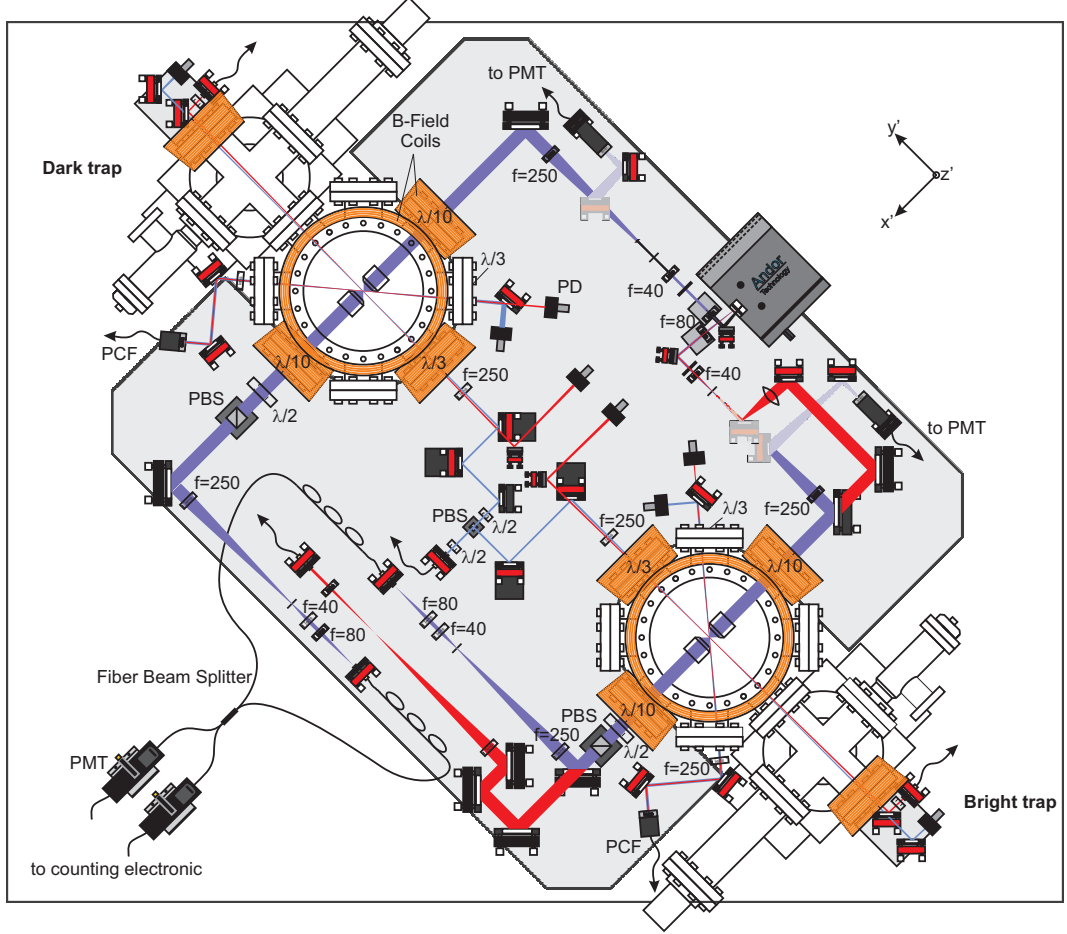


Figure 4.9.: Combined setup on the trap table. The light is brought with fibers from the laser table. Each trap has two alternative excitation channels (under 90° and 45° with respect to the quantization axis). On one side of the breadboard the fluorescence light of the ions collected by the HALO's is imaged onto a CCD camera. On the other side the collected fluorescence is modematched to the two input ports of a fiber beam splitter. At the output ports of the fiber beam splitter the photons are detected by two photomultipliers.

Interferometric stability

For certain entanglement protocols [59], interferometric stability of the setup is required. This means that the distance between two ions in the two different traps has to be stabilized well below half a wavelength of the used light. In order to reach this future goal, the setup has been designed with a special focus on stability from the very beginning. The two chambers are connected with a custom made honeycomb breadboard¹⁰ and form a rigid construction. The breadboard has a

¹⁰1HB series Standa

flatness of $\pm 0.1 \text{ mm/m}^2$ and is supported by six posts consisting of stainless steel and filled with vibration-damping plastic¹¹. The position of the posts has been adjusted to suppress vibrational modes of the board.

Optics

Since the protocols for distant entanglement of atoms like [59, 92, 62, 63, 64], which the setup is designed to study, rely on interference of indistinguishable single photons, special care has to be taken not to distort the wavefront of the photons on their path to the place of interference. Otherwise the fidelity of the final entangled state will be reduced. In all mentioned protocols the interference of fluorescence light happens at a beam splitter which forms an interferometer with the two atoms. In our setup these protocols are particularly sensitive right after the HALO lenses, where the wavefront extends over the full aperture of the HALO. This is why all optical elements in the interferometer path have been chosen for high wavefront accuracy and surface flatness. The viewports on the x'-axis, the observation channel, are custom made for high wavefront accuracy. The flatness of the substrate before diffusion-bonding to the CF-63 flange¹² has been specified to be $\lambda/10$ for 632 nm. Two windows with a flatness of $\lambda/3$ are mounted at the excitation channel (y'-axis ports of the two chambers facing each other) as well as under 45° with respect to the y'-axis facing the CCD camera (see figure 4.9). Also the 10 mm thick substrate of the inverted bottom viewport was specified to $\lambda/3$ before bonding to the flange. All custom-made viewports are made from spectrosil 2000, a synthetic fused silica glass with good optical properties. It exhibits a very high purity, is bubble free, fluorescence free and very well suited for UV light. All other UHV windows are made from ordinary BK7 glass. Each window is anti-reflection coated for 397 nm, 729 nm and 866 nm from both sides. The CF-200 flanges have a coating optimized for an angle of incidence of 38° for the same wavelengths.

Beam distribution and detection channels

The level scheme of $^{40}\text{Ca}^+$ is presented in chapter 5.1. For the transitions used in the experiments presented in this thesis, laser light at 397, 850, 854 and 866 nm is needed. All experiments rely on detecting the 397 nm fluorescence light that is scattered by the ion when it is illuminated with 397 and 866 nm laser light. Both traps have an excitation channel under 45° to the x'-axis for these two wavelengths. The 397 nm and 866 nm light is coming through two separate fibers from the laser table to the trap table. Each beam is split into two parts and the two infrared and blue beams are then overlapped (not shown in figure 4.9) to be coupled into two Photonic Crystal Fibers¹³ (PCF) respectively. The use of PCF has the advantage that both beams are automatically overlapped. For two independent beams with

¹¹Silent Rod 2SR32-30 Standa

¹²fabricated by UKAEA

¹³Crystal Fibre LMA-PM-5

4. Experimental setup

a small waist this is not an easy task as they have to be overlapped with the two photo-ionization lasers and the atomic beam in the trap center. After the PCF, an achromatic lens collimates the two beams and a second one focuses them into the chamber. On the other side of the chamber, the beams are split by a dichroic mirror and detected by two photodiodes (PD) to monitor the power. The PCF channel was used to trap and cool ions for the first time. The angle of 45° to the quantization axis (x' -axis) ensures that π - and σ - transitions are driven and no accidental pumping into dark states happens, which would be the case if for example at 866 nm only π transition were excited.

The use of PCF's has the disadvantage that the polarization after the fiber cannot be controlled separately for blue and infrared light. Also an excitation channel with the capability to excite pure π - (H-polarized light under 90° to the quantization axis) or σ -transitions (V-polarized light under 90° to the quantization axis) is required. This is why for each chamber 397 nm and 866 nm beams under 90° to the x' -axis have been added. A fiber for the blue light ends in the middle between the two chambers. The light is distributed between bright and dark chamber by a $\lambda/2$ -waveplate and a polarizing beam splitter (PBS). For the dark chamber the light is rotated back to vertical polarization. Both beams get focused into their respective traps by $f = 250$ mm lenses. On the other side of the chamber the 397 nm light passes through a dichroic mirror and is directed to a photodiode.

The dichroic mirror reflects the counter-propagating 866 nm light, which is coupled out from a fiber on a little platform behind the five-way cross, into the chamber. The beam is focussed directly by the fiber coupler, passing a polarizer before the mirror, and it is detected with photodiodes behind the chamber in the same way as the blue beam. The same fiber can also be used to send 854 nm light to the ion (fig. 4.12).

The photodiodes of the 90° channels are connected to the analog inputs of the radio frequency drive (HYDRA) and are used to stabilize the power of the beams (see chapter 4.2.10). Blue and infrared light can be distributed between 45° - and 90° -channels through their respective fibers by means of polarizing beam splitters and $\lambda/2$ -waveplates on the laser table (fig. 4.12).

The fluorescence light of the ions collected by the HALOs is imaged onto a CCD camera¹⁴ on one side of the breadboard. A two-inch dichroic mirror reflects the blue light and a two-inch lens ($f = 250$ mm), that forms a first telescope with the HALO, images the ions onto a slit¹⁵. A second telescope images this intermediate image onto the camera. The overall magnification of the imaging optics is 20. An interference filter in front of the camera reduces the stray light. For both chambers an optional mirror with a magnetic mount can be introduced into the imaging beam path (indicated in pale colors in figure 4.9). It couples the light into a multimode fiber that is connected to a photomultiplier¹⁶.

¹⁴ Andor Ixon DV 887-BI

¹⁵ Owis Spalt SP60

¹⁶ Hamamatsu, H7360-02SEL

4.1. Trap apparatus

For the bright trap a second imaging path for 866 nm light has been set up on the side of the camera. The infrared light is transmitted by a dichroic mirror behind the viewport, while the blue light is reflected. With two mirrors, a lens and a third magnetic mirror the light is also imaged onto the camera. Depending on which mirror is placed in the beam path, either the blue or infrared fluorescence light is sent to the camera, or the blue light is detected by the photomultiplier.

On the side of the breadboard opposed to the CCD camera, the σ -polarized fluorescence light of the ions emitted along the quantization axis passes a $\lambda/2$ -plate and a polarizing beam splitter (PBS). The PBS cleans the polarization and the $\lambda/2$ -plate maximizes the transmission before the light is mode-matched into fibers. Either the light is guided directly to the photomultipliers (PMT) or via a fiber beam splitter¹⁷ as indicated in figure 4.9. In the two input arms of the fiber beam splitter, polarization controllers allow full control of the polarization arriving at the beam splitter.

For the bright trap an additional beam path for incoming light has been set up. A telescope expands the beam leaving a fiber coupler in between the mode-matching optics for the fiber beam splitter. Three mirrors are used to send the light through the dichroic mirror of the 397 nm detection path and the HALO onto the ion. This channel is used in chapter 10.1 to send single photons and a weak laser beam at 850 nm onto the ion. The mode-matching to the single mode fiber is optimized for the HALO in the focal position for 850 nm light.

UHV preparation

All parts exposed to the vacuum except the translation stages, the HALO lenses and the viewports have been baked in a self-built oven for several days at 350 °C. After this first bake-out, the trap, translation stages, HALOs and viewports were mounted. A second moderate bake-out at 150 °C (limited by the translation stages) yielded a pressure better than 10^{-10} mbar after one week. No pressure sensor has been built into the system, but the pressure is proportional to the current through the ion-getter-pump. Since the current is very small for low pressure this measurement is very unprecise and limited to 10^{-10} mbar. However the observed low ion loss rates in our experiments confirms that the pressure is indeed below this value.

The oven consists of a custom-made tent¹⁸ specified for up to 400 °C that is spanned over a rectangular metal structure. Two 2000 W resistors heat the inside of the oven while a ventilator provides air circulation. Four PT100 sensors measure the temperature inside the oven. The current through the heaters is regulated according to the mean value of all four sensors, assuring a slow heating and cooling process. If the gradient between the different sensors is getting too big the heating or cooling process is stopped until the temperature is homogeneous again. The whole process is controlled by a Labview programm involving a PID regulator.

Although the translation stages were specified for UHV-use and temperatures of

¹⁷FOC AKOA-Y11-502V02F-002

¹⁸Rex Industrie-Produkte

4. Experimental setup

up to 150 °C, severe problems occurred after the second bake-out of the first chamber (the dark chamber). Both stages got stuck in the z'-direction. Apparently, the coating of the piezo, an important factor of the slip-stick mechanism which defines the friction between the moving parts, had degenerated during the long bake-out. The translation stages, which were specified for a maximum weight of 300 g, could not move the 100 g heavy lenses. Also the next generation of translation stages, which were promised by Attocube to solve the problem did not work satisfactory after mounting them in the chambers. Again one stage got stuck in the dark chamber, which was finished after the bright chamber. The third generation of translation stages survived the bake-out without any problems. Both chambers could be completed and set up on the optical table with a considerable time delay.

4.2. Laser Setup

In this chapter the laser setup of the experiment is described. It consists of a complex locking chain to frequency stabilize each laser with respect to an atomic transition. Adding this absolute reference to the short-term stabilization of each laser to optical resonators provides very good long term stability. The spectroscopic methods as well as the development of the transfer stabilization scheme using cavities and locking electronics are presented. Finally the frequency stability of one of the lasers is characterized by evaluating its Allan variance.

4.2.1. Lasers

All lasers are commercial grating-stabilized diode lasers in the "Littrow" configuration. In this type of laser, the light emitted by the laser diode is collected by a lens and then strikes a reflection grating. The first diffraction order is reflected back and focused into the laser diode thus forcing the laser to run on the mode selected by the grating. This optical feedback reduces the linewidth to about 1 MHz and can moreover be used to frequency-tune the laser by tilting the angle of the grating. Together with a feed forward mechanism, a mode hop free tuning range of 20 GHz can be reached.

To achieve full control over the internal degrees of freedom of $^{40}\text{Ca}^+$, five lasers are necessary (figure 4.10). Additionally we use a reference laser at 852 nm which is resonant with the D2 line of cesium. The specifications of the six lasers systems are listed according to their wavelength:

- 850 nm: extended-cavity diode laser with 120 mW output power
- 852 nm: extended-cavity diode laser with 120 mW output power
- 854 nm: extended-cavity diode laser with 120 mW output power
- 866 nm: extended-cavity diode laser with 60 mW output power

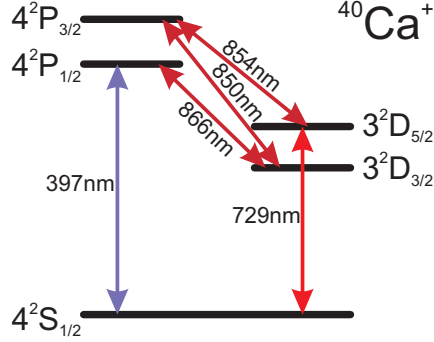


Figure 4.10.: Level scheme of $^{40}\text{Ca}^+$

- 397 nm: extended-cavity diode laser at 794 nm with 120 mW output as master laser power, SHG stage with a BIBO crystal in a bow tie cavity delivers 10 mW output power at 397 nm
- 729 nm: extended-cavity diode laser with 60 mW output power as master laser, tapered amplifier stage delivers 500 mW output power

In order to do high resolution spectroscopy and quantum information processing, the linewidth of the lasers has to be reduced well below the natural linewidth of the respective transition and long term drifts have to be avoided. For this purpose we have developed a novel stabilization scheme that makes use of an atomic reference line in Cs, which is described in the following sections.

4.2.2. Doppler-free saturated absorption spectroscopy

Spectroscopy signals from a thermal atomic gas exhibit a Doppler broadening of the natural linewidth which is caused by the thermal movement of the atoms. According to [93] the resulting linewidth is described by:

$$\delta\nu_D = \frac{2}{\lambda} \cdot \sqrt{2 \ln 2 \frac{k_B T}{M}}, \quad (4.3)$$

with M being the atomic mass, k_B the Boltzmann constant, T the temperature of the gas and c the speed of light. The Doppler broadened linewidth of the $5^2\text{S}_{1/2}$ to $5^2\text{P}_{3/2}$ transition in ^{85}Rb , for example, will be $\delta\nu_D \approx 500$ MHz for a wavelength of 780 nm at room temperature. This is by far too broad to resolve any hyperfine splitting. Doppler-free saturated absorption spectroscopy is a technique which circumvents this broadening.

Two collinear counter-propagating laser beams are sent into the absorption cell. One is a saturating pump beam and the other one a weak probe beam that gets detected by a photo diode, producing the spectroscopy signal. If the laser frequency is not resonant with the atomic transition but within the Doppler profile, then the media can absorb photons from both, the pump and the probe beam. However,

4. Experimental setup

atoms from two different velocity classes, with non zero velocity components, are responsible for the absorption in the pump and probe beam. If the laser frequency is resonant with the atomic transition, then the back and forth running beams are both resonant with atoms at rest (velocity component $v=0$). Photons out of both beams are absorbed by the same atoms. Like this, the more intensive pump beam saturates the atoms, and the cell gets transparent for the probe beam. Using again ^{85}Rb as an example the line shape of a Doppler free spectroscopy signal can be explained. If the frequency is tuned over the Doppler broadened transition line, the absorption of the probe beam breaks down each time the laser hits the resonance of a hyperfine level. The corresponding spectroscopy signal shows narrow dips in the Doppler profile for each resonance (figure 4.17 and 4.24). At all mid frequencies of two hyperfine levels a "crossover-resonance" is observed. These dips are caused by atoms with a non zero velocity component along the beam direction, that are resonant with two different transitions for the pump and probe beam. Moving towards one beam and away from the other, the Doppler shift they experience has opposite sign but equal magnitude. Since these lines are especially pronounced in the spectroscopy signal they are used for the laser stabilization.

4.2.3. Pound-Drever-Hall technique

The technique was first introduced to stabilize microwave oscillators by Pound in 1946 [94] and transferred onto optical frequencies in the early 1980's by Drever, Hall and coworkers [95]. It uses a radio-frequency phase modulation to convert the frequency deviation of a laser from a reference into an electronic error signal. The reference can be any frequency discriminator with frequency-dependent phase shift, like a Fabry-Perot cavity or a gas of atoms. The error signal has a sharp zero crossing at the peak of the spectral feature, i.e. at the cavity resonance or at the atomic line center. This change of sign vs. the detuning produces an ideal control signal. In the case of a grating-stabilized diode laser, feeding the error signal back onto the current of the laser and the piezo actuator that controls the angle of the grating, can reduce the linewidth of laser emission. A detailed description of the technique is found in [96].

If the phase of a laser passing through a frequency discriminator is modulated with the frequency Ω_{mod} and the amplitude $M = \frac{\delta\Omega_{mod}}{\Omega_{mod}}$, the electric field reads

$$\tilde{E}(t) = \frac{1}{2} \tilde{E}_0 \left(e^{i(\omega_L t - M \sin(\Omega_{mod} t))} + c.c. \right). \quad (4.4)$$

Where ω_L is the carrier frequency of the laser before the modulation. This leads to sidebands in the frequency spectrum of the signal that is detected after the discriminator. These sidebands are arranged symmetrically around the carrier at frequencies $\omega_L \pm \Omega_{mod}$, $\omega_L \pm 2\Omega_{mod}$, ... In our experiment the modulation is obtained via the current of the laser diode. This leads also to a small amplitude modulation that shall be neglected here but is treated in further detail in appendix D. For small M one

4.2. Laser Setup

can consider only the first two sidebands. The electric field is then approximately:

$$\tilde{E}(t) = \frac{1}{2} \tilde{E}_0 \left[\frac{M}{2} e^{i(\omega_L + \Omega_{mod})t} + e^{i\omega_L t} - \frac{M}{2} e^{i(\omega_L - \Omega_{mod})t} + c.c. \right] \quad (4.5)$$

Passing through the discriminator the light experiences a frequency-dependent absorption and dispersion. This is taken into account by a factor $T_j = e^{-\delta_j - i\phi_j}$, where $j = 0$ represents the carrier, $j = \pm 1$ the sidebands, $\delta_j = \alpha_j L/2$ the absorption and $\phi_j = n_j L(\omega_L + j\omega_{mod})$ the phase shift. α_j is the absorption coefficient, n_j the refractive index, and L the length of the discriminator. The electric field thus takes the form:

$$\tilde{E}(t) = \frac{1}{2} \tilde{E}_0 \left[\frac{M}{2} T_1 e^{i(\omega_L + \Omega_{mod})t} + T_0 e^{i\omega_L t} - \frac{M}{2} T_{-1} e^{i(\omega_L - \Omega_{mod})t} + c.c. \right] \quad (4.6)$$

A photodiode detects the intensity that results from (4.6) according to $I(t) = \epsilon_0 c E^2(t)$. However, frequencies of the order of ω_L can not be detected with a common detector. But due to interference of the sidebands with the carrier, a beat signal with the modulation frequency Ω_{mod} can be observed:

$$I(t) = \epsilon_0 c \tilde{E}_0^2 e^{-\delta_0} [1 + M(\delta_{-1} - \delta_1) \cos(\Omega_{mod} t) + M(\phi_1 + \phi_{-1} - 2\phi_0) \sin(\Omega_{mod} t)] \quad (4.7)$$

The detector only sees a modulated signal if there is a difference in the absorption of the sidebands or if the phase shift of the carrier deviates from the mean of the sidebands. Via a phase selective detection one can choose between an absorptive ($M(\delta_{-1} - \delta_1)$) or a dispersive ($M(\phi_1 + \phi_{-1} - 2\phi_0)$) signal. This can be achieved by demodulating the beat signal that the photo diode delivers with a mixer that uses the source of the phase modulation as the local oscillator. At resonance the phase shift of the carrier is zero and the shift of the two sidebands has opposite sign and equal amplitude. Thus at resonance the dispersive signal vanishes. Since the modulation frequency Ω_{mod} is typically chosen much bigger than the width of the spectral feature and the phase shifts of the sidebands depend very strongly on the frequency distance from the resonance, the signal is very sensitive to detuning. The demodulation delivers a voltage that is proportional to the frequency deviation of the laser from the reference and can be used for frequency stabilization. In figures 4.20, 4.17, 4.18, 4.19 and figure 4.25 such error signals are plotted for a Fabry-Perot cavity, a Cs and a Rb absorption cell.

4.2.4. Stabilization scheme

The stabilization scheme consists of a chain of consecutive Pound-Drever-Hall locks. Figure 4.11 shows a sketch of the locking chain. A reference laser at 852 nm is locked to the D2 line of Cs using the Pound-Drever-Hall technique in combination with Doppler-free absorption spectroscopy on a Cs cell. This laser serves as the

4. Experimental setup

reference for all other lasers. Its stability is transferred to the other lasers by the use of temperature stabilized low finesse cavities (chapter 4.2.5). A Pound-Drever-Hall lock stabilizes the length of the cavities with respect to the reference laser. Each laser is then stabilized with another Pound-Drever-Hall lock to its respective transfer cavity. Each transfer cavity is brought to a resonance condition for both the reference laser and an additional laser at the same time by a coarse temperature tuning plus fine tuning using an AOM (chapter 4.2.7). The advantage of this scheme is that not only the linewidth on a short time scale is reduced by the lock to the cavity, but also long term drifts are eliminated due to the referencing to an atomic line.

In more detail, a beam splitter is used to send $50\mu\text{W}$ of the 852 nm reference beam to the Cs cell and the rest of the power to the different transfer cavities. The error signal derived from the saturated absorption spectroscopy on the Cs cell is fed back onto the piezo controlling the length of the first cavity via a self-built electronic device for stabilization called "cavity locker", see section 4.2.6. The cavity locker has a Pound-Drever-Hall module that uses the 20 MHz oscillation signal from a current modulation of the reference laser to demodulate the absorption signal. A digitally implemented compensator controls the piezo of the cavity. At the same time a low frequency regulation stabilizes the temperature via a heating wire.

The error signal from the light reflected from this first cavity is used to stabilize the reference laser to this cavity with the help of commercial electronics¹⁹. The electronics consist of a Pound-Drever module which contains the oscillator that modulates the current of the laser through a bias T and a mixer that demodulates the signal coming from the photo diode. The 20 MHz modulation signal is generated by a quartz and is also supplied to all the cavity lockers for stabilization to the reference laser. The error signal generated by the Toptica electronics is then passed on to the PID regulator where the different gains are adjusted. The output of the PID is given onto the piezo that controls the grating in the laser head. Additionally the laser is equipped with a FET Current-Control that exhibits a high modulation bandwidth of 5 MHz. Applying the bare error signal to this FET is equivalent to a fast proportional additional feedback to the laser and improves the frequency stability significantly.

Using the error signal from the saturated absorption spectroscopy for the cavity and the one from the cavity for the laser is in principle equivalent to doing it vice versa. In both cases laser and cavity will be stabilized to the Cs line. The implemented scheme, however, is the optimal choice for the following reasons. Taking into account that the piezo of the cavity has a bandwidth [84] of about 3 kHz and the FET a bandwidth of 5 MHz it seems natural to exploit the potential of the fast FET regulation. The steeper the slope of an error signal, the faster is the response to a possible frequency deviation. Since the natural linewidth of Cs is 32.8 MHz [97] and the measured linewidth of our cavities is around 1.9 MHz [98] the slope of the cavity error signal is much steeper and was therefore chosen to stabilize the laser.

¹⁹Toptica DC110

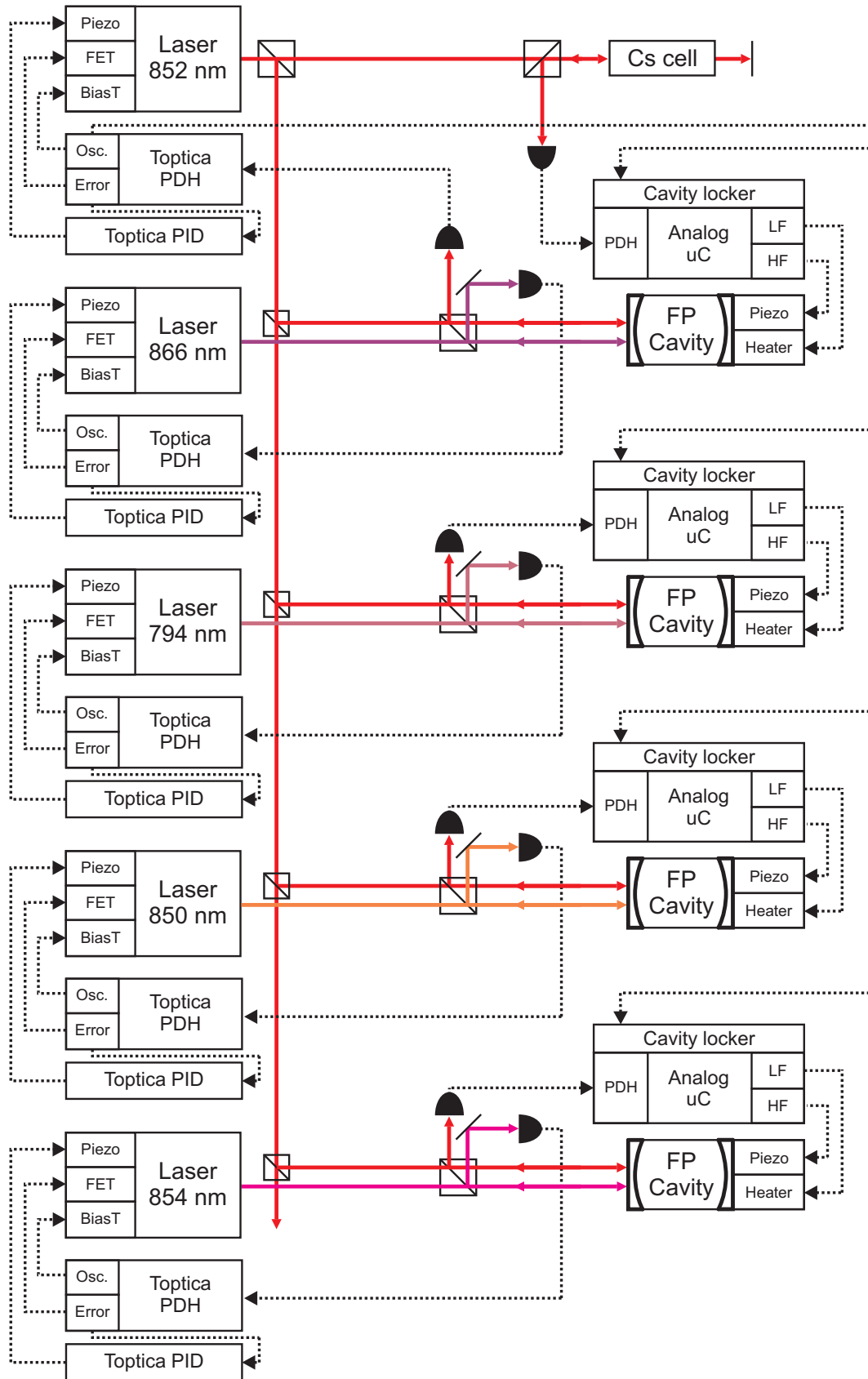


Figure 4.11.: Laser stabilization scheme

4. Experimental setup

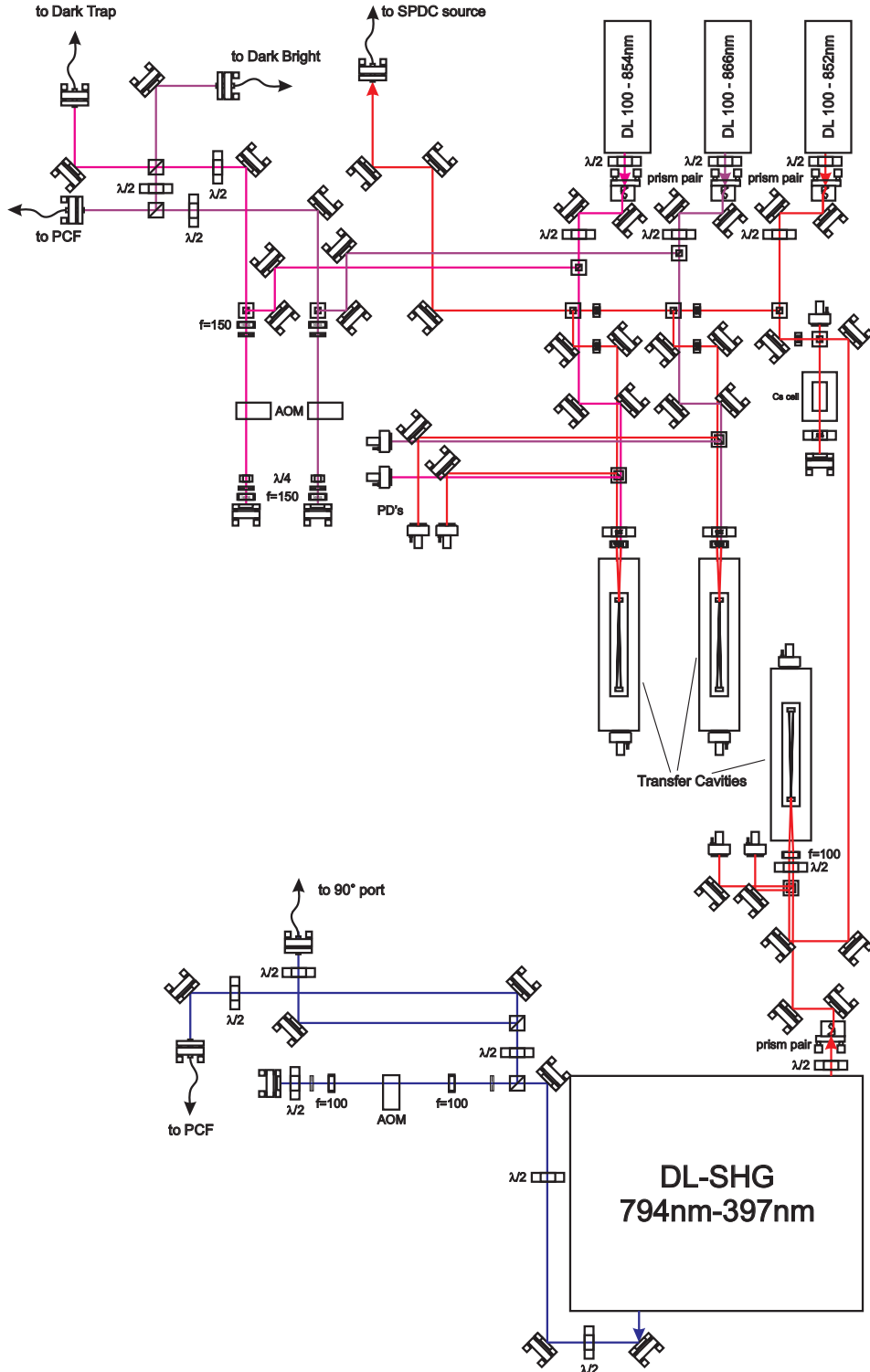


Figure 4.12.: Setup of the stabilization chain. All lasers locked via transfer-cavities to the reference laser, which itself is locked to a Cs cell. The 850 nm laser is the fundamental of a SPDC source in the neighboring lab. The light is brought to the trap table (see figure 4.9) via optical fibers.

The reference laser is coupled to all the respective transfer cavities and the individual reflection signals are used to stabilize the cavities in a similar fashion as before. Finally all lasers are stabilized to their respective cavities using their reflection signals and Toptica electronics in the same way as for the 852 nm laser. All detectors are fast low noise photo diodes with a bandwidth of 125 MHz similar to the model 1801 of New Focus. Figure 4.12 shows the setup on the optical table.

4.2.5. Cavities

The confocal Fabry-Perot cavities are built from two Layertec mirrors ($R = 99,5\%$) at a distance of 15 cm, resulting in a free spectral range of 500 MHz. The mirrors have a broad band coating with a transmission below 1 % for all lasers and an anti-reflection coating at the back side (appendix A). Finesse and linewidth are measured to be 270 and 1.9 MHz, respectively [98]. Only the cavity for the stabilization of 794 nm laser is build from mirrors from a different manufacturer²⁰. Although the specifications are similar, $R = 99,5\%$ and an anti-reflection coating (794 + 852 nm) at the backside, this cavity exhibits a lower finesse ($F \approx 100$).

In all cavities the two mirrors are mounted at the two ends of an aluminium tube as depicted in Figure 4.13. Having a high temperature expansion coefficient ($\alpha = 23 \mu\text{m} \cdot \text{K}^{-1}$), aluminium assures the temperature tunability of the mirror distance. A heating wire with a resistance of 15Ω is wound in a spiral back and forth around the tube. The heating wire and a PT100 temperature sensor are fixed with isolation tape to the aluminum tube. The whole tube itself is wrapped in isolating material and sits inside a bigger aluminium rod that can be mounted on the optical table with two posts. To connect the heating wire, the temperature sensor and the piezo, three BCN connectors are fixed to one side of this outer rod. One mirror is glued to an end cap of the tube that can be screwed in and out for coarse length adjustment. The other mirror is glued to an aluminium ring that is mounted in a special teflon mount. The aluminium ring with the mirror sits in between the two white pieces in Figure 4.13. The first part is a little tube that fits into the aluminium tube with a wedge on the inner side. The aluminum ring with the mirror is pressed by three piezo stacks²¹ against a rubber ring²² that sits in between the aluminum ring and the wedge. The piezo stacks have a cubic rectangular form and are guided by three holes in the second teflon part that sits inside the first one. An end cap that is screwed onto the aluminium tube puts pressure on the piezos and the flexible rubber ring. The piezos find sufficient resistance to compress the rubber ring thus changing the length of the cavity. A maximum voltage of $\pm 10\text{V}$ is applied to the piezos corresponding to a length change of about $2.5 \mu\text{m}$ and resulting in a shift of the resonance frequency of 1.5 GHz. The cavity can thus be scanned over maximal three free spectral ranges using the piezos. Scanning over a wider frequency range requires changing the temperature.

²⁰Standa

²¹Piezomechanik PSt 150/2x3/7

²²inner diameter = 16 mm, thickness = 1.5 mm

4. Experimental setup



Figure 4.13.: Cavity assembly consisting of a commercially available lens tube system and a custom made teflon holder. The picture shows from left to right: end cap with hole for optical access and electric connections, three piezo stacks, teflon part guiding the piezos, aluminium ring, rubber ring, first mirror, teflon part holding the aluminium ring, aluminium tube with heating wire and temperature sensor, end cap for coarse adjustment, second mirror, mirror holder, ring to fix the mirror holder to end cap.

4.2.6. Cavity Locker

The stabilization of the cavities is realized with a self built electronic device called "cavity locker". The cavity locker consists of a Pound-Drever-Hall (PDH) input stage, a microcontroller²³, a scanning unit and outputs for low and high frequency feedback, respectively (figure 4.11). The PDH stage is similar to the Toptica PDH module. It consists of an input amplifier, a mixer, a phase shifter and a bandpass filter and demodulates the photo diode signal [84]. The PDH error signal (similar to figure 4.20) which it produces is the input for the regulator which is implemented with software on the microcontroller. Since the cavity locker is used to lock the cavities to the reference laser, the PDH stage uses the rf modulation signal of the reference laser current as local oscillator (figure 4.11). In control mode the low frequency output is driving the heating wire (chapter 4.2.5) and the high frequency output the cavity piezo. If the control loop is open the piezos can be scanned by the scanning unit and the temperature is stabilized to the value defined by the temperature set point potentiometer. The reading at the PT100 temperature sensor (chapter 4.2.5) is compared to the potentiometer setting and a PI compensator regulates the current through the heating wire accordingly (see appendix B). Figure

²³Analog Devices EVAL-ADUC7026QSZ



Figure 4.14.: Photograph of the cavity locker. The front panel is divided into a Pound-Drever Hall input unit, a unit controlling the piezo and a temperature unit.

4.14 shows a photograph of the cavity locker.

The hold switch (HOLD SETP in fig. 4.14) offers the option to save the last temperature set point in control mode when the control loop is interrupted. If the hold switch is set to on, the cavity locker will hold the current temperature also when it is not locked. This is important because during longer locking periods the temperature set point will slightly vary from the initial value. Taking the cavity out of lock, with the hold switch in the off position, causes the temperature stabilization to regulate to the set point defined by the potentiometer. Relocking will then lead to a different laser frequency (chapter 4.2.7).

A detailed description of the electronic circuit, components, housing and the software implementation of the regulator can be found in [84]. Figure 4.15 shows a block diagram of the control loop used to stabilize the cavity with a description of its working principle in the caption.

Because the piezo set point value is zero the heater compensator will always try to regulate the length in such a way that the piezos are in their mid position. This assures that the piezo is kept in its range and does not have to regulate over its full amplitude. In other words the temperature stabilization follows the piezos. Both compensators are designed (programming language C) analysing the response of the system. The heater regulates low frequency length drifts and is limited by the heating power and the isolation of the cavity. The speed of the piezo compensator loop is limited by the eigen-frequency of the piezo actuators. This frequency has been measured to be 3 kHz.

The advantage of using an evaluation board with a microcontroller for the implementation of the controller lies in the flexibility of the digital technology. The compensators can be changed easily and fast to account for different applications without the need of prototyping electronic boards. The best example is the integration of a mode hop button into the cavity locker after its completion. This function

4. Experimental setup

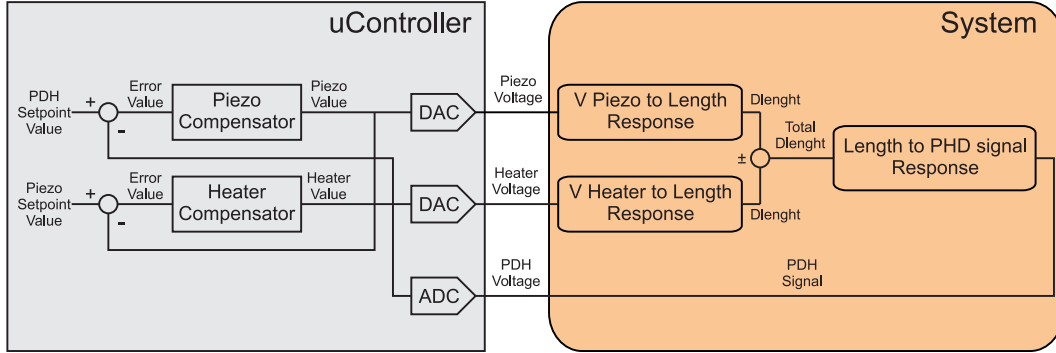


Figure 4.15.: Cavity locker control loop. The system consists of the cavity with its piezos and heater that control the length and the resulting PDH signal generated by the PDH module. The micro controller processes the error signal and controls the piezos and the heater. The PDH signal is digitized by an analog to digital converter (ADC) and compared to the PDH set point value that was programmed to be 1.25 V. From the comparison the piezo compensator calculates the piezo value that is converted into the piezo voltage by the digital to analog converter (DAC). The piezo converts this voltage into a length response. The piezo value is also compared to the piezo set point value that is programmed to be zero. The generated error value gives rise to a second control loop actuating on the cavity temperature. The heater compensator calculates the heater value and the DAC converts it into a voltage. The heating voltage leads to a second length response of the cavity. Together with the first one this triggers a response of the PDH error signal and closes the loop.

called "magic button" could be implemented during one morning after first tests suggested that it would be rather difficult to lock to the very same mode each time the cavity is relocked. Triggering the magic button causes the cavity locker to switch off the control mode, scan the piezos into the direction defined by the scan on/off switch and relock to the next mode (see appendix B). This very convenient way of frequency tuning is explained in chapter 4.2.7.

The PDH error signal has to be sufficiently big for the magic button function to work. Having the set point at 1.25 V the maximum of the error signal has to be bigger than 2 V and the minimum lower than 0.5 V. Otherwise the cavity locker can not identify the next mode. This thresholds, like all compensator gains and the scanning speed, can be changed via software.

A Labview program reads out the temperature, its set point and the piezo voltage via a serial port. The cavity temperature is limited to 50 °C by software, because the isolation material may be damaged by temperatures above this threshold. Exposing the cavity to high temperatures for longer times (i.e. over night) will shrink the isolation material and consequently misalign the cavity (see appendix B).

Some notes with practical advice for the reader that intents to achieve control over or operate the setup are summarized in appendix B.

| λ [nm] | $\Delta\lambda$ [nm] | ΔN | $\Delta\nu_2$ [MHz] |
|----------------|----------------------|------------|---------------------|
| 849.802 | 2.311 | 1915 | 1.4 |
| 854.209 | 2.096 | 1728 | 1.2 |
| 866.214 | 14.101 | 11462 | 8.3 |
| 793.694* | 58.419 | 51827 | 34.3 |
| 729.147** | 64.547 | 66920 | 40.7 |

Table 4.1.: Difference in cavity mode number for all lasers with respect to the reference laser at 852.113 nm for a confocal cavity with length $l=15$ cm. $\Delta\nu_2$ denotes the frequency shift of each laser caused by one mode hop (reference laser) of cavity. The wavelength data is taken from the NIST database. * The frequency shift for the 397 nm laser arises from doubling the one of the 793.694 nm laser. ** this laser has been temporarily stabilized with respect to the 793.694 nm master laser, all values are given with respect to the 793.694 nm laser.

4.2.7. Transfer lock

The resonance condition of a Fabry-Perot cavity for a laser with wavelength λ_i is $l = N \cdot \lambda_i / 2$ with N being the mode number and l the length of the cavity. For the frequency ν_i of the laser the condition can be written as

$$N \cdot FSR = \nu_i = \frac{c}{\lambda_i}, \quad (4.8)$$

where $FSR = \frac{c}{4l}$ (≈ 500 MHz for our cavity of length 15 cm) denotes the free spectral range of a confocal cavity and c the speed of light. In general two lasers with different frequencies ν_1 and ν_2 will not be both resonant to the same cavity for a given length. However, the cavity can always be brought to a resonance conditions for both lasers by tuning its length. The maximum length change necessary depends on the frequency difference of the two lasers.

If N and M are the mode numbers for the lasers with frequency ν_1 and ν_2 respectively, the difference in mode number for a given cavity length is

$$\Delta N = M - N = \frac{c}{FSR} \left(\frac{1}{\lambda_2} - \frac{1}{\lambda_1} \right) = \frac{c}{FSR} \cdot \frac{\Delta\lambda}{\lambda_1 \lambda_2} = 4l \frac{\Delta\lambda}{\lambda_1 \lambda_2}. \quad (4.9)$$

Table 4.1 shows the difference in mode number for our laser wavelength and cavities ($l=15$ cm) with respect to the reference laser at 852.113 nm. Imagine the cavity to be stabilized to the frequency ν_1 of the first laser. Jumping from one mode to the next one of this first laser by changing the length of the cavity will result in a different free spectral range FSR' according to the condition

$$\nu_1 = N \cdot FSR = (N + 1) \cdot FSR'. \quad (4.10)$$

The shift in frequency that arises for the mode of the second laser due to the length change is

$$\Delta\nu_2 = |(M + 1) \cdot FSR' - M \cdot FSR|. \quad (4.11)$$

4. Experimental setup

Substituting FSR' with 4.10 leads to

$$\Delta\nu_2 = \left| (M+1) \frac{N}{N+1} \cdot FSR - M \cdot FSR \right|. \quad (4.12)$$

Which with 4.9 and for large N can be simplified to

$$\Delta\nu_2 = \frac{|\Delta N|}{N+1} \cdot FSR \approx \frac{|\Delta N|}{N} \cdot FSR. \quad (4.13)$$

As mentioned in chapter 4.2.6 the cavity locker used for the stabilization of the cavities to the reference laser features a mode hope button called "the magic button". Triggering this button causes the cavity locker to lock to the next mode of the reference laser by changing the length of the cavity via the piezo. The formula 4.13 can be used to calculate the frequency shift of each laser associated with one mode hope by the cavity (see table 4.1). The table makes clear that using the magic button is only efficient if the wavelength of the laser is not too close to the one of the reference laser. In practice, already for the 866 nm laser temperature tuning results more efficient. Due to the frequency doubling the frequency shift for the 397 nm laser is 68.6 MHz, twice the shift for the 794 nm laser.

The smallest ratio of mode number difference and mode number among our lasers is the one for the 854 nm laser, $\frac{\Delta N_{854}}{N_{854}} = \frac{1}{406}$. This implies that for this laser, in the worst case, one has to jump 406 modes leading to a frequency shift of $406 \cdot \Delta\nu_{854}$ (one FSR) in order to find a common resonance. That means one has to be able to tune the length of the cavity by at least $\Delta l = 406 \cdot \frac{\lambda}{4} = 86 \mu\text{m}$. The temperature change ΔT needed to accomplish a linear thermal expansion of $\Delta L = 86 \mu\text{m}$ is given by the equation

$$\frac{\Delta L}{L_0} = \alpha_{Al} \cdot \Delta T. \quad (4.14)$$

With a cavity length $L_0 = 15 \text{ cm}$ and the thermal expansion coefficient of aluminum $\alpha_{Al} = 23 \cdot 10^{-6} \text{ K}^{-1}$, the maximal temperature change that the system needs to reach is $\Delta T = 25^\circ\text{C}$.

In practice we can only be sure to find a coincidence of the resonance condition for both lasers after a certain relative temperature change, not at an absolute temperature. The laser frequencies are given by the transitions of the ion and the only free parameter is the length of the cavity. It is possible to avoid the need of heating the cavity to too high temperatures by setting up the cavities in a certain way. Before adjusting the length of the cavity both lasers are brought to the desired frequency. Also the temperature of the cavity should be adjusted to the desired working point. After these two steps the coarse length adjustment is done by screwing the end cap of the aluminium tube in or out until the cavity modes of both lasers are symmetric. If the cavity is not confocal, higher modes are not degenerate with the TEM00 and TEM10 modes, which leads to an asymmetric mode shape. Following this procedure yields coincident resonances close to the initial temperature. In general the coarse length adjustment can be used to reach coincident resonances at any temperature.

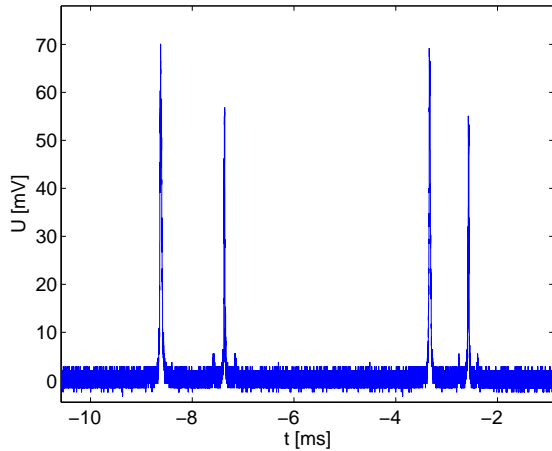


Figure 4.16.: Cavity transmission with 852 and 794 nm lasers coupled to the cavity. The length of the cavity was scanned with the piezos. To distinguish the two lasers the power of the 794 nm laser was reduced and the amplitude of the sidebands modulation has been increased until the sideband became visible. Due to the different wavelength the spacing between the modes differs for each mode pair.

An intuitive way to understand the transfer stabilization scheme is to imagine the resonance peaks of a Fabry-Perot cavity of the two lasers. Figure 4.16 shows two pairs of resonances for the 852 nm and the 794 nm lasers recorded with a photo diode in transmission of the cavity when the piezos are scanned. The time (x-)axis is equivalent to the length change of the cavity. To distinguish the two lasers the power of the 794 nm laser was reduced and the amplitude of the sideband modulation has been increased until the sidebands became visible. Only two mode pairs are shown since the cavity can maximally be scanned by three free spectral ranges. Due to the different wavelengths of the two lasers the spacing between modes of different lasers changes for each mode pair. It is obvious that for fixed laser frequencies an overlap of two modes can be reached (within a certain margin that is usually of the order of ~ 20 MHz, easy to compensate for by an acousto-optic modulator, see chapter 4.2.10) if the length is changed sufficiently.

In practice two modes are easily overlapped by shifting the resonances of the second laser, tuning its frequency with the offset of the piezo. For this purpose the frequency of the second laser is scanned and the reference laser and the cavity stay locked to the Cs transition. Tuning the piezo offset changes the wavelength of the second laser.

In day to day operation the laser is locked to the next best mode and the wavelength is checked with the wavemeter. In case the wavelength is far off the desired transition wavelength the second laser has to be shifted one or several full spectral ranges using the offset of the piezo. If the mode closest to the desired wavelength is found, the magic button or temperature tuning of the cavity length is necessary

4. Experimental setup

to account for the residual frequency shift. Using the magic button is equivalent to jumping to the next mode pair, i.e. to the next mode for both lasers. As opposed to tuning to the next mode using the piezo offset for the second laser only. The latter yields a frequency shift of one FSR, the use of the magic button the shift specified in table 4.1.

4.2.8. Systematic errors

For high precision spectroscopy and quantum information tasks the laser frequency has to be stabilized well below the natural linewidth of the respective transition in $^{40}\text{Ca}^+$, in order to reach good resolution and well-defined excitation conditions. Since experiments are usually very complex and data acquisition can take many hours or even days, also a very good long term stability is required, i.e. the laser frequency must not drift with respect to the absolute transition frequency during an experimental run. Generally, at the wavelengths needed for ions there are no vapor cells available that could be used as frequency reference via spectroscopy. The usual approach is to lock the lasers to stable Fabry-Perot cavities and to correct for residual drifts with an AOM or by locking to the next cavity mode if necessary. These cavities are often build from expensive ultra low expansion materials and are placed in temperature stabilized vacuum vessels or pressure sealed containers to minimize possible drifts [99]. The absolute wavelength can be adjusted using a precise wavemeter and by monitoring the fluorescence signal of the ion.

As outlined in the previous chapters, we followed a different approach to fulfill the requirements of long term stable high precision spectroscopy. This approach allows the use of cheap open (at ambient pressure) tabletop cavities without the need for a vacuum setup and ultra low expansion materials. In our setup the length of the transfer cavity is stable with respect to the atomic reference at all times and the cavity temperature can be considered constant.

As described in chapter 3.3 the reasons for low frequency noise or instabilities over long time scales are mainly due to environmental influence like temperature and pressure fluctuations. In the following the effect of such fluctuations on a transfer stabilization are estimated. To distinguish between the reference laser and the second laser that is to be stabilized, the latter one will be called spectroscopy laser in the following. The discussion will be restricted to the influence of temperature and pressure on the resonance frequencies of the cavity (for the reference laser at the Cs wavelength and spectroscopy laser) and its consequences on the frequency of the spectroscopy laser [100], which constitute the biggest effects.

The resonance condition for the frequency ν of the longitudinal mode of a confocal Fabry-Perot resonator is

$$\nu = \frac{Nc_0}{4nd}, \quad (4.15)$$

with c_0 the speed of light in vacuum, n the refractive index of the medium between the mirrors, d the distance between the mirrors and N the mode number. For the reference laser at 852.33496 nm the refractive index of air under our lab conditions

4.2. Laser Setup

($p_0 = 1013.25$ mbar, $T_0 = 23$ °C) and 50 % relative humidity is $n = 1.000266801$ according to the modified Edlén equation [101]. A pressure change δp at constant temperature leads to a change of the density of the air inside the cavity and consequently to a shift in resonance frequency $\nu + \delta\nu$. Since $(n - 1)$ is linearly proportional to the density of the air [102] between the mirrors the new resonance frequency reads

$$\nu + \delta\nu = \frac{Nc_0}{4[n + (n - 1)\frac{\delta p}{p_0}]d} \approx \frac{Nc_0}{4nd} \left(1 - \frac{n - 1}{n} \frac{\delta p}{p_0}\right). \quad (4.16)$$

With 4.15 and 4.16 one finds

$$\delta\nu \approx -\frac{n - 1}{n} \frac{\delta p}{p_0} \nu \approx -(n - 1) \frac{\delta p}{p_0} \nu. \quad (4.17)$$

At the wavelength of our reference laser the frequency deviation of the cavity due to a pressure change near ambient pressure is $\frac{\delta\nu}{\delta p} = -92.6$ MHz/mbar. Hence for a non actively stabilized cavity the pressure would have to be controlled down to $1.6 \cdot 10^{-3}$ mbar to achieve a stability of 150 kHz.

A temperature change affects the cavity modes in two ways. First, for an open cavity the consequent density change caused by the temperature deviation leads to a similar shift as discussed in the previous paragraph. And second the spacing of the mirrors will be changed due to thermal expansion of the spacer and mirror mounts.

The frequency change due to temperature induced pressure change can be estimated as

$$\delta\nu \approx (n - 1) \frac{\delta T}{T_0} \nu, \quad (4.18)$$

This amounts to a drift of $\frac{\delta\nu}{\delta T} = 317$ MHz/K of the 852 nm reference laser for atmospheric pressure. One should point out that this effect has the opposite sign as the direct pressure influence and therefore compensates the latter to a certain degree.

The direct influence of the temperature on the resonance frequency of the cavity mode is estimated using the thermal expansion coefficient α of the spacer material

$$\nu + \delta\nu = \frac{Nc_0}{4nd(1 + \alpha\delta T)} \approx \frac{Nc_0}{4nd} (1 - \alpha\delta T), \quad (4.19)$$

or

$$\delta\nu \approx -\alpha\delta T \nu. \quad (4.20)$$

For aluminium $\alpha = 23 \cdot 10^{-6}/\text{K}$ and $\frac{\delta\nu}{\delta T} = -8$ GHz/K. For fused silica $\alpha = 0.55 \cdot 10^{-6}/\text{K}$ and $\frac{\delta\nu}{\delta T} = -193$ MHz/K. This means that the temperature of the cavity would have to be controlled to about $2 \cdot 10^{-5}$ K in order to achieve a frequency stability of 150 kHz.

These values confirm that the cavity resonance frequency is extremely sensitive to ambient pressure and temperature. Consequently the length of the cavity has to be stabilized very well to compensate for any change of these variables if it is to be

4. Experimental setup

used to transfer stability from the stable reference laser to another laser. Experimentally we achieve this with the setup described in the previous chapters. The frequency shifts caused by the lab environment, which naturally does not fulfill the above extreme stability conditions, are compensated for by the combined piezo and temperature stabilization action. Nevertheless, the frequency shift of a cavity mode depends on the refractive index of the medium in the cavity at the corresponding wavelength. The refractive index of air, on the other hand, is dependent on the wavelength and therefore there is a residual shift of the frequency of the spectroscopy laser due to the different indices at the wavelengths of the two lasers. It turns out that this differential shift is the limiting factor of our transfer system. A quantitative approximation is derived in the following.

We consider the temperature of the cavity to be stable due to the active stabilization. The discussion will therefore be restricted to the pressure influence. In the general case for non constant temperature, the effect of the pressure change due to temperature fluctuations is obtained in a similar fashion by comparing 4.17 and 4.18.

Locking the mode number N_{ref} of our confocal cavity to the frequency ν_{ref} of our reference laser at ambient pressure p requires the length d of the cavity to be

$$d = \frac{N_{ref}c_0}{4\nu_{ref}} \frac{1}{1 + (n_{ref} - 1) \frac{p}{p_0}} \approx \frac{N_{ref}c_0}{4\nu_{ref}} \left(1 - (n_{ref} - 1) \frac{p}{p_0} \right). \quad (4.21)$$

The stabilization feedback will compensate a pressure change δp by adjusting the length to $d + \delta d$, with

$$\frac{\delta d}{\delta p} \approx \frac{-N_{ref}c_0}{4\nu_{ref}} (n_{ref} - 1) \frac{1}{p_0}. \quad (4.22)$$

Considering only first order changes in length we can set the refractive index in 4.21 equal to 1 and write 4.22 as

$$\delta d \approx -d(n_{ref} - 1) \frac{\delta p}{p_0}. \quad (4.23)$$

Before the pressure change, a second cavity mode with mode number N_{laser} resonant with the spectroscopy laser at frequency ν_{laser} , will obey the condition

$$\nu_{laser} \approx \frac{N_{laser}c_0}{4d} \left(1 - (n_{laser} - 1) \frac{p}{p_0} \right) \quad (4.24)$$

in analogy with 4.21. Because the stabilization will change the cavity length by δd in order to keep the cavity locked to the reference laser correcting for the pressure change δp , the frequency of the spectroscopy laser mode will be changed by $\delta\nu_{laser}$ according to

$$\nu_{laser} + \delta\nu_{laser} = \frac{N_{laser}c_0}{4d} \left(1 - \frac{\delta d}{d} \right) \left(1 - (n_{laser} - 1) \frac{p + \delta p}{p_0} \right). \quad (4.25)$$

4.2. Laser Setup

Substituting equation 4.23 and discarding all non linear terms one finds

$$\delta\nu_{laser} \approx \frac{N_{laser}c_0}{4d} \frac{\delta p}{p_0} (n_{ref} - n_{laser}) \approx \nu_{laser} \frac{\delta p}{p_0} (n_{ref} - n_{laser}). \quad (4.26)$$

Equation 4.26 tells us that there is a remaining error resulting from the different refractive indices of air at the wavelengths of the reference laser and the spectroscopy laser. The closer the wavelengths of the two lasers are, the smaller is the frequency deviation caused by a pressure change.

The wavelengths of most of the lasers in our experiment are fairly close to the 852 nm reference laser. The one which is furthest away is the master laser of the frequency doubling stage at 795 nm. The refractive index of air for our laboratory conditions at this wavelength is $n_{795} = 1 + 2.67117 \cdot 10^{-4}$. Together with the refractive index of the reference laser $n_{ref} = 1 + 2.66801 \cdot 10^{-4}$ this results in a residual error of $\frac{\delta\nu_{795}}{\delta p} = 118 \text{ kHz/mbar}$. In other words, a pressure fluctuation of 10 mbar will lead to a significant frequency error of 1 MHz.

The other three stabilized lasers are much closer to the reference laser in frequency. The effect scales approximately linearly with the difference in wavelength. That means a shift about four times less for the laser at 866 nm, $\frac{\delta\nu_{866}}{\delta p} = 30 \text{ kHz/mbar}$, and as much as 30 times less for the lasers at 850 and 854 nm, $\frac{\delta\nu_{850/854}}{\delta p} = 4 \text{ kHz/mbar}$.

In contrast to the temperature, the pressure is not regulated in our lab. Depending on the weather conditions the atmospheric pressure can change up to 10 mbar during a day in a bad case. Although our cavity is not completely open, it is closed by the thread of a lens tube mount but not sealed in any way, it is considered that pressure changes get transferred more or less immediately into the housing. From the results presented in chapter 4.2.13 and the considerations in this chapter it is deduced that the stability of our transfer lock is limited by pressure fluctuations. This is consistent with the sensitivity to acoustic noise experienced in the every day operation of the experiment. The error signals of the locks are sensitive to all sorts of air acoustics caused by slamming doors, clapping hands or loud voices. On the contrary, body acoustic noise like vibrations and shocks do affect the error signals very little. The stabilization chain stayed in lock with a compressed air hammer working 15 m away in another room of the same building.

4.2.9. Locking procedure

To lock the whole chain the following procedure has to be performed. The reference laser is brought to resonance with the Cs D2 line ($F = 3 \rightarrow F' = 3/4$, cross over line) by adjusting the laser current and piezo offset. It is important to stay close to the typical laser values (I=177 mA, Offset=2.3) in order not to confuse the resonance from the hyperfine ground-state levels $F = 3 \rightarrow F' = 2, 3, 4$ with the one from $F = 4 \rightarrow F' = 3, 4, 5$ which is only 9 GHz away [97]. The reference laser is scanned and then locked to the cavity mode which is closest to the absorption signal. The offset of the cavity locker scan module should be set to the mid-position and the temperature should be set to the desired value before hand. For the procedure the

4. Experimental setup

| λ [nm] | I [mA] | Offset [a.u.] | T [$^{\circ}$ C] | T _{cavity} [$^{\circ}$ C] |
|----------------|--------|---------------|-------------------|-------------------------------------|
| 852.10076 | 177 | 2.3 | 25.3 | |
| 866.21450 | 102 | 3.1 | 20.0 | 37.0 |
| 854.20906 | 208 | 7.2 | 20.1 | 33.4 |
| 793.69971 | 165 | 4.5 | 21.1 | 36.5 |

Table 4.2.: Wavemeter readings and typical laser and cavity parameters

cavity temperature should be well stabilized. Once the laser is locked, the cavity is scanned with a frequency slow enough that the laser follows. When the spectroscopic signature of the reference transition in Cs appears on the oscilloscope, the feedback loop is closed and the laser is locked to it.

Once the reference laser and first cavity are stabilized, the 866 nm laser is locked to the same cavity. The resulting wavelength is checked with the wavemeter immediately. If the desired wavelength is between two cavity modes, the temperature has to be fine tuned and the locking procedure for the reference laser starts from the beginning. Although the desired 866,21450 nm are reached routinely with a constant cavity temperature, noise due to pick up in the temperature sensor cable can lead to slight variations of this temperature on the timescale of a few days. Since in control mode the temperature stabilization is programmed to keep the piezo in the middle of its range, the temperature will deviate slightly from the original set point after longer locking periods. This is why after adjusting the temperature of the cavity the "hold mode" has to be activated. In this mode the set point is set to the last temperature read out when the controller is switched off. The temperature is kept at the same value until the cavity is locked again. Otherwise the temperature drifts back to the value defined by the potentiometer.

After this, all other cavities are locked to the reference laser, and their respective lasers onto the cavities. The method for compensating any residual detuning depends on the magnitude of the wavelength difference to the reference laser. If the difference is big enough, the "magic button" can be used (chapter 4.2.6 and 4.2.7). If the difference is too small, jumping to the next mode pair yields only a very small frequency shift and is not efficient. For the 794 nm laser one jump with the magic button corresponds to a wavelength shift of 60 MHz which is very convenient for tuning it to the resonance. For the 850 nm and 854 nm lasers temperature tuning results more efficient. Typical values for laser current, offset, temperature, laser wavelength and cavity temperature are found in table 4.2. In order to reach the indicated resonance these values should be followed. All wavelength values are measured with a commercial wavemeter ²⁴ with 60 MHz absolute accuracy. The next chapter explains how the laser frequencies are fine tuned with higher resolution.

²⁴High Finesse WS7 super precision

4.2.10. Radio Frequency Drive

The fine tuning of the laser frequencies is done with Acousto-Optical-Modulators (AOM) which are controlled by a radio frequency. The phase and amplitude of the radio frequency applied to the AOM get imprinted onto the phase and amplitude of the light passing through it. AOMs therefore offer unique pulse shaping properties that are used to create the complex pulse sequences needed in quantum information processing. In the early days of ion trapping, pulse sequences were produced by complicated radio frequency networks consisting of a number of very stable analog synthesizers, switches and phase shifters [35]. Nowadays digital technology opens up new possibilities.

Several groups have developed devices based on Direct Digital Synthesizers (DDS) and Field Programmable Gate Arrays (FPGA) [103, 104]. A FPGA is programmable hardware implemented on an integrated circuit. The standard approach is that the FPGA controls several DDSs such that they execute the desired pulse sequence. DDSs are cheap and precise integrated-circuit RF-sources. The FPGA can be easily reprogrammed via a PC and controls the DDSs independent from the computer.

In our group we developed our own FPGA-based²⁵ pulse sequencer. The essential difference of our device from the previous projects is the use of not only one powerful FPGA but several less powerful ones. Each DDS is controlled by an FPGA²⁶ that communicates with a Digital Signal Processor²⁷ (DSP) via a LVDS²⁸ backplane. The DSP constitutes the heart of the system and uses an additional FPGAs for backplane communication.

Two types of DDS cards for the 19" rack system have been developed. Each card comprises one FPGA that manages the communication with the backplane. The first type contains two DDSs and the second contains one DDS plus an additional analog input which offers the option of regulating the RF output amplitude. The latter can be used for example for laser intensity stabilization.

The instructions for a certain sequence are saved directly in the FPGA of each card before the sequence is executed. The DSP does not have to send the full sequence but only a signal triggering the saved commands. The clock frequency is 80 MHz, which means that the frequency can be updated as fast as in 12.5 ns. The rack can take up to 14 cards. Due to the fact that processing power is distributed over several cards and the analogy of this structure to the serpent-like beast with numerous heads from Greek mythology, the device was baptized HYDRA.

HYDRA is programmed via a user-friendly visual-C based software. It also contains two counters for the read out of photo-detectors. The device is subject of another PhD thesis, in which it is described in full detail [84].

²⁵XILINX Spartan 3, XC3S200

²⁶Analog Devices AD9858 1 GS/s

²⁷Texas Instruments TMS320C6455 1 GHz

²⁸Low Voltage Differential Signaling

4. Experimental setup

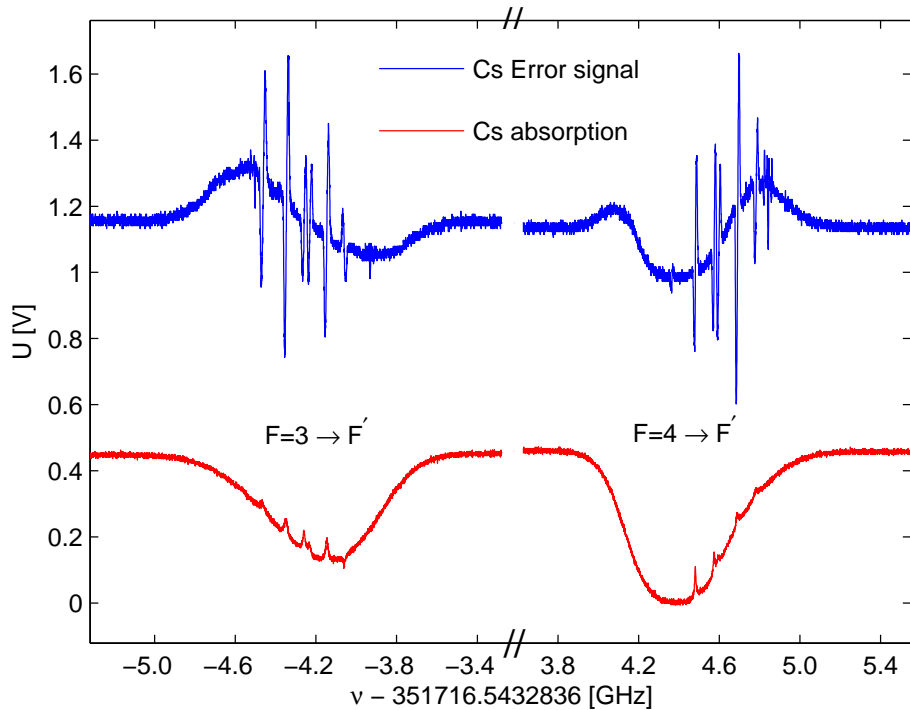


Figure 4.17.: Cs doppler free absorption spectroscopy signal (lower trace) and the corresponding error signal (upper trace) produced by the cavity locker electronics. The x-axis shows the absolute frequency of the transitions. The hyperfine splitting between the $F=3$ and $F=4$ ground state levels is 9.2 GHz.

4.2.11. Cs spectroscopy

The setup for the Doppler free absorption spectroscopy at the Cs cell is displayed in the upper part of figure 4.22. A small portion of the 852 nm light going to the transfer cavity is sent into the Cs cell as the pump beam. The light transmitted through the cell gets reflected at a mirror and passes twice through a $\lambda/4$ plate changing its polarization. The reflected beam acts as the probe beam and gets detected by the photo diode PD1 after the polarizing beam splitter. The detected absorption signal is shown in figure 4.17 together with the corresponding error signal produced by the Pound-Drever-Hall part of the cavity locker. The hyperfine ground state splitting of 9.2 GHz between the $F=3$ and $F=4$ state is used to calibrate the frequency axis. In figure 4.18 and figure 4.19 the Doppler free transitions from the $F=3$ and $F=4$ ground states are depicted respectively. All hyperfine transitions are resolved and identified. The transition used as reference is the $F = 3 \rightarrow F' = 3/4$ cross over transition. The little distortion to the left of the $F = 3 \rightarrow F' = 4$ and to the right of the $F = 4 \rightarrow F' = 3$ fringe is caused by the direct feedback of the transfer cavity error signal onto the laser current. The laser is scanning across a

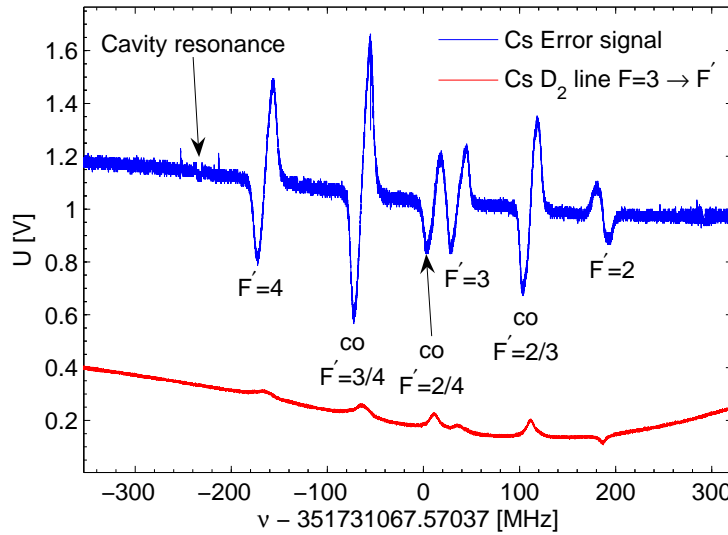


Figure 4.18.: Cs doppler free absorption spectroscopy signal (lower trace) and the corresponding error signal (upper trace) for the $F = 3 \rightarrow F' = 2, 3, 4$ and its cross over transitions. The x-axis shows the absolute frequency of the transitions.

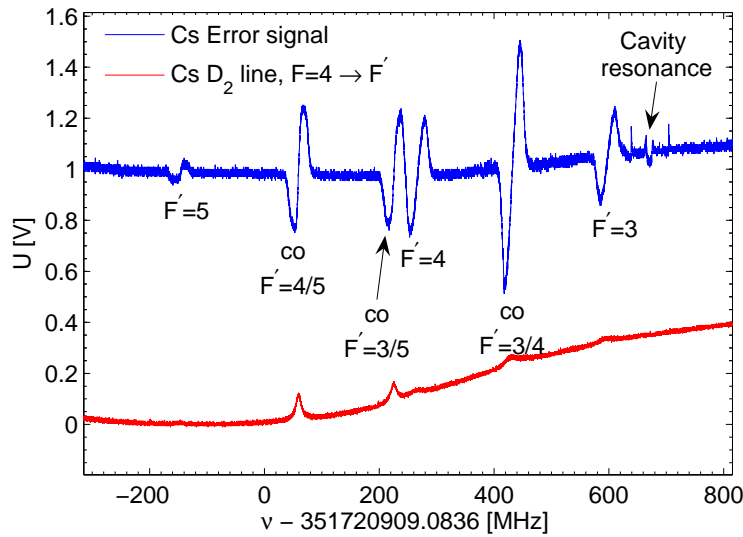


Figure 4.19.: Cs doppler free absorption spectroscopy signal (lower trace) and the corresponding error signal (upper trace) for the $F = 4 \rightarrow F' = 3, 4, 5$ and its cross over transitions. The x-axis shows the absolute frequency of the transitions.

4. Experimental setup

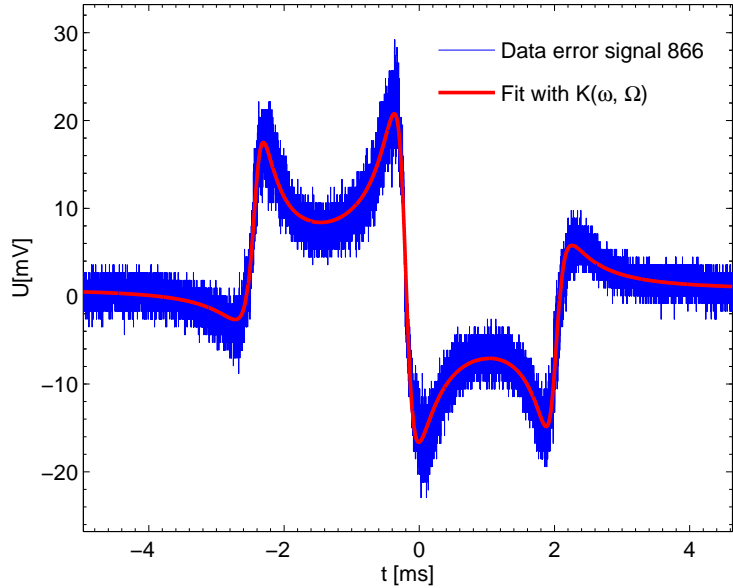


Figure 4.20.: Pound-Drever-Hall error signal of the 866 nm laser (noisy trace) and fit of $K(\omega, \Omega)$ to the data (smooth trace). The fit is used to determine the root mean square (rms) frequency deviation of the laser with respect to the transfer cavity. A typical value for all diode lasers is 40 kHz of rms deviation.

cavity resonance at this point. The feedback is working against the scan of the piezo, trying to regulate the frequency to the cavity mode. This causes the effective frequency scan to be slower for a moment and distorts the Cs error signal.

4.2.12. Characterization of the individual stabilizations

To characterize the stability of the individual Pound-Drever-Hall locks of the lasers to the cavities, the root mean square frequency deviation with respect to the cavity was measured. For this purpose the error signal of each laser was fitted with the function $K(\omega, \Omega)$ which is derived in appendix D.

$$K(\omega, \Omega) = N \exp^{-i\Phi} (f(\omega)f^*(\omega + \Omega) + f^*(\omega)f(\omega - \Omega)) + M(f(\omega)f^*(\omega + \Omega) - f^*(\omega)f(\omega - \Omega)) \quad (4.27)$$

according to [105] with

$$f(\omega) = \frac{r(\exp(i\frac{\omega}{\Delta\nu_{fsr}}) - 1)}{1 - r^2 \exp(i\frac{\omega}{\Delta\nu_{fsr}})} \quad (4.28)$$

The Matlab files used for the fit can be found in appendix E. First the file `find_b0.m` is used to find the initial values used for the fit. The file plots the data of the error signal recorded with the oscilloscope and $K(\omega, \Omega)$. Changing the starting

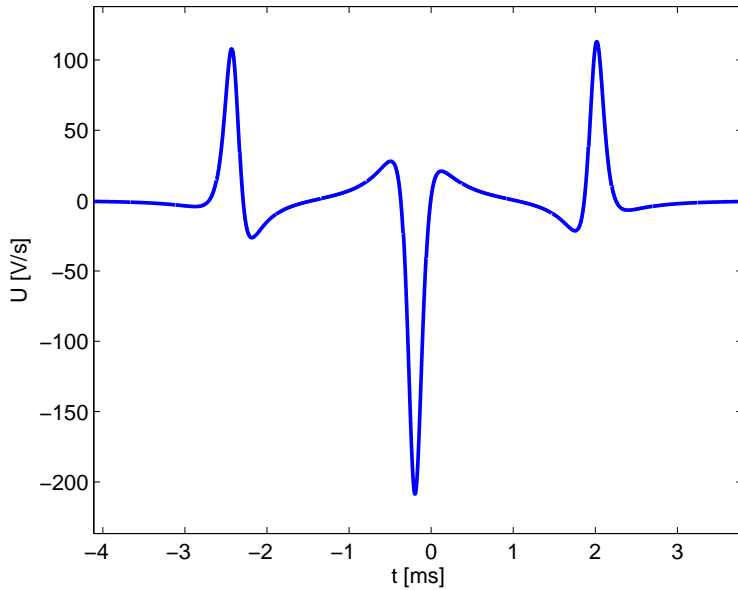


Figure 4.21.: Slope of the fit to the 866 nm Pund-Drever-Hall error signal (figure 4.20). The steepest slope (set point of the stabilization) is used to gauge the frequency axis of figure 4.20 and to calculate the root mean square frequency deviation from the in loop signal.

parameters, like the amplitude of the phase and amplitude modulation, offsets, the phase of detection etc., and running `find_b0.m` iteratively, the data and $K(\omega, \Omega)$ are matched. When a good overlap has been reached, the starting parameters for the fit `b0` are plugged into the fitting routine `fit_PDH.m`. This file fits the data with $K(\omega, \Omega)$ and plots both, data and fit. Figure 4.20 shows such plot for the error signal of the 866 nm laser.

A third Matlab file, `slope.m`, calculates the slope of the fit of the error signal, plots it and returns position and value of the maximum and minimum slope. A plot of the slope of the error signal from figure 4.20 is shown in figure 4.21. Using the zero crossings of the side band features and the known modulation frequency (20 MHz) the frequency axis is gauged. From the in-loop error signal recorded over 2 ms the root mean square deviation is calculated and converted into frequency deviation. The root mean square frequency deviation of our diode lasers, with respect to the transfer cavities, measured in the way described above, is 38 kHz.

4.2.13. Characterization of the transfer lock

To estimate the absolute stability of the transfer locked lasers they were compared with an independent atomic reference, a rubidium gas cell. For this purpose a second Doppler free absorption spectroscopy was set up and the master laser of the

4. Experimental setup

frequency doubling stage was tuned to the D1 line of ^{85}Rb at 794.979 nm [106]. In contrast to the characterization in chapter 4.2.12, where the stability with respect to the transfer cavity was determined, the rubidium cell acts as an absolute and independent frequency reference. In figure 4.22 the setup is shown as it was mounted on the optical table. The laser is locked to a Cs transition by three consecutive Pound-Drever-Hall stabilizations as described in the previous sections: a reference laser is locked to a cavity, the cavity is locked to the Cs resonance and the laser is stabilized to the reference using the transfer cavity.

The comparison is done by generating a Pound-Drever-Hall error signal from the saturated absorption spectroscopy signal on ^{85}Rb . The laser light is modulated at 20 MHz in order to lock it to its transfer cavity as described in chapter 4.2.4. The Doppler-free saturated absorption signal recorded with a fast photo diode (PD2)²⁹ behind the Rb cell is amplified, mixed down with a mixer³⁰ and filtered by a bandpass filter³¹. In analogy to figure 4.11, a schematic of the electronics used for the measurement is shown in figure 4.23.

The full Rb Doppler-free absorption signal that is obtained by scanning the frequency of the laser is depicted in figure 4.24. Since the cell contains Rb isotopes in their natural abundances, absorption lines for ^{85}Rb (72.2 %) and ^{87}Rb (27.8 %) are observed. The Doppler free hyperfine structure is well resolved and the frequency axis was calibrated using the literature value [107] of the ground state hyperfine splitting (between the $F = 1 \rightarrow F = 2'$ and $F = 2 \rightarrow F = 2'$ D1 lines of ^{87}Rb) of $\delta\nu = 6.8\text{ GHz}$. The different hyperfine dips are easily identified using the splittings known from the literature [108, 107].

With the whole stabilization chain locked, i.e. the master laser at 795 nm is locked via the transfer cavity to the stable reference laser, the laser was brought as close as possible to the strongest line in ^{85}Rb , the $F = 3 \rightarrow F' = 2/3$ crossover line, using the magic button. Finally an AOM is used for fine tuning. Scanning the AOM one can identify the desired transition and set the frequency to resonance, which is equivalent to the point with the steepest slope of the error signal on the oscilloscope. Figure 4.25 shows the error signal of the $F = 3 \rightarrow F' = 2/3$ crossover line obtained by scanning the AOM. Due to the limited bandwidth (80 MHz) of the AOM only one hyperfine transition can be scanned in this way.

The error signal also serves for converting the voltage recorded with the oscilloscope into frequency. For this purpose the AOM is linearly scanned with an amplitude of $\pm 2\text{ MHz}$ around the resonance. The recorded slope is fitted linearly to determine the conversion factor between frequency and voltage for each measurement.

To measure the short term stability of the locking chain, the signal was recorded for a fixed AOM frequency at three different times during one day over a time span of 200 ms with different sampling rates. From the voltage trace on the oscilloscope, rms

²⁹New Focus model 1801 (Bandwidth 125 MHz)

³⁰Mini Circuits ZAD-1H

³¹Mini Circuits SIF-21.4+

4.2. Laser Setup

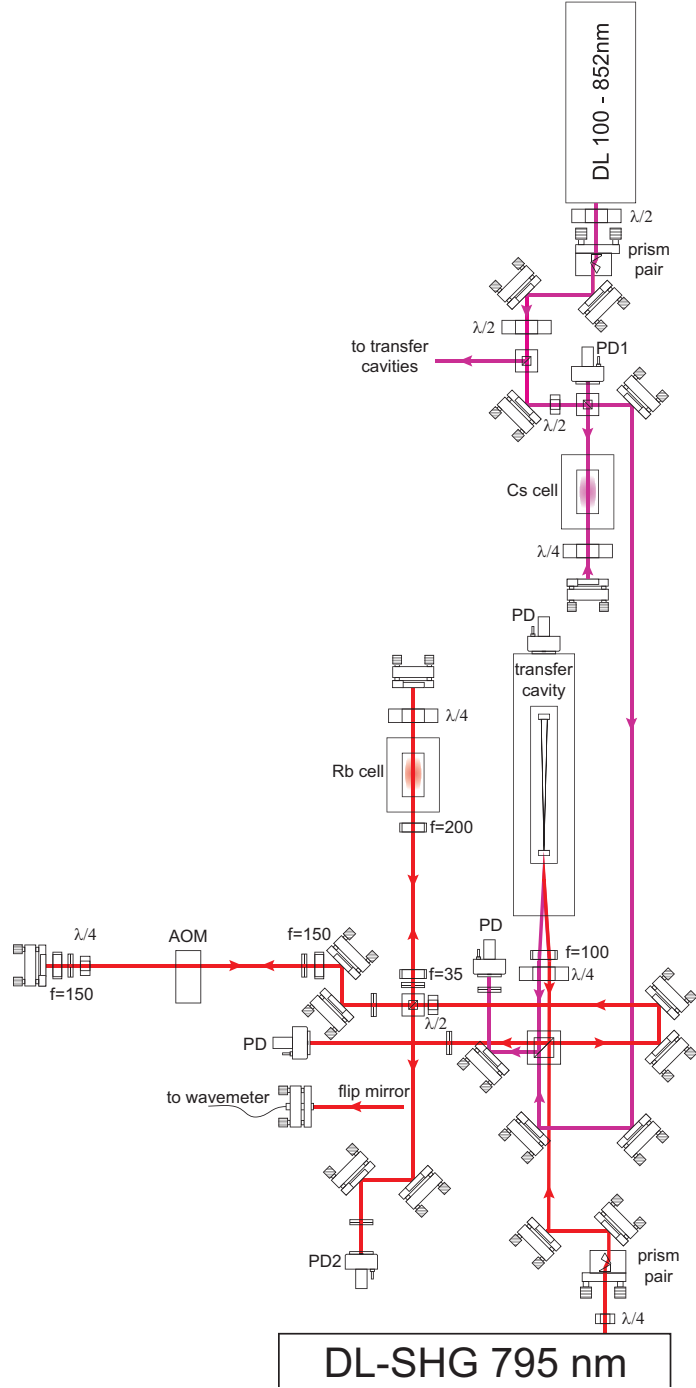


Figure 4.22.: Setup for the characterization of the locking chain. The master laser of the frequency doubling stage at 795 nm is locked to a Cs transition by three consecutive Pound-Drever-Hall stabilizations using a transfer cavity. A PDH error signal is derived from a Doppler-free absorption spectroscopy on ^{85}Rb . An AOM tunes the laser to the D1, $F = 3 \rightarrow F' = 2/3$ crossover line. Monitoring the error signal with an oscilloscope reveals the absolute stability of the locking scheme.

4. Experimental setup

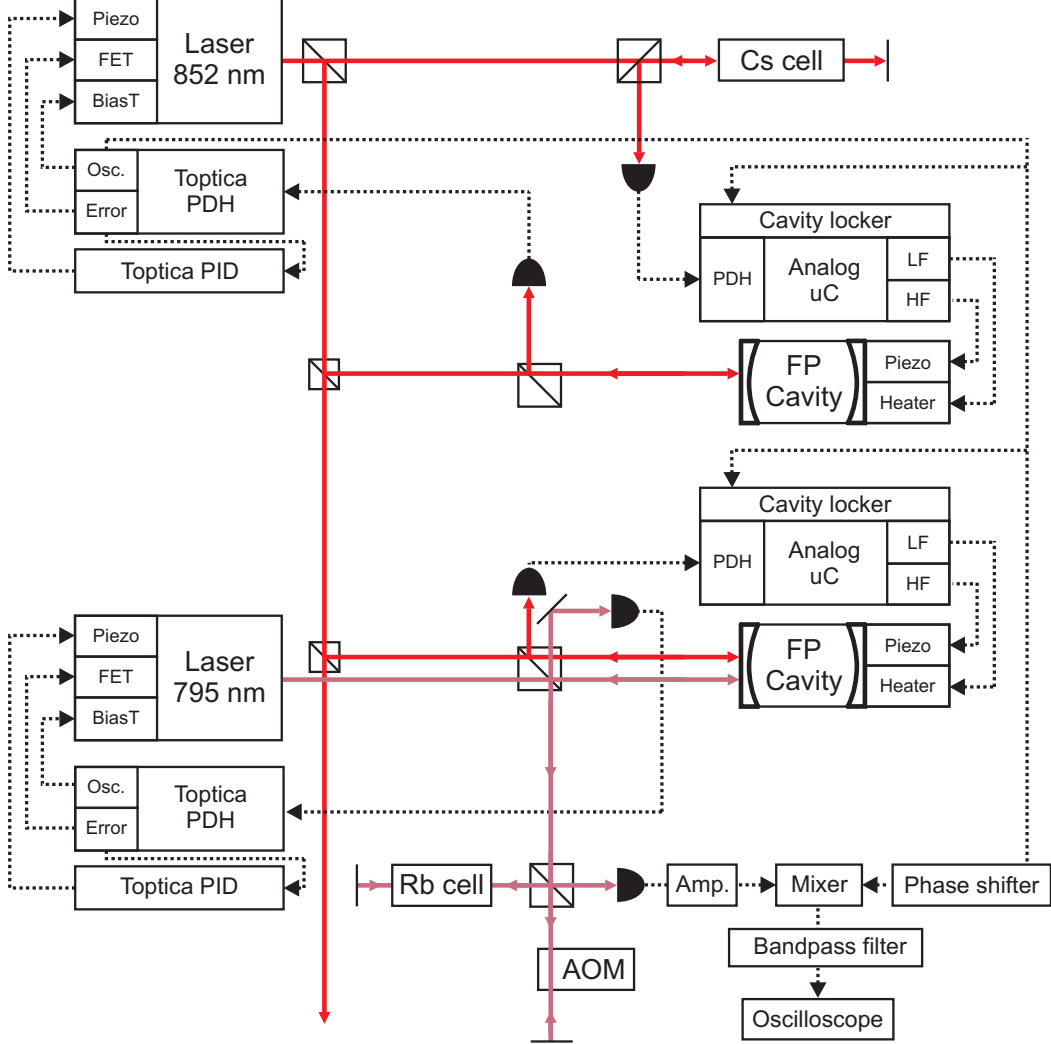


Figure 4.23.: Schematic of the electronics used for the characterization of the transfer lock.

deviations of 143 kHz, 123 kHz and 133 kHz were measured, respectively. Recalling the result of 38 kHz for a single Pound Drever lock from chapter 4.2.12, the stability of 123 kHz for three consecutive locks is consistent with the former measurement. However the result from the spectroscopy measurement is more relevant as it has been measured with respect to an independent reference and can be transferred to the Ca^+ spectroscopy.

In order to measure the long term stability of the setup, the mean value of the voltage was recorded with a PC. A Labview program read out the voltage from the oscilloscope and stored the mean value over the time $\Delta\tau = 1\text{s}$ for a duration of 3 hours. In the particular data set analyzed here the laser fell out of the lock after 2 hours. However, much longer locking times are typically observed in a daily

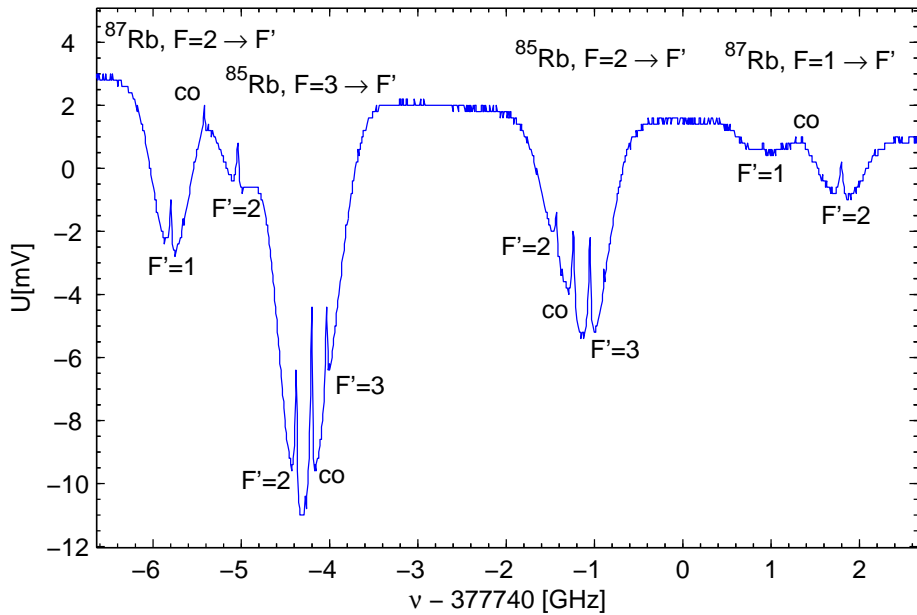


Figure 4.24.: Full Rb spectrum obtained via Doppler free absorption spectroscopy.

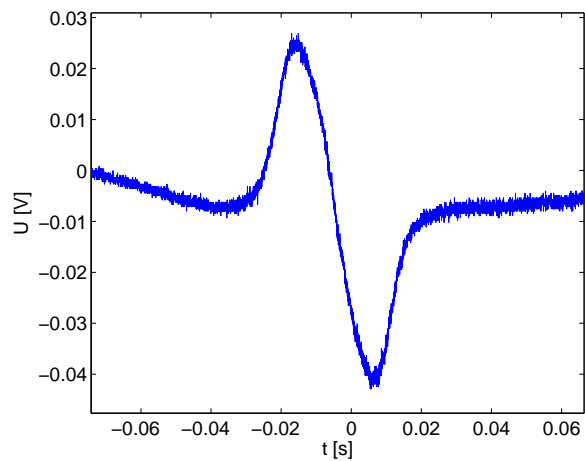


Figure 4.25.: Error signal of the $^{85}\text{Rb}, F = 3 \rightarrow F' = 2/3$ crossover line. The signal was recorded by scanning an AOM with the laser locked to an atomic Cs reference by the transfer stabilization scheme.

4. Experimental setup

routine. The mean value ($\Delta\tau = 1$ s) of the error signal drifted about one short-term rms deviation ($\Delta t = 200$ ms), i.e. about 130 kHz, during these two hours. The main cause of instability is due to acoustic noise or pressure drifts. According to the analysis in chapter 4.2.8 the observed drift is equivalent to a pressure change of 1mbar. Since the pressure is not controlled in any way in our lab, it is reasonable to assume that the frequency drift is caused by a pressure drift. The daily cyclic variation of the atmospheric pressure is on the order of 1mbar for our latitudes. However, this variation is usually superimposed by dynamic pressure fluctuations. For drastic weather changes the pressure variation can get up to several mbar, what can be considered rather the exception than the norm in daily operation.

Altogether one can assume that the stabilization scheme is precise on the order of few hundreds of kHz on an absolute scale over some days. Due to the smaller difference in wavelength with the reference laser, the stability of the lasers at 850, 854 and 866 nm is much better than the one measured for the 795 nm laser. On the time scale of the short-term rms fluctuations the frequency of these lasers can be considered practically drift-free. The presented scheme meets very well the requirements of sub-MHz long-term stability. It is particularly well suited for measurements with low count rate that require stable conditions over a long time period. For the longest experimental run until the completion of this thesis, stable conditions over 40 hours could be achieved. The stabilization was interrupted only by very short periods caused by acoustic noise or instabilities in the laser diodes. During this time no noticeable frequency drift on the MHz scale was observed with respect to the excitation spectrum of a single ion.

For a full characterization of the stability of the 795nm laser oscillator the Allan variance was calculated from the three short-term measurements as well as from the long-term measurement. As described in chapter 3.2 the Allan variance is based on the differences of adjacent frequency values rather than on differences with respect to the mean. Practically it is determined by sampling the voltage of the error signal at resonance with the oscilloscope. The fractional frequency deviation $y(t)$ is calculated through the calibration of the error signal obtained by the mentioned linear scan of the AOM (± 2 MHz). Furthermore, the mean value \bar{y}_{i,τ_0} of the fractional frequency deviation over the shortest time duration τ_0 , at which the Allan variance is to be determined, is calculated. It is important that there is no dead time between two subsequent values. From these data \bar{y}_{i,τ_0} the Allan variance for time τ_0 is calculated according to 3.12. For all longer times the values are obtained by post processing. The new values for times $2\tau_0$ are calculated by averaging over two adjacent data points respectively, $\bar{y}_{1,2\tau_0} = (\bar{y}_{1,\tau_0} + \bar{y}_{2,\tau_0})/2$, $\bar{y}_{2,2\tau_0} = (\bar{y}_{3,\tau_0} + \bar{y}_{4,\tau_0})/2$, $\bar{y}_{3,2\tau_0} = \dots$. For all other times $\tau = n \cdot \tau_0$ that are multiples of τ_0 one has to proceed accordingly. A Matlab code to calculate the Allan variance from a given data set \bar{y}_{i,τ_0} is found in appendix C.

The Allan variance calculated from the four different data sets is plotted in figure 4.26. All three measurements over 200 ms show good agreement between $\tau = 10^{-4}$ and $\tau = 10^{-2}$ s. The Allan variance decays with τ^{-1} over two orders of magnitude down to the $\sigma_y^2 = 10^{-22}$ region. According to chapter 3.3 this indicates the presence

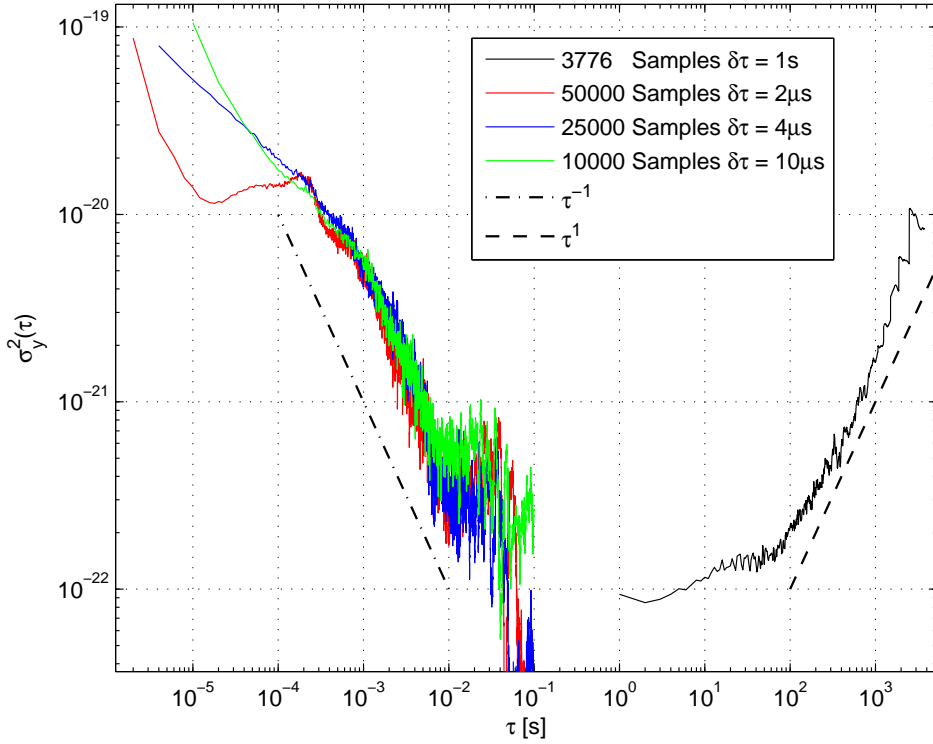


Figure 4.26.: Allan variance for three short term measurements with different sampling rate and an measurement duration of 200 ms and one long term measurement with integration time of 2 h. The dashed line (τ^{-1}) indicates the dominating white frequency noise for high frequencies. The dotted line (τ^1) indicates the dominating random walk frequency noise for long time scales.

of white frequency noise caused in electronic components. It is expected that the accuracy of an oscillator increases with further integration time until other effects, such as long term drifts, start to dominate. In accordance with this the Allan variance for the long-term measurement rises again starting from $\tau = 10^2$ s up to $\tau = 10^4$ s. The slope is proportional to τ^1 indicating that the dominant noise type is a random walk of frequency noise caused by the environmental conditions. This is in agreement with the observation of high sensitivity to pressure fluctuations in this chapter and the analysis in chapter 4.2.8. Long and short-term measurements seem to connect quite well for time scales of $\tau = 10^{-2}$ to 10^1 s. Although there is some data missing, a flat behavior of $\sigma_y^2 \propto \tau^0$ may be assumed in that region. This suggests an expected flicker noise floor for low frequencies.

Two of the short-term measurements drop drastically for some time values close to $\tau = 10^{-1}$ s. The Allan variance at this points is calculated from very few points, i.e. the value at $\tau = 10^{-1}$ s is the difference between the average of the first half

4. Experimental setup

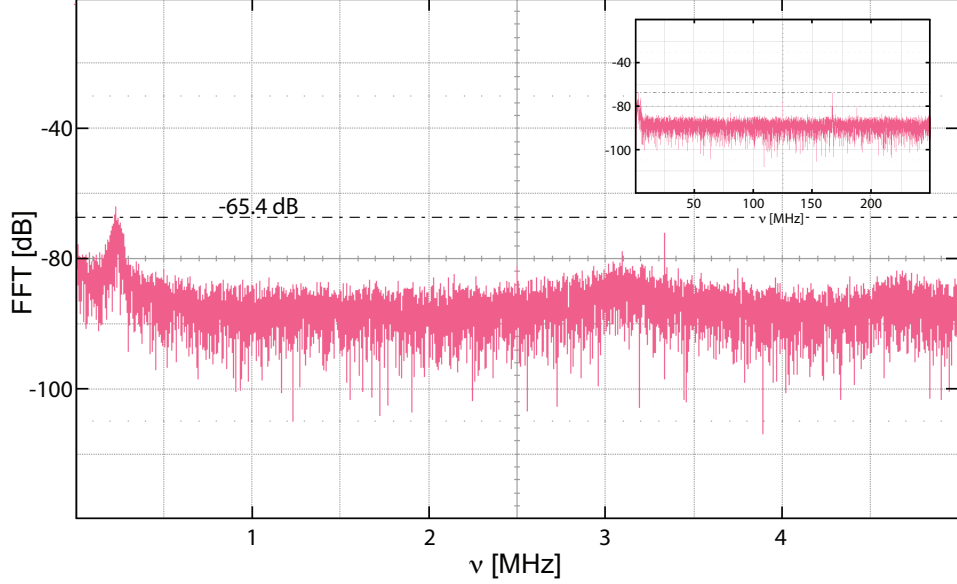


Figure 4.27.: Fast Fourier Transform (FFT) of the Rb error signal for a bandwidth of 5 MHz. The inset shows the FFT for a bandwidth of 250 MHz.

of the data set and the average of the second half of the data set. This is also the case for all averaging times with $\tau = n \cdot \tau_0$ and $n > N/3$, because there are not enough data points to calculate three new values that are averaged over $N/3$ points. The insufficient statistics leads to the observed fluctuations of the Allan variance at this time scale. As a consequence one can not trust this part of the curve. However it is noted that the order of magnitude of the upper limit of the Allan variance is consistent with the long term measurement. The same considerations apply for the values calculated from the long term measurement. For $\tau > 2 \cdot 10^3$ the discreteness of σ_y^2 is clearly visible.

As required in the definition of the Allan variance (3.2), for the long-term measurement each data point was averaged by the oscilloscope over 1 s, with no dead time in between subsequent measurements. This requirement assures that there are no fast oscillations that might be disregarded by the measurement apparatus. The three short-term measurements were only sampled, i.e. each data point was recorded after the sampling period $\Delta\tau$ specified in figure 4.26. To make sure that there is no high frequency noise present, an additional Fast Fourier Transform (FFT) of the Rb error signal was recorded with the oscilloscope. Figure 4.27 shows the FFT for a bandwidth of 5 MHz. All noise with higher frequency than that is filtered by the bandpass filter (figure 4.23). The most prominent peak at 250 kHz with an amplitude of -65.4 dB is still accounted for with the sampling rates of $2 \mu\text{s}$ and $4 \mu\text{s}$. There is no significant high frequency noise present. The inset of the figure shows that the FFT for a bandwidth of 250 MHz. Also for frequencies until the bandwidth of the photodiode (125 MHz) no significant noise is found. Therefore sampling without

averaging on the time scale of the short-term measurements is permitted.

According to the measured Allan variance, the stability of our laser oscillator on the time scale of $\tau = 1 - 10$ s is comparable with the stability of commercial atomic frequency standards³². If we compare it to similar laser stabilization schemes, as for example the closed cavity scheme in [109], we find that the short term stability of our system is reduced but the long term stability is enhanced. With respect to [109] and on time scales of $\tau = 10^{-5}$ to $\tau = 10^{-2}$ our Allan variance is two orders of magnitude bigger. This is reasonable if we take into account that the cavities in [109] have a higher Finesse ($\propto 700$) and sit on a ultra low expansion spacer inside a pressure-sealed container. This yields a much better short-term stability than our aluminium cavities. On longer time scales, however, our Allan variance is more than one order of magnitude lower than the one in [109]. In particular it scales only with τ^1 and not with τ^2 as in [109]. This means that there is no linear frequency drift present, as a result of the referencing to the Cs line.

Relation to earlier results

To my knowledge a measurement of the Allan variance of a transfer-cavity laser stabilization with respect to an absolute reference involving the Pound-Drever-Hall technique has not been published before. A characterization of a transfer cavity stabilization scheme for lasers suitable for ion spectroscopy at $^{40}\text{Ca}^+$ is described in [110]. There the stability of a HeNe reference laser is transferred with a scanning transfer scheme and leads to an Allan deviation of $\sigma_y = 10^{-10}$ at an averaging time of $\tau = 10^3$ s. Figure 4.26 reveals that our Allan variance is a factor of 2 lower for this time scale. As the scanning transfer scheme is very slow due to the 1 kHz scanning rate, no data for shorter time scales is available for comparison.

A scheme very similar to ours is used for high-precision frequency measurements of the D₁ line of alkali atoms [111]. A reference laser (ECDL) is locked to the Rb D₂ line by saturation absorption spectroscopy. The 10 kHz linewidth is transferred to a second laser of the same type via an in vacuum ring cavity. This second laser was then used to measure the absolute frequency of the Rb D₁ line using a second saturated absorption spectroscopy, but no characterization of the long term stability is presented.

In [112] the Allan deviation was calculated from the beat-note of two diode lasers locked to two different hyperfine transitions of the Rb D₁ line using a vapor cell and a cavity. In contrast to our transfer scheme, which bridges optical frequencies, the frequency difference of the two lasers lies with 361 MHz in the micro wave regime. The short-term stability for this setup is much lower than ours. For time scales above $\tau = 10^1$ s the stability gets comparable or even one order of magnitude better ($\tau = 10^3$) than our transfer system. Naturally, on long time scales, a simple Pound-Drever-Hall lock is expected to be more stable than a transfer scheme involving several consecutive stabilizations.

³²SRS Rubidium Frequency Standard FS725

4. Experimental setup

The ultimate solution for stable referencing is the use of recently developed frequency combs. In [113] a Titanium sapphire laser is referenced to the Australian national time standard (UTC) by the use of a frequency comb via a H maser and a GPS system. The square root Allan variance shown in [113] is much lower than ours for $\tau = 10^{-1}$ but gets almost comparable for $\tau = 10^1$. On this time scale, with the simple means of our transfer lock, we reach almost the same performance as this ultra high precision spectroscopy setup.

Summarizing the characterization presented in this paragraph, it can be concluded that the goal of creating a low-cost laser frequency stabilization scheme for $^{40}\text{Ca}^+$ spectroscopy with high long-term stability has been reached very satisfactorily. The absolute stability of 123 kHz rms deviation is well below all relevant transition linewidths ($\propto 20$ MHz). The long-term stability is very good, spectra taken at different times over the day do not show any significant shifts. The linewidth of the laser system is comparable with systems used for ultra-high precision spectroscopy [113]. The advantage in comparison with other transfer stabilization schemes lies in the use of open low-cost table top cavities. No vacuum or ultra low expansion material is needed. A combined temperature and piezo length stabilization of the cavity controlled by a micro controller is at the heart of the system. The degree of stability achieved compared to the resources employed is unrivaled.

5. Light-matter interaction

In the following the theoretical tools needed to describe the experiments in this thesis are discussed. A quantum mechanical formalism for a single atom interacting with two laser light fields is introduced. Equations of motion (Bloch equations) for the internal degrees of freedom of the ion are derived. This allows to describe the intensity of the light scattered by the ion and is used to calibrate all experimental parameters via excitation spectra. A general description of light-matter interaction can be found in [114, 115]. Finally the photon counting statistics of the single-ion resonance fluorescence is discussed. The second order correlation function introduced here serves as the basis for the theoretical description of the two-photon interference presented in the following chapter. As a starting point some properties of $^{40}\text{Ca}^+$ are introduced.

5.1. The Ca ion

Neutral Calcium is a soft grey alkaline earth metal and is the fifth most abundant element by mass in the Earth's crust. It has an atomic number of 20 and an atomic mass of 40.078 amu. Out of the six stable isotopes (^{40}Ca , $^{42-44}\text{Ca}$, ^{46}Ca , ^{48}Ca), ^{40}Ca is the most abundant one with 97 % of the naturally occurring Calcium. This is why it is widely used in K-Ca age dating.

The singly charged Ca^+ ion has a hydrogen-like level structure with a configuration

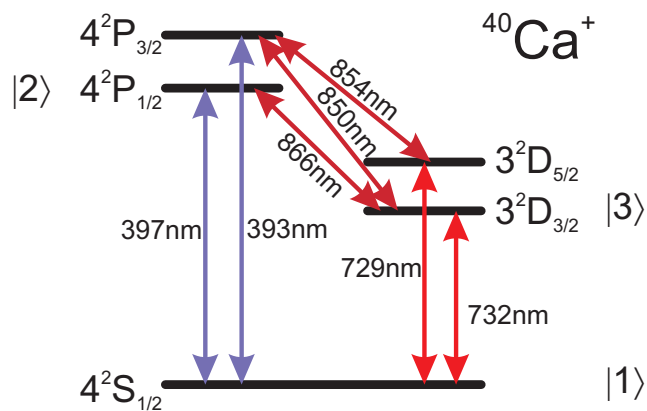


Figure 5.1.: Level scheme of $^{40}\text{Ca}^+$

5. Light-matter interaction

| Transition | λ [nm] | Γ_{nat} [MHz] | τ_{nat} [ns] |
|-----------------------------------|----------------|----------------------|--------------------|
| $S_{1/2} \leftrightarrow P_{1/2}$ | 396.874 | 20.7 | 7.7 |
| $S_{1/2} \leftrightarrow P_{3/2}$ | 393.366 | 21.5 | 7.4 |
| $P_{1/2} \leftrightarrow D_{3/2}$ | 866.214 | 1.7 | 94.3 |
| $P_{3/2} \leftrightarrow D_{3/2}$ | 849.802 | 0.18 | 901 |
| $P_{3/2} \leftrightarrow D_{5/2}$ | 854.209 | 1.6 | 101 |
| $S_{1/2} \leftrightarrow D_{5/2}$ | 729.147 | $152 \cdot 10^{-9}$ | $1.045 \cdot 10^9$ |
| $S_{1/2} \leftrightarrow D_{3/2}$ | 732.389 | $147 \cdot 10^{-9}$ | $1.080 \cdot 10^9$ |

Table 5.1.: Wavelength, natural linewidth and life times of all relevant transitions of $^{40}\text{Ca}^+$.

| $\frac{P_{1/2} \rightarrow S_{1/2}}{P_{1/2} \rightarrow D_{3/2}}$ | $\frac{P_{3/2} \rightarrow S_{1/2}}{P_{3/2} \rightarrow D_{3/2}}$ | $\frac{P_{3/2} \rightarrow S_{1/2}}{P_{3/2} \rightarrow D_{5/2}}$ |
|---|---|---|
| 15.88 | 150.8 | 17.6 |

Table 5.2.: Branching ratios of the P levels [117]

similar to Argon plus an additional valence electron. The level scheme of $^{40}\text{Ca}^+$, which is used in the presented experiments, is shown in figure 5.1. It exhibits no hyperfine splitting since the nuclear magnetic spin is zero. The only isotope with nuclear spin is $^{43}\text{Ca}^+$. It has a much more complex structure but in the context of quantum information it offers the advantage of a hyperfine quantum bit with increased coherence time. This isotope is subject to recent investigations [116].

All wavelengths of the relevant transitions of $^{40}\text{Ca}^+$ can be produced by solid state or diode lasers. The Λ -like level scheme from figure 5.1 has two short lived excited P-states, two meta-stable D-states with a lifetime of about 1s and the $S_{1/2}$ -ground state. The transitions from the $S_{1/2}$ level to the $D_{3/2}$ and $D_{5/2}$ levels are electric quadrupole transitions. All other transitions are electric dipole transitions. Table 5.1 lists the wavelengths and natural linewidths of all transitions and the lifetimes of the respective levels¹. From the linewidths the branching ratios of the P levels are determined (table 5.2). To calculate the Zeeman splitting of a certain level, the Landé factor g_J is needed. Table 5.3 lists the Landé factors of all five levels.

¹A new set of values, based on recent publications, lies within a 5 % error of these values.

| | $S_{1/2}$ | $P_{1/2}$ | $P_{3/2}$ | $D_{3/2}$ | $D_{5/2}$ |
|-------|-----------|-----------|-----------|-----------|-----------|
| g_J | 2 | 2/3 | 4/3 | 4/5 | 6/5 |

Table 5.3.: Landé factors of the five lowest energy levels [118]

5.2. Three level system interacting with two light fields

For simplicity, the dynamics of the three level system is discussed before the formalism is extended to eight levels. The Hamiltonian that describes the interaction of a three level atoms with two coherent light fields can be divided into three different contributions:

$$\hat{\mathcal{H}} = \hat{\mathcal{H}}_{atom} + \hat{\mathcal{H}}_{field} + \hat{\mathcal{H}}_{int} \quad (5.1)$$

The eigenvectors $|a\rangle$ of the atomic Hamiltonian $\hat{\mathcal{H}}_{atom}$, with $a \in \{1,2,3\}$ being the quantum states denoted in figure 5.1, satisfy the equation

$$\hat{\mathcal{H}}_{atom}|a\rangle = \hbar\omega_a|a\rangle. \quad (5.2)$$

$\hat{\mathcal{H}}_{atom}$ can thus be expanded in terms of the eigenvectors

$$\hat{\mathcal{H}}_{atom} = \sum_{a=1}^3 \hbar\omega_a |a\rangle\langle a|. \quad (5.3)$$

The equivalent matrix representation with respect to the basis $a = 1, 2, 3 \rightarrow (1, 0, 0)^T$, $(0, 1, 0)^T$ and $(0, 0, 1)^T$ reads

$$\mathcal{H}_{atom} = \hbar \begin{pmatrix} \omega_1 & 0 & 0 \\ 0 & \omega_2 & 0 \\ 0 & 0 & \omega_3 \end{pmatrix}.$$

If the zero point of energy is chosen to be at level $|2\rangle$:

$$\mathcal{H}_{atom} = \hbar \begin{pmatrix} \omega_1 - \omega_2 & 0 & 0 \\ 0 & 0 & 0 \\ 0 & 0 & \omega_3 - \omega_2 \end{pmatrix}.$$

Due to the large number of photons in the laser fields used in our experiments the effect of the interaction onto the light field can be neglected. The laser fields can therefore be treated as classical monochromatic waves,

$$\vec{E}_b = \Re(E_{b0} e^{-i\omega_b t}) \cdot \vec{\epsilon}_b, \quad \vec{E}_r = \Re(E_{r0} e^{-i\omega_r t}) \cdot \vec{\epsilon}_r. \quad (5.4)$$

The indices $i \in \{b, r\}$ describe the laser fields at 397 nm, coupling level $|1\rangle$ and $|2\rangle$, and 866 nm, coupling level $|2\rangle$ and $|3\rangle$, respectively (see figure 5.1). E_{i0} denotes the amplitude, ω_i the angular frequency and $\vec{\epsilon}_i$ the polarization vector.

Since the transitions coupled by the laser fields in question are both dipole allowed, higher order contributions can be neglected. Under the dipole approximation the light can be assumed to interact only with the electric dipole moment of the atom and not with higher order electric or magnetic moments. The interaction Hamiltonian is thus taken to be

$$\hat{\mathcal{H}}_{int} = -\hat{\vec{D}} \cdot \hat{\vec{E}} \quad (5.5)$$

5. Light-matter interaction

$\hat{\vec{D}}$ represents the atomic dipole vector

$$\hat{\vec{D}} = e \begin{pmatrix} x \\ y \\ z \end{pmatrix},$$

that can also be expressed in terms of the atomic eigenvectors

$$\hat{\vec{D}} = \sum_{a,b=1,2,3} \vec{D}_{ab} |a\rangle\langle b| \quad (5.6)$$

Since the S-D transition is dipole-forbidden, the D level is treated as a stable energy level. In view of the long life time ($1s$) of the D state compared to the typical time scale of the dynamics of the internal degrees of freedom, this approximation is justified. Assuming that the light fields \vec{E}_b and \vec{E}_r only interact with their respective transitions and setting their phases to zero, the interaction Hamiltonian in matrix representation is written as

$$\hat{\mathcal{H}}_{int} = \hbar \begin{pmatrix} 0 & \frac{\Omega_{12}}{2} e^{+i\omega_b t} & 0 \\ \frac{\Omega_{12}}{2} e^{-i\omega_b t} & 0 & \frac{\Omega_{23}}{2} e^{-i\omega_r t} \\ 0 & \frac{\Omega_{23}}{2} e^{+i\omega_r t} & 0 \end{pmatrix},$$

with

$$\hbar\Omega_{12} := \vec{\epsilon}_b \cdot \vec{D}_{12} E_{0b} \quad \hbar\Omega_{23} := \vec{\epsilon}_r \cdot \vec{D}_{23} E_{0r}. \quad (5.7)$$

The Rabi frequencies Ω_{12} and Ω_{23} denote the coupling strength between the atom and the electric field. The complete Hamiltonian finally reads

$$\hat{\mathcal{H}} = \hbar \begin{pmatrix} \omega_1 - \omega_2 & \frac{\Omega_{12}}{2} e^{+i\omega_b t} & 0 \\ \frac{\Omega_{12}}{2} e^{-i\omega_b t} & 0 & \frac{\Omega_{23}}{2} e^{-i\omega_r t} \\ 0 & \frac{\Omega_{23}}{2} e^{+i\omega_r t} & \omega_3 - \omega_2 \end{pmatrix}.$$

Applying the rotating wave approximation, i.e. transforming into a reference frame rotating with the laser frequencies and neglecting "counter-rotating" terms which oscillate at twice the optical frequency, simplifies $\hat{\mathcal{H}}$ further. The unitary transformation into the rotating frame U is written as

$$U = \begin{pmatrix} e^{-i\omega_b t} & 0 & 0 \\ 0 & 1 & 0 \\ 0 & 0 & e^{-i\omega_r t} \end{pmatrix}.$$

With the detunings Δ_b and Δ_r of the laser frequencies to their respective transitions,

$$\Delta_b = \omega_b - (\omega_2 - \omega_1) \quad \Delta_r = \omega_r - (\omega_2 - \omega_3), \quad (5.8)$$

the simplified Hamiltonian for a three level system coupled to two laser fields is

$$\hat{\mathcal{H}}' = \hbar \begin{pmatrix} \Delta_b & \frac{\Omega_{12}}{2} & 0 \\ \frac{\Omega_{12}}{2} & 0 & \frac{\Omega_{23}}{2} \\ 0 & \frac{\Omega_{23}}{2} & \Delta_r \end{pmatrix}.$$

5.3. Master equation

In a realistic model the spontaneous decay from the excited state $|2\rangle$ has to be taken into account. Rather than treating the system as a pure state, the density operator formalism has to be used. The atomic density operator in the basis $|a\rangle$ is

$$\hat{\rho} = \sum_{a,b=1,2,3} \rho_{ab} |a\rangle\langle b|. \quad (5.9)$$

The diagonal elements of the density operator ρ_{ii} with $i \in \{1, 2, 3\}$ are the expectation values for finding the ion in the respective state, while the off-diagonal elements ρ_{ij} with $i \neq j \in \{1, 2, 3\}$ are coherences representing superposition states. The trace of $\hat{\rho}$ is preserved

$$\text{Trace}(\hat{\rho}) = \rho_{11} + \rho_{22} + \rho_{33} = 1. \quad (5.10)$$

For a closed system, i.e. before dissipative processes are taken into account, the time evolution of the density operator is given by the von-Neumann equation

$$\frac{d\hat{\rho}}{dt} = -\frac{i}{\hbar} [\mathcal{H}, \hat{\rho}], \quad (5.11)$$

which is equivalent to the Schrödinger equation for the state vector. When including dissipative processes such as spontaneous emission into the description, the system can no longer be considered closed. To describe the system, that is no longer a pure state but coupled to reservoirs, the master equation in Lindblad form is used.

$$\frac{d\hat{\rho}'}{dt} = \mathcal{L}(\hat{\rho}') = -\frac{i}{\hbar} [\mathcal{H}', \hat{\rho}'] + \mathcal{L}_{damp}(\hat{\rho}) \quad (5.12)$$

It describes a Markovian non-unitary dissipative evolution of the density matrix that is trace preserving. ρ' is the density matrix in the rotating frame and the operator \mathcal{L}_{damp} represents the damping terms which remain unchanged under transformation into the rotating frame.

$$\mathcal{L}_{damp}(\hat{\rho}) = -\frac{1}{2} \sum_m [\hat{C}_m^\dagger \hat{C}_m \hat{\rho} + \hat{\rho} \hat{C}_m^\dagger \hat{C}_m - 2\hat{C}_m \hat{\rho} \hat{C}_m^\dagger] \quad (5.13)$$

The operators \hat{C}_m describe the dissipative processes such as the decay from P to S level

$$\hat{C}_{21} = \sqrt{\Gamma_{21}} |1\rangle\langle 2| \quad (5.14)$$

or the decay from P to D level

$$\hat{C}_{23} = \sqrt{\Gamma_{23}} |3\rangle\langle 2| \quad (5.15)$$

in the three level atom. Since equation 5.12 is a linear differential equation, we will write its formal solution as:

$$\hat{\rho}'(t) = e^{\mathcal{L}t} \hat{\rho}'(0), \quad (5.16)$$

making use of the super operator $e^{\mathcal{L}t}$.

5.4. Bloch equations

After the evaluation of \mathcal{H}' and \mathcal{L}_{damp} , equation 5.12 can be written in a matrix form

$$\frac{d\rho_i}{dt} = \sum_j M_{ij} \rho_j. \quad (5.17)$$

Where M is a $N^2 \times N^2$ matrix, with N being the number of levels and ρ has been transformed into a vector

$$\vec{\rho} := (\rho_{11}, \rho_{12}, \dots, \rho_{23}, \rho_{33}). \quad (5.18)$$

These linear equations are called optical Bloch equations. For the initial condition $\rho(0)$ the solution of 5.17 is given by

$$\vec{\rho}(t) = \exp(Mt) \vec{\rho}(0) \quad (5.19)$$

The normalization condition 5.10 has to be fulfilled for all times. By substituting this condition into one of the Bloch equations and considering only steady state solutions, $\rho(\infty) = const. \rightarrow \dot{\rho} = 0$, the set of equations

$$0 = \sum_j M'_{ij} \vec{\rho}_j. \quad (5.20)$$

can be solved by diagonalizing the matrix M' numerically.

5.5. Excitation spectra

To record excitation spectra, the fluorescence light emitted by the ion is detected while one of the two lasers is scanned over the resonance. The rate of photons scattered by the ion N_{tot} is proportional to the population of the excited state

$$N_{tot} = \Gamma_b \rho_{22} + \Gamma_r \rho_{22}. \quad (5.21)$$

Solving equation 5.20 for the correct experimental parameters predicts therefore the expected excitation spectra. Usually the infrared laser at 866 nm is detuned while the blue photons at 397 nm are recorded. In chapter 6.3 such excitation spectra are fitted with the Bloch equation model to fully calibrate the experiment. Usually it is very hard to precisely predict all parameters, as for example the Rabi frequency that the ion sees can not be measured directly.

The time binning with which the count rate is recorded is on the order of 100 ms to 1 s. This justifies the use of a steady state solution from the previous chapter as the population dynamics happen on a much faster time scale (see table 5.1).

5.5.1. Dark resonances

While sweeping the frequency of the infrared laser over the resonance, eventually the condition for a two-photon coupling of the levels $|1\rangle$ and $|3\rangle$, $\Delta_b = \Delta_r$ will be fulfilled. When this happens, the fluorescence light disappears and the excitation spectrum shows a characteristic dip. This effect is called dark resonance. It can be explained by looking at the stationary solutions of the Bloch equations for this condition.

$$\rho_{dark} = \begin{pmatrix} \frac{\Omega_{23}^2}{\Omega_{12}^2 + \Omega_{23}^2} & 0 & -\frac{\Omega_{12}\Omega_{23}}{\Omega_{12}^2 + \Omega_{23}^2} \\ 0 & 0 & 0 \\ -\frac{\Omega_{12}\Omega_{23}}{\Omega_{12}^2 + \Omega_{23}^2} & 0 & \frac{\Omega_{12}^2}{\Omega_{12}^2 + \Omega_{23}^2} \end{pmatrix}$$

which is a pure state $\rho_{dark} = |\Psi_{dark}\rangle\langle\Psi_{dark}|$ with

$$|\Psi_{dark}\rangle = \frac{1}{\sqrt{\Omega_{12}^2 + \Omega_{23}^2}} (\Omega_{23} |1\rangle - \Omega_{12} |3\rangle) \quad (5.22)$$

$$\hat{\equiv} \frac{1}{\sqrt{\Omega_{12}^2 + \Omega_{23}^2}} \begin{pmatrix} \Omega_{23} \\ 0 \\ -\Omega_{12} \end{pmatrix} \quad (5.23)$$

$|\Psi_{dark}\rangle$ is a coherent superposition state between $|1\rangle$ and $|3\rangle$ and has no contribution from $|2\rangle$. The diagonal elements of the density matrix 5.5.1 show that the population is shared between these states according to the ratio of the Rabi frequencies. The off-diagonal elements denote the coherent oscillations between $|1\rangle$ and $|3\rangle$. Because the population of the excited state ρ_{22} is zero, no light is scattered by the ion.

Considering the time evolution of the dark state

$$\hat{\mathcal{H}}_{int} |\Psi_{dark}\rangle = \hbar \begin{pmatrix} 0 & \frac{\Omega_{12}}{2} & 0 \\ \frac{\Omega_{12}}{2} & 0 & \frac{\Omega_{23}}{2} \\ 0 & \frac{\Omega_{23}}{2} & 0 \end{pmatrix} \begin{pmatrix} \Omega_{23} \\ 0 \\ -\Omega_{12} \end{pmatrix} = 0$$

it becomes clear that ρ_{dark} indeed is a steady state solution. The ion does no longer interact with the light field and is therefore transparent.

5.5.2. Eight-level system

For simplicity, up to now, the discussion has been limited to a three-level system. A realistic model has to take into account the Zeeman splitting of the energy levels that is introduced by the magnetic field defining the quantization axis. The former degenerate states ${}^2S_{1/2}$, ${}^2P_{1/2}$ and ${}^2D_{3/2}$ split into eight new levels (see figure 5.2) according to their magnetic quantum number m_j

$$\Delta E = m_j g_j \mu_B |\vec{B}|, \quad (5.24)$$

with μ_B being the Bohr magneton and g_j the Landé factor (see table 5.3).

The vector form of the Bloch equations from chapter 5.4 can be easily generalized

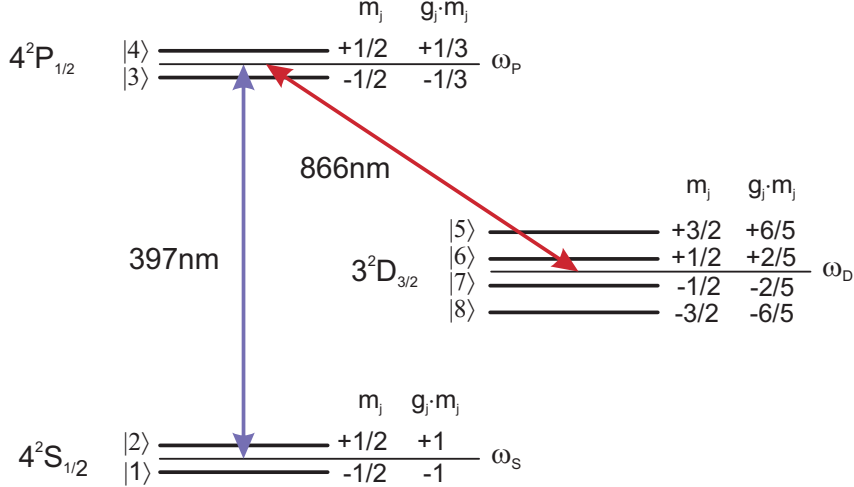


Figure 5.2.: Level scheme of $^{40}\text{Ca}^+$ for a non zero magnetic field \vec{B} . The former degenerated states $^2\text{S}_{1/2}$, $^2\text{P}_{1/2}$ and $^2\text{D}_{3/2}$ split into eight new levels according to their magnetic quantum number m_j and the Landé factors g_j . The splitting shown is not to scale.

to eight levels, with the state vector $\vec{\rho}(t) = (\rho_{11}(t), \rho_{12}(t), \dots, \rho_{78}(t), \rho_{88}(t))$ and M being a 64×64 matrix. One major difference is that due to the selection rules the coupling between the eight levels now depends on the angle α between the polarization of the light and the quantization axis. As a consequence, the excitation spectra also depend on α and on the angle β of the light vector \vec{k} with the quantization axis. A detailed description of the eight-level system can be found in [119].

The maximal number of dark resonances increases to eight, since every sublevel of $S_{1/2}$ can form a coherent superposition with every sublevel of $D_{3/2}$. Their number and positions vary with α and β . For example for excitation with \vec{k} perpendicular to the quantization axis and with $\alpha = 90^\circ$ (σ -polarized light), four dark resonances are expected.

5.5.3. Modeling excitation spectra

The modeling of the excitation spectra is done with a Matlab program described in [119]. It solves the Bloch equations in the steady state limit (equation 5.20) by diagonalizing the matrix M' . M' contains the following parameters:

- The Rabi frequencies Ω_b and Ω_r defined in equation 5.7. They depend on the amplitude of the light field and the dipole matrix elements $\vec{D}_{ab} = \langle a | \vec{D} | b \rangle$, which itself is related to the atomic decay rates Γ_{ab} by

$$\Gamma_{ab} = \frac{8\pi^2}{3\epsilon_0\hbar\lambda_{ab}^3} \left| \langle a | \vec{D} | b \rangle \right|^2 \quad (5.25)$$

The Rabi frequencies can also be expressed in terms of saturation parameters

$$S_b = \frac{\Omega_b}{\Gamma_b}, \quad S_r = \frac{\Omega_r}{\Gamma_r}. \quad (5.26)$$

- The detunings of the lasers from the transitions

$$\Delta_b = \omega_b - (\omega_P - \omega_S) \quad \Delta_r = \omega_r - (\omega_P - \omega_D), \quad (5.27)$$

ω_S , ω_P and ω_D are defined in figure 5.2.

- The magnetic field, expressed through

$$u = \frac{\mu_B |\vec{B}|}{\hbar} \quad (5.28)$$

- The angles α , between the magnetic field and the polarizations of the light², and β , between the magnetic field and the \vec{k} vectors.

- The linewidths of the two lasers

All parameters except the atomic decay rates are external parameters. The ion itself is fully characterized by the level structure, Γ_b and Γ_r .

5.6. Correlation functions

The excitation spectra we discussed so far reveal only information about properties of the system described by stationary solutions of the Bloch equations. The internal dynamics of the atom happens on time scales much shorter than the interrogation times for excitation spectra. The coherence properties of the fluorescence light scattered by an atom contain information about this dynamics, and can be described in terms of correlation functions.

Suppose the emitted light is observed at a fixed position and only one polarization component is filtered out, the first order coherence function is then defined as [114]

$$G^{(1)}(\tau) = \langle E^*(t)E(t + \tau) \rangle, \quad (5.29)$$

and the normalized first order coherence function or degree of first order coherence as

$$g^{(1)}(\tau) = \frac{\langle E^*(t)E(t + \tau) \rangle}{\langle E^*(t)E(t) \rangle}. \quad (5.30)$$

It is a measure of the ability of light to form interference fringes when superimposed at two different points in space and time, here restricted to the case of a fixed point in space and two different times t and $t + \tau$. The second very important property

² α is sufficient for the description of linear polarized light. In the general case of non-linear polarized light a second angle ϕ is necessary.

5. Light-matter interaction

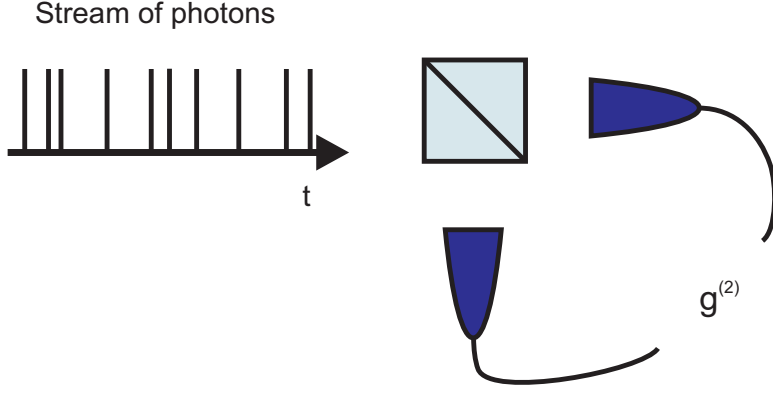


Figure 5.3.: Hanbury-Brown and Twiss setup

of the $g^{(1)}$ -function is that its Fourier-transform reveals the spectral distribution of the light field

$$S(\omega) = \frac{1}{2\pi} \int_{-\infty}^{\infty} g^{(1)}(\tau) e^{i\omega\tau} d\tau. \quad (5.31)$$

The second order correlation function is defined as

$$G^{(2)}(\tau) = \langle E^*(t)E^*(t+\tau)E(t+\tau)E(t) \rangle, \quad (5.32)$$

and the degree of second order coherence as

$$g^{(2)}(\tau) = \frac{\langle E^*(t)E^*(t+\tau)E(t+\tau)E(t) \rangle}{\langle E^*(t)E(t) \rangle^2} = \frac{\langle I(t)I(t+\tau) \rangle}{\langle I(t) \rangle^2}. \quad (5.33)$$

It describes the temporal intensity fluctuations of a light beam, and in a quantum optical context it is usually measured in a Hanbury-Brown and Twiss setup (see figure 5.3): The light beam is sent into one input port of a 50/50 beam splitter and at the two output ports two detectors (usually PMT's or APD's) record the arrival times of the photons. By correlating the arrival times $g^{(2)}$ is evaluated. In general three cases of photon counting statistics are distinguished (figure 5.4).

- $g^{(2)}(0) > 1$: Photon bunching. Due to their bosonic nature photons occur in bunches. The probability of detecting a second photon right after the first one is higher than for longer time differences. Bunching is observed in thermal light that has high intensity fluctuations.
- $g^{(2)}(0) = 1$: Coherent light. It consists of a random stream of photons without any time structure in its correlations.
- $g^{(2)}(0) < 1$: Antibunching. The detection of successive photons is more likely to occur with longer time separation than at shorter time intervals. The most prominent example is the light from a quantum-emitter like a single atom.

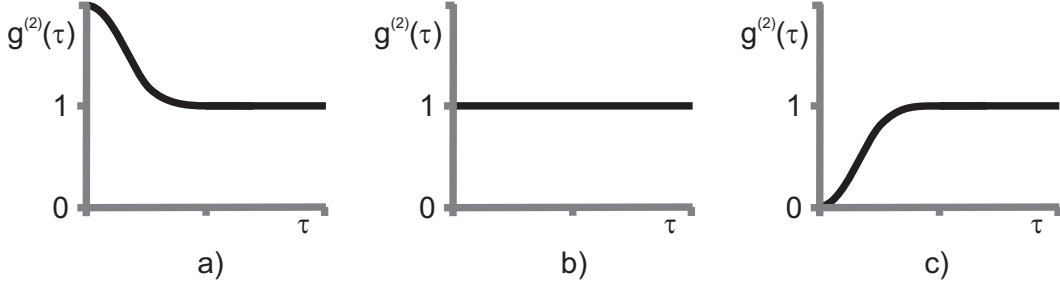


Figure 5.4.: Second order correlation function for: a) Bunching $g^{(2)}(0) > 1$, b) Coherent light $g^{(2)}(0) = 1$ and c) Antibunching $g^{(2)}(0) < 1$

The light scattered by a single ion or neutral atom is ideally antibunched and its second order correlation function vanishes for $\tau = 0$, $g^{(2)}(0) = 0$. After the emission of a photon, the ion first has to be re-excited before it can emit a subsequent photon. This is why the light scattered by a single ion consists of a stream of photons well separated in time. The ion never scatters two photons at a time.

In the following it is shown that the $g^{(2)}$ of a single ion can be interpreted as the probability to find the ion in the excited state after the emission of a photon. Since antibunching can not be explained classically, the coherence properties, i.e. the correlation functions, have to be expressed in terms of quantum mechanical operators

$$g^{(1)}(\tau) = \frac{\langle \hat{E}^-(t)\hat{E}^+(t+\tau) \rangle}{\langle \hat{E}^-(t)\hat{E}^+(t) \rangle} \quad (5.34)$$

and

$$g^{(2)}(\tau) = \frac{\langle \hat{E}^-(t)\hat{E}^-(t+\tau)\hat{E}^+(t+\tau)\hat{E}^+(t) \rangle}{\langle \hat{E}^-(t)\hat{E}^+(t) \rangle^2} \quad (5.35)$$

respectively [114]. $\hat{E}^+(t)$ and $\hat{E}^-(t)$ denote the positive- and negative-frequency part of the electric field operator $\hat{E}(t) = \hat{E}^+(t) + \hat{E}^-(t)$ representing the field radiated by the ion. For a two-level system the field operators can be expressed in terms of the transition operators of the ion:

$$\hat{\sigma} = |1\rangle\langle 2|, \quad \hat{\sigma}^\dagger = |2\rangle\langle 1|. \quad (5.36)$$

The field of an ion sitting in the origin, measured at the point \vec{r} along the quantization axis is then represented by

$$\hat{E}^+(\vec{r}, t) = -\frac{e\omega_0^2 D_{12}}{4\pi\epsilon_0 c^2 |\vec{r}|} \vec{i} \cdot \hat{\sigma} \left(t - \frac{|\vec{r}|}{c} \right), \quad \hat{E}^-(\vec{r}, t) = \hat{E}^{+\dagger}(\vec{r}, t), \quad (5.37)$$

with ω_0 and D_{12} being the frequency and the dipole matrix element 5.6 of the

5. Light-matter interaction

transition, respectively. With 5.37 equation 5.34 and 5.35 can be written as

$$g^{(1)}(\tau) = \frac{\langle \hat{\sigma}^\dagger(t)\hat{\sigma}(t+\tau) \rangle}{\langle \hat{\sigma}^\dagger(t)\hat{\sigma}(t) \rangle} \quad (5.38)$$

$$g^{(2)}(\tau) = \frac{\langle \hat{\sigma}^\dagger(t)\hat{\sigma}^\dagger(t+\tau)\hat{\sigma}(t+\tau)\hat{\sigma}(t) \rangle}{\langle \hat{\sigma}^\dagger(t)\hat{\sigma}(t) \rangle^2}. \quad (5.39)$$

The expectation values of the transition operators in the interaction picture can be calculated to be

$$\langle \hat{\sigma}(t) \rangle = \text{Tr}[\hat{\rho}_I(t)\hat{\sigma}] \exp(-i\omega_0 t) \quad (5.40)$$

$$= \rho_{21}(t) \exp(-i\omega_0 t) \quad (5.41)$$

$$\langle \hat{\sigma}^\dagger(t) \rangle = \rho_{12}(t) \exp(i\omega_0 t) \quad (5.42)$$

$$\langle \hat{\sigma}^\dagger(t)\hat{\sigma}(t) \rangle = \rho_{22}(t) \quad (5.43)$$

Using the quantum regression theorem [120, 121, 122] it can be shown that under the initial conditions $\rho_{22}(0) = 0$, $\rho_{11}(0) = 1$ and $\rho_{21}(0) = \rho_{12}(0) = 0$ and at steady state, the second order correlation function is related to the excited state population by

$$g^{(2)}(\tau) = \frac{\rho_{22}(\tau)}{\rho_{22}(\infty)}. \quad (5.44)$$

For the general case of eight levels a similar expression can be derived. The correlation function of the fluorescence light of $^{40}\text{Ca}^+$ scattered from the excited state $^2\text{P}_{1/2}$ (see figure 5.2) is

$$g^{(2)}(\tau) = \frac{\rho_{33}(\tau) + \rho_{44}(\tau)}{\rho_{33}(\infty) + \rho_{44}(\infty)}. \quad (5.45)$$

Solving the time dependent optical Bloch equations for a given initial state thus predicts the second order correlation function measured from the fluorescence light of a single ion. In turn, the measured second order correlation of the light scattered by a single ion can be interpreted as the excited state population evolving out of the ground state at $t=0$. Equation 5.45 is used to model the data in chapter 7.4 and is modified further in chapter 9.1 to model the polarization dependent second order correlation functions presented in chapter 9.2.

In the next chapter the optical Bloch equations are used to model excitation spectra. The fitted spectra are used to calibrate the experimental parameters in both traps and establish well-controlled conditions.

6. Preparation of the two traps

In this chapter the preparation of the two traps for interference experiments are described. After the trapping procedure for single ions has been performed, the micro-motion has to be compensated. Finally excitation spectra are recorded and fitted with the Bloch equation model in order to calibrate both traps and establish well-controlled conditions.

6.1. Trapping procedure

Before the trapping procedure can start, the radio frequency and the lasers have to be switched on for half an hour. The trap structure and the lasers need this short time period to warm up and run under stable conditions.

As a first step, all laser wavelengths and powers are adjusted. The wavelengths are set with the wavemeter according to table 4.2 using the procedure described in chapter 4.2.9. For trapping, the blue laser is red-detuned by 50 to 100 MHz to assure optimal Doppler cooling. The most convenient way to do so is by jumping one or two modes (the wavemeter has an accuracy of 60 MHz) to higher wavelength with the magic button (see chapter 4.2.6). The infrared laser and the photo-ionization laser (wavemeter reading of the fundamental 845.35015 nm, see chapter 4.1.3) are set to resonance . The photo-ionization laser is not stabilized since the natural linewidth (20 MHz) of the first ionization step is an order of magnitude bigger than the free running linewidth of the laser (2 MHz) and under typical conditions trapping is successful before the laser drifts away.

Once the lasers are locked, the power is distributed between the two traps. Ions can be trapped using two different beam geometries. The first option is to send the blue and infrared beams through the same Photonic Crystal Fiber (PCF) as indicated in figure 4.9. The advantage of this access channel is that the beam waists of the two beams inside the trap are large ($w \approx 100 \mu\text{m}$) and both beams are automatically overlapped. This makes the PCF channel less sensitive to misalignment and provides a big capture range. However, the disadvantage is that the foci of the blue and infrared beams are slightly displaced and that a lot of blue laser power is necessary for efficient trapping. If low blue laser power is available, all the power has to be sent to one trap for trapping. Usually $300 \mu\text{W}$ of blue and red power, measured with the photodiode behind the trap are sufficient. The second beam geometry that can be used for trapping ions is the beam pair along the y' -axis (figure 4.9). Both beams, blue and infrared, are focussed much better ($w \approx 30 \mu\text{m}$) and therefore require less power for trapping. The disadvantage of this channel is that it is easily misaligned due to the small beam waists in the trap center. The laser

6. Preparation of the two traps

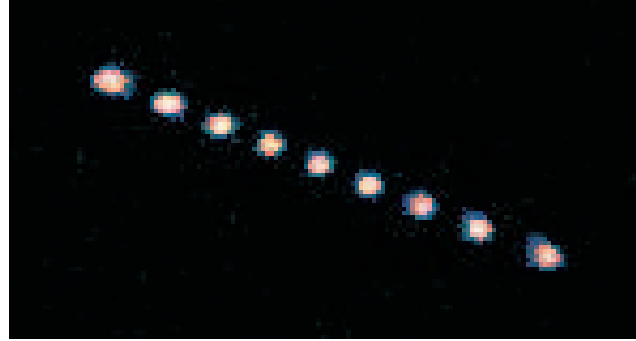


Figure 6.1.: String of 9 ions recorded with the CCD camera for an end tip voltage of 3 V and RF power of 7 W.

powers are read out with a labview program and monitored at all times.

The laser and the LED for photo-ionization are coupled into the same multimode fiber and focussed into the trap with an achromatic lens (for details see [83]) through the bottom viewport. For alignment of the PI beams, the in-coupling side of the multimode fiber is plugged into the input port of one of the PMT's. With an ion trapped, maximizing the count rate on the PMT also optimizes the alignment of the PI beams. If there is no signal, alignment has to be done from scratch: the interference filter in front of the CCD camera is removed (4.9); then, while exciting the atomic beam with the 423 nm laser, the PI beams are aligned to the center of the trap using the 423 nm fluorescence light detected with the camera.

To trap a single ion a current of 4.5 A is sent through the oven. The oven needs some minutes to heat up and generate the sufficient atom flux. A labview program controls the LED, the oven and a shutter that blocks the PI beams. If an ion appears on the camera screen, oven and PI beams are switched off immediately. Leaving the shutter open, the LED switched on and the oven running after an ion is trapped leads to immediate and consecutive loading of more ions. Strings with up to 11 ions can be produced in a quasi-deterministic fashion with this method. Figure 6.1 shows a string of 9 ions imaged onto the CCD camera. For long strings the trap potential has to be very elongated, i.e. low end tip voltage and high RF power.

If the alignment of the exciting lasers is lost and trapping of single ions is not successful, a cloud of ions is loaded in order to realign the lasers. To load an ion cloud, the oven current is set to a high value (max. 6.5 A) and the laser powers are set to maximum. In contrast to the loading of single ions, the pressure in the chamber is rising noticeably during the loading process of an ion cloud.

6.2. Micromotion compensation

Due to electric stray fields caused by surface charges on the electrodes and the entire structure of the trap, the ion is usually shifted away from the minimum of the radio frequency pseudo potential. Another possible cause for this shift are field

6.2. Micromotion compensation

asymmetries caused by imperfections of the trap, e.g. misalignment of the end-caps with the trap axis. This leads to a enhanced motion of the ion at the radio frequency, i.e. micro motion [75, 72]. This has several adverse effects, e.g. alteration of atomic transition line shapes, Doppler shifts, bad cooling or even stark shifts in atomic transitions. Micromotion is compensated by shifting the ion back to the center of the radio frequency potential. This is done by applying the corresponding DC voltages to the compensation electrodes described in chapter 4.1.1. There are several methods to find the right compensation voltages [123].

The method applied in the experiments presented here uses the correlation of the fluorescence light of the ion with the radio frequency. Due to the Doppler effect, the fluorescence light is modulated at the frequency of motion of the ion. The PMT signal that detects the light is now correlated with a TTL signal derived from the RF frequency drive coming from the sine-wave amplifier (see chapter 4.1.5). The correlation of the two signals is done with a commercial counting device¹ by recording a histogram of the photon arrival times with respect to the TTL pulses. The TTL pulses that the PMT generates from the fluorescence photons trigger the start of the time measurement, and a TTL pulse from the radio frequency stops the measurement. The histogram accumulated over a few seconds in this configuration shows a sinusoidal modulation if there is micromotion with a projection onto the direction of the laser beam. The method works best if the laser at 397 nm is tuned to the steepest slope of the resonance curve. At this point, the count rate of fluorescence photons is most sensitive to the change in resonance frequency introduced by the Doppler effect. Since in a linear trap micromotion occurs only in the radial plane of the trap, the procedure has to be carried out using two different laser beams with a projection onto the two radial trap axes for a full compensation of the micromotion.

The compensation electrodes sketched in figure 4.1 are each connected individually and are controlled via the same labview program as the oven and PI beams. In principle micromotion in every radial direction can be compensated by applying the right voltages to the electrodes and thus canceling the modulation in the histogram signal. However it turned out that the configuration of the compensation electrodes is not ideal and that the compensation effect along the y-axis of the trap (see figure 4.1) is shielded by the trap blades. Simulations of the static potentials confirm this assumption [124]. The micromotion in this direction can thus not be fully compensated and the configuration of the electrodes has to be changed on the long run. The residual micromotion has no impact on the experiments presented in this thesis. The motion has no projection on the direction of observation (the x'-axis) and thus the resonance fluorescence observed along this direction is not altered if the ion is excited with a beam perpendicular to the y-axis.

¹PicoHarp 300, PicoQuant

6. Preparation of the two traps

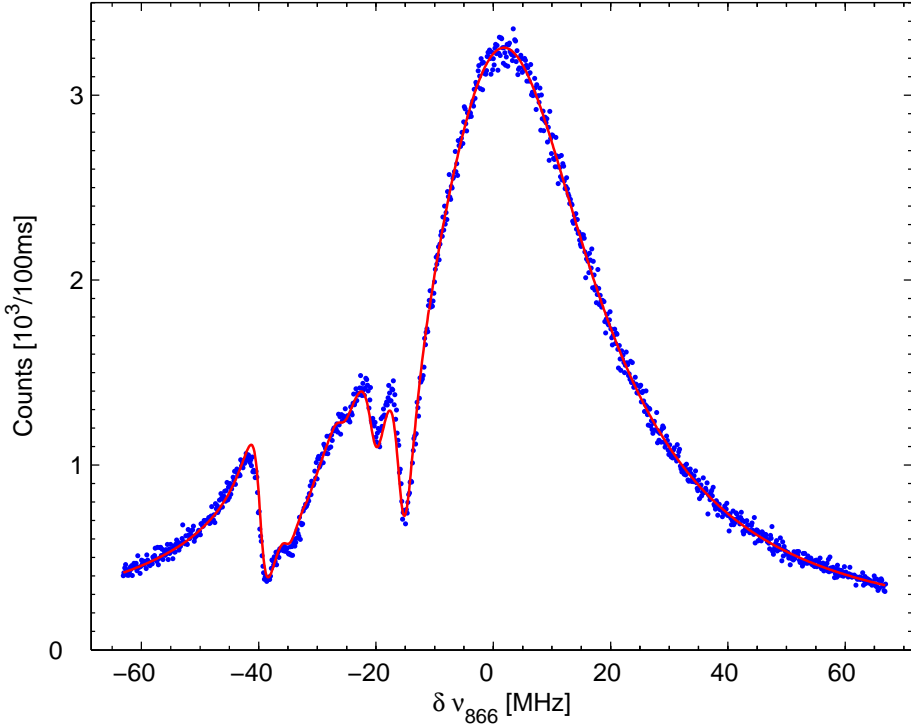


Figure 6.2.: Excitation spectrum of a single ion in the dark trap with excitation under 45° between the x' and y' -axis and detection in the x' -direction. The red line is calculated from the eight-level Bloch equation model. From the fitted line the experimental parameters are calibrated as follows: $\Omega_{SP} = 2\pi \cdot 15$ MHz, $\Omega_{DP} = 2\pi \cdot 3.5$ MHz, $\Delta_{SP}/2\pi = -27$ MHz and $B = 3.8$ G.

6.3. Excitation spectra

Chapter 5.5 describes how excitation spectra are modeled using the optical Bloch equations. In this chapter, this method is applied to one spectrum from the dark and bright trap respectively. In practise, spectra similar to the ones shown are recorded before each measurement to establish well-controlled conditions in both traps. In particular, the indistinguishability of the photons emitted by the two ions is fundamental for all interference experiments and the entanglement protocols based on interference [59, 92, 62, 63, 64]. To achieve this indistinguishability, the Rabi frequencies and the magnetic fields at the sites of the two ions have to be matched.

To record excitation spectra, the fluorescence light of the ion, collected by the HALOs, is detected with a photon-counting PMT while one of the two lasers is scanned over the resonance. Since many more photons are scattered on the blue transition, usually the 397 nm laser is fixed at a detuning providing efficient Doppler

6.3. Excitation spectra

cooling, while the repump laser at 866 nm is scanned over the resonance. For all the plots shown here, each data point represents the count rate integrated over 100 ms.

Figure 6.2 shows the excitation spectrum of a single ion in the dark trap with excitation under 45° to the x' -axis and detection in the x' -direction (along the quantization axis). The polarization of the 397 nm beam is adjusted with a polarizer after the photonic crystal fiber. Both beams are overlapped at this point and therefore the polarization is not controlled independently for the blue and infrared beam. In the case of figure 6.2 the polarizer was adjusted to vertical polarization for the blue beam, exciting only σ -transitions. Using a polarimeter the polarization of the infrared beam was measured to be almost horizontally, exciting σ - as well as π -transitions. The red line is the eight-level Bloch equation model that was fitted to the data with a numeric Matlab-based fitting routine. The agreement with the model is very good, exhibiting a χ^2 of 1.8. To reach such good agreement, also the polarization of the infrared laser was fitted as a free parameter. It turned out to have a slight ellipticity of 3 %. The experimental parameters determined from the fit are given in the caption of figure 6.2. The full linewidth of the lasers extracted from the fit is $\delta\nu_{397}/2\pi = 268$ kHz for the blue laser and $\delta\nu_{866}/2\pi = 1/2 \cdot \delta\nu_{397}/2\pi = 134$ kHz for the infrared laser. This is consistent with the linewidth measured in section 4.2.13.

Figure 6.3 shows the excitation spectrum of a single ion in the bright trap with excitation from the y' -axis and detection in the x' -direction (see figure 4.9). The spectrum was recorded with both the blue and the infrared beam polarized vertically, thus exciting only σ -transitions. The red line is the eight-level Bloch equation calculation, showing good agreement with the measured curve. The four expected dark resonances for this case are well resolved and agree with the model. The experimental parameters calibrated from the fit are given in the caption of figure 6.3. The full linewidth of the lasers extracted from the fit is $\delta\nu_{397}/2\pi = 1400$ kHz for the blue laser and $\delta\nu_{866}/2\pi = 1/2 \cdot \delta\nu_{397}/2\pi = 700$ kHz for the infrared laser.

The fitted linewidths are found to be systematically larger in the bright than in the dark trap. The feature in the recorded excitation spectrum which influences most the fitted linewidth is the width of the dark resonances. Since the fitted laser linewidth accounts for all possible processes that affect the width of the dark resonance, the linewidth determined by the fit is an upper limit for the real width. Since both spectra were taken under equal conditions, the different linewidths indicate an effective additional broadening in the bright trap. This may be caused by inefficient Doppler cooling, if e.g. the k -vector of the 397 nm laser (along the y' -axis) has no or little projection onto one of the radial trap axes. These axes are defined by imperfections in the rotational symmetry (z -axis) of the trap and their alignment is not fully under control. Another reason could be the residual micromotion along the x -axis of the trap. This motion has a projection on the direction of the exciting laser only for the excitation in the bright chamber. The line shape of the dips in figure 6.3 could therefore be explained by Doppler broadening.

By fitting excitation spectra for both traps with the Bloch equation model, the Rabi frequencies, detunings and magnetic fields in both traps are matched. The

6. Preparation of the two traps

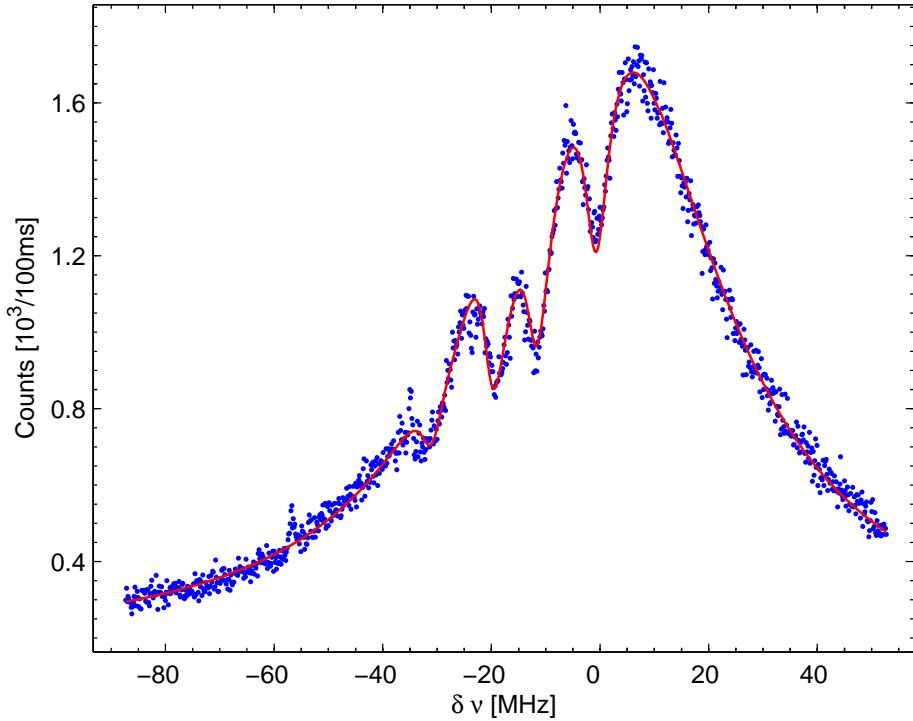


Figure 6.3.: Excitation spectra of a single ion in the bright trap with excitation from the y' -axis and detection in the x' -direction. The red line is a eight level Bloch equation model. From the hand fitted line the experimental parameters can be calibrated as follows: $\Omega_{SP} = 2\pi \cdot 11 \text{ MHz}$, $\Omega_{DP} = 2\pi \cdot 4.9 \text{ MHz}$, $\Delta_{SP}/2\pi = -16 \text{ MHz}$ and $B = 4.9 \text{ G}$.

Rabi frequencies and detunings of the fit in figure 6.2 have an uncertainty of 3 % and the magnetic field of 5 %. For the fit in figure 6.3 uncertainties of 5 % for the Rabi frequencies and detunings, and 9 % of the magnetic field are deduced. These are typical values that are valid also for the spectrum shown in chapter 9. It has to be noted that the parameters of one fit are not independent from each other. With the identical emission properties for both chambers the single ions are prepared for the interference experiments.

7. Two-photon interference

In this chapter the observation of two-photon interference of the fluorescence light from two remotely trapped ions is reported. After a short introduction, the theoretical background of the experiment is discussed. The description of the setup is followed by the final section presenting the experimental results. The experimental data is modeled using the theoretical description from the previous section. The coherence properties of the single photons scattered by each ion are derived from the measurement.

7.1. Introduction

The first and most famous optical interference experiment was performed by Thomas Young in 1801 [125]. In his double-slit experiment, Young showed that the interference pattern observed at a screen behind two illuminated slits results from the superposition of the amplitudes of waves with a certain phase-relation rather than from the addition of intensities. This superposition principle holds true also for the interference of quantized light. The most astonishing phenomenon is the interference of two light fields containing only a single photon. A prerequisite for this interference is that the two photons are indistinguishable in all of their properties, like e.g. wavelength or polarization. Two-photon interference manifests itself particularly clear when the photons are overlapped on a beam splitter. In this configuration the detectors at the two output ports of the beam splitter never detect photons simultaneously because the two photons will always leave the beam splitter through the same output port. This effect is called photon coalescence and was originally shown by Hong, Ou and Mandel [126].

Two-photon interference is the basis of a number of experiments in fundamental quantum physics. As for example, the violation of Bell inequalities [127], the teleportation of a polarization state of a photon [128] or the experimental realization of GHZ states [129, 130]. Especially the proposal by Knill, Laflamme and Milburn for probabilistic quantum computing [131, 132] with single photon sources and only linear optical elements relies on two-photon interference.

Interference of single photons is also essential for future quantum networks where static qubits may constitute the nodes while communication between remote nodes may be achieved through photonic channels transmitting quantum states and entanglement [133]. Figure 7.1 shows an artist's view of a simple network consisting of two quantum processors (two ion strings imaged simultaneously onto the EMCCD camera) and a beam splitter with detectors at the output. Interference of the photons emitted by the ions can establish entanglement between the two processors by

7. Two-photon interference

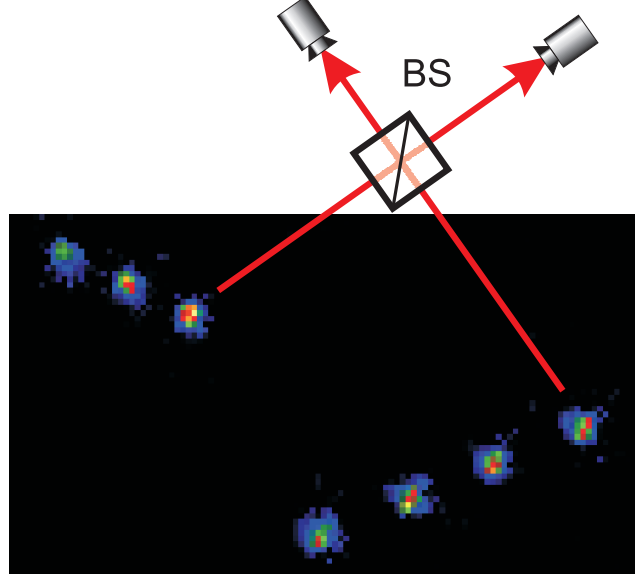


Figure 7.1.: Sketch of quantum network consisting of two quantum processors (two ion strings in different locations, here imaged simultaneously onto the EMCCD camera) and a beam splitter with detectors at the output.

a projective measurement.

Several experiments have recently addressed the realization of atom-photon qubit interfaces that would be suitable for quantum networks. Studies were performed with various systems, including atom-cavity devices [134, 135, 136, 137, 138, 139], atomic ensembles [140, 141, 58, 57], and single trapped atoms or ions [61, 142, 143, 144, 65]. Early experimental progress the observation of single-photon interference between two ions in the same trap under continuous excitation by a laser [145, 85]. A neutral-atom experiment could show interference between photons emitted by two atoms in distinct dipole traps separated by $6\ \mu\text{m}$ under pulsed laser-excitation [142]. Two-photon interference of single-ion fluorescence under continuous excitation was shown [144], as well as two-photon interference between two ions confined in remote traps excited by short laser pulses [143]. The latter experiment has more recently lead to the demonstration of remote entanglement between two independently trapped ions [65, 66]. Furthermore, with the same setup, quantum teleportation between distant matter qubits has been reported for the first time using remotely trapped $^{171}\text{Yb}^+$ ions [67].

For a large number of protocols in quantum information processing the most important resource is entanglement. Remote entanglement in particular is the major challenge in the realization of quantum teleportation, the process to be used to transfer information between nodes in a quantum network.

Entanglement between two remotely trapped atomic systems can be established through single- or two-photon interference. In the first case, two indistinguishable

scattering paths of a single photon interfere such that its detection leads to entanglement of the atoms [59, 60]. In the latter case, coincident detection of two photons, each being entangled with one atom [61], projects the two atoms into an entangled state [62, 63, 64]. Chapter 8 compares these two methods analyzing the role of the detection efficiency. A detailed comparison of this analysis is found in [68].

In this chapter we study the conditions to achieve entanglement between two distant $^{40}\text{Ca}^+$ ions. $^{40}\text{Ca}^+$ is today the only species for which a universal two-qubit gate with an infidelity below or close to the error threshold of models for fault tolerant quantum computation has been achieved [13]. This makes two-photon interference and remote entanglement with $^{40}\text{Ca}^+$ particularly interesting for quantum networking.

In the experiment described in this chapter, we observe and characterize quantum interference between photons emitted by two ions which are independently trapped in the two vacuum chambers, approximately one meter apart. Under continuous laser excitation, resonance fluorescence photons are collected in two input ports of a single-mode optical fiber beam splitter. Due to photon coalescence, both photons leave the beam splitter through the same output mode. Indistinguishability of the input photons is then marked by a vanishing coincidence rate between the two output ports, corresponding to the generation of two-photon states. The contrast of two-photon interference is reduced, however, when the spatial or temporal overlap of the incident photon wave packets is only partial, such that the photons become partially distinguishable [135]. At the output ports, correlations among photon detection events are evaluated. Controlling the polarization at the beam splitter inputs, we observe high-contrast two-photon interference. Recorded correlations allow us to quantify the coherence of the single-ion resonance fluorescence under continuous excitation.

7.2. Theory

In this part the basic theoretical description for the quantification of two-photon interference in the experimental configuration is presented. As depicted in the schematic setup in figure 7.2, we label the two input ports of the beam splitter as I_1 and I_2 . The corresponding fields, \hat{E}_1 and \hat{E}_2 are written in an (\vec{e}_x, \vec{e}_y) polarization basis, \vec{e}_z being the direction of propagation of the fields, where \vec{e}_x , \vec{e}_y and \vec{e}_z denote unit vectors in x , y and z directions, respectively. In the following, fluorescence photons emitted on the $|\text{P}_{1/2}\rangle$ to $|\text{S}_{1/2}\rangle$ electronic transition are expressed in terms of Pauli lowering operators, $\hat{\sigma}_1^-$ and $\hat{\sigma}_2^-$, for ion 1 and 2, respectively (equation 5.36). These are associated with the creation of a single photon. Without any loss of generality, it is assumed that $\hat{\sigma}_1^-$ transforms the field into x polarization, while the polarization of the field corresponding to $\hat{\sigma}_2^-$ is at a variable angle ϕ to the x

7. Two-photon interference

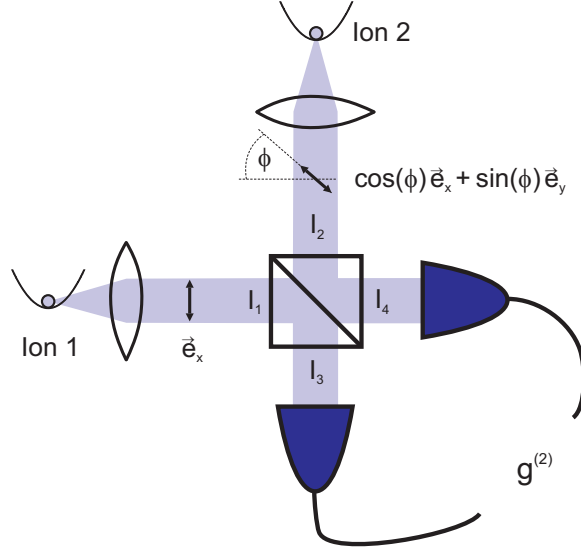


Figure 7.2.: Schematic illustration of the experimental setup. The fluorescence light scattered by each ion is collected with a lens and overlapped on a beam splitter. The light coming from ion 1 is polarized along e_x , while the polarization of the light coming from ion 2 is defined by the angle ϕ . At the output ports I_3 and I_4 of the beam splitter the photons are detected with two detectors and g^2 is calculated.

axis, such that

$$\begin{aligned}\hat{E}_1(t) &= \hat{\sigma}_1^-(t) \vec{e}_x \\ \hat{E}_2(t) &= \hat{\sigma}_2^-(t)(\cos \phi \vec{e}_x + \sin \phi \vec{e}_y).\end{aligned}\quad (7.1)$$

In this expressions the scaling factor of expression 5.37 has been omitted since it plays no role in the following calculations. Also the source-free part of the input fields has been neglected since noise contributions play a minor role in our experiments [146].

For an ideal 50/50 beam-splitter, the transmission and reflection coefficients (t , r) may be chosen as $-i \cdot t = r = \frac{1}{\sqrt{2}}$ [147]. Therefore, field operators at the output arms read

$$\begin{aligned}\hat{E}_3(t) &= \frac{1}{\sqrt{2}} \{ [\hat{\sigma}_1^-(t)e^{i\psi} + i \cos \phi \hat{\sigma}_2^-(t)] \vec{e}_x + [i \sin \phi \hat{\sigma}_2^-(t)] \vec{e}_y \} \\ \hat{E}_4(t) &= \frac{1}{\sqrt{2}} \{ [i \hat{\sigma}_1^-(t)e^{i\psi} + \cos \phi \hat{\sigma}_2^-(t)] \vec{e}_x + [\sin \phi \hat{\sigma}_2^-(t)] \vec{e}_y \},\end{aligned}\quad (7.2)$$

where ψ represents a random phase between the fields emitted by the two ions. Although the experiment has been designed for a future implementation of a path length stabilization between the two ions, the experimental setup used here does not ensure sub-wavelength mechanical stability yet, which imposes the inclusion of ψ .

7.2. Theory

The overall correlation function $G_{\text{tot}}^{(2)}(t, t + \tau)$ can then be expressed as the sum over correlation functions representing all possible polarization permutations

$$G_{\text{tot}}^{(2)}(t, t + \tau) \propto \sum_{(i,j)=\{x,y\}} \langle \hat{E}_{3,i}^\dagger(t) \hat{E}_{4,j}^\dagger(t + \tau) \hat{E}_{4,j}(t + \tau) \hat{E}_{3,i}(t) \rangle \quad (7.3)$$

where $\hat{E}_{(3,4),x}^\dagger$ corresponds to the part of the field $\hat{E}_{(3,4)}$ polarized along x . In the following it is assumed that the emission properties of ions 1 and 2 are identical. After averaging over all possible values of ψ , such that position-dependent non-classical correlations are excluded [148, 149], one finds

$$\begin{aligned} G_{\text{tot}}^{(2)}(t, t + \tau, \phi) &\propto \frac{1}{4} [\langle \hat{\sigma}_1^+(t) \hat{\sigma}_1^+(t + \tau) \hat{\sigma}_1^-(t + \tau) \hat{\sigma}_1^-(t) \rangle \\ &+ \langle \hat{\sigma}_2^+(t) \hat{\sigma}_2^+(t + \tau) \hat{\sigma}_2^-(t + \tau) \hat{\sigma}_2^-(t) \rangle \\ &- 2 \cos^2(\phi) \langle \hat{\sigma}_1^+(t) \hat{\sigma}_1^-(t + \tau) \rangle \cdot \langle \hat{\sigma}_2^+(t + \tau) \hat{\sigma}_2^-(t) \rangle \\ &+ 2 \langle \hat{\sigma}_1^+(t + \tau) \hat{\sigma}_1^-(t + \tau) \rangle \langle \hat{\sigma}_2^+(t) \hat{\sigma}_2^-(t) \rangle]. \end{aligned} \quad (7.4)$$

The first two terms in formula 7.4 represent second order correlations between photons both emitted by the same ion, ion 1 and 2 for the first and second term, respectively. The third term shows the interference between two photons emitted by different ions. It can be rewritten as a product of the individual first-order correlation functions $G^{(1)}$

$$-2 \cos^2(\phi) \langle \hat{\sigma}_1^+(t) \hat{\sigma}_1^-(t + \tau) \rangle \cdot \langle \hat{\sigma}_2^+(t + \tau) \hat{\sigma}_2^-(t) \rangle = -2 \cos^2(\phi) [G_1^{(1)}(t, t + \tau) G_2^{(1)}(t, t + \tau)^*].$$

This term reflects the degree of indistinguishability of photons at the input ports of the beam splitter and consequently vanishes for $\phi = \pi/2$, i.e. for orthogonal polarizations. The fourth term represents the level of random correlations between photons emitted by different ions. This contribution reads as the product of the mean number of photons emitted by each ion, which we denote $\langle n \rangle^2$. Under the assumption of identical emission properties for ions 1 and 2 we can set $G_1^{(2)}(t, t + \tau) = G_2^{(2)}(t, t + \tau) = G^{(2)}(t, t + \tau)$ and $G_1^{(1)}(t, t + \tau) = G_2^{(1)}(t, t + \tau) = G^{(1)}(t, t + \tau)$ and obtain

$$\begin{aligned} G_{\text{tot}}^{(2)}(t, t + \tau, \phi) &= \frac{1}{2} [G^{(2)}(t, t + \tau) - \\ &\cos^2(\phi) |G^{(1)}(t, t + \tau)|^2 + \langle n \rangle^2]. \end{aligned} \quad (7.5)$$

At steady state ($t \rightarrow \infty$), the normalized correlation function is given by $g_{\text{tot}}^{(2)}(\tau, \phi) = G_{\text{tot}}^{(2)}(\tau, \phi) / G_{\text{tot}}^{(2)}(\tau \rightarrow \infty, \phi)$, and it follows

$$g_{\text{tot}}^{(2)}(\tau, \phi) = \frac{1}{2} g^{(2)}(\tau) + \frac{1}{2} [1 - \cos^2(\phi) |g^{(1)}(\tau)|^2]. \quad (7.6)$$

An interesting feature about equation (7.6) is that the two-photon interference contribution (last term) has an amplitude which is given by the individual coherence

7. Two-photon interference

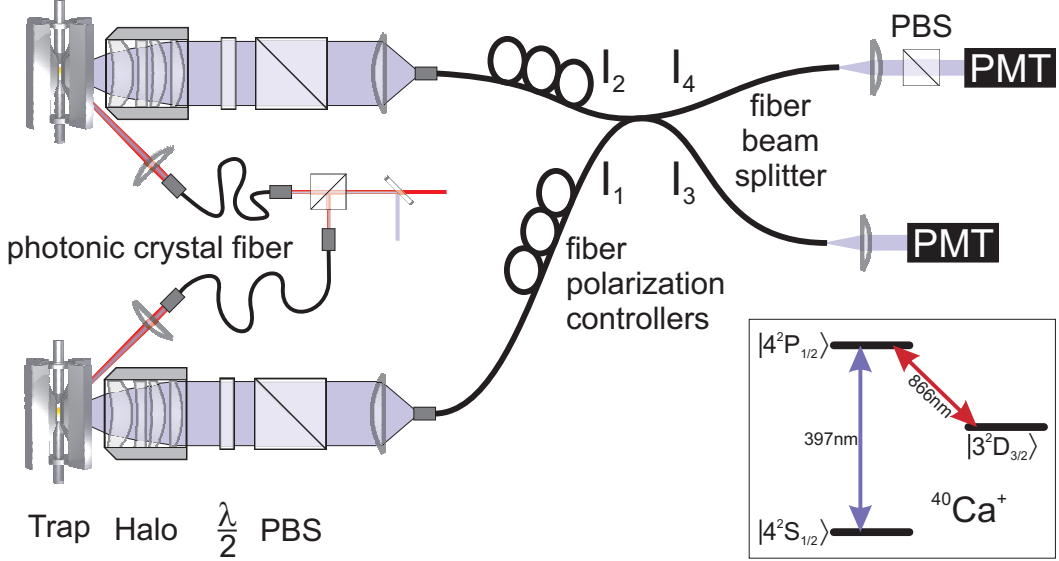


Figure 7.3.: Sketch of the experimental setup. Fluorescence photons are coupled into the two inputs of a single mode fiber beam splitter. Stable polarization is then ensured using fiber polarization controllers (successive loops) and optionally a polarizing beam-splitter (PBS) for control. Second order correlations are computed by recording arrival times at the detectors (PMT) using single-photon counting electronics. The overall time resolution of the detection setup is 1.5 ns. The inset shows the relevant electronic levels of a $^{40}\text{Ca}^+$ ion.

properties of the interfering fields, even for $\phi = 0$, i.e. for identical polarization. Starting from $|g^{(1)}(0)|=1$, the first order coherence function continuously decreases with a time constant equal to the coherence time of the resonance fluorescence. Hence, for ϕ set to 0, the coincidence rate vanishes due to both, the discrete character of photon emission by a single-ion ($g^{(2)}(0)=0$, anti-bunching) and the complete photon coalescence at the beam-splitter. On the other hand, for $\tau \neq 0$, the individual coherence of interfering fields is revealed by the $g_{\text{tot}}^{(2)}$ -function.

7.3. Setup

The schematic of the setup of this experiment and the relevant level scheme for $^{40}\text{Ca}^+$ are shown in Fig. 7.3. The setup consists of two linear Paul traps mounted in the two vacuum vessels separated by about one meter, as described in detail in chapter 4.1. In each of the two traps a single $^{40}\text{Ca}^+$ ion is loaded. The ions are continuously excited and cooled on the $|\text{S}_{1/2}\rangle \rightarrow |\text{P}_{1/2}\rangle$ electronic transition by the laser at 397 nm. The laser at 866 nm resonant with the $|\text{P}_{1/2}\rangle \rightarrow |\text{D}_{3/2}\rangle$ transition prevents optical pumping into the metastable $|\text{D}_{3/2}\rangle$ state. Both lasers are frequency stabilized as described in chapter 4.2.4. Excitation parameters, e.g. laser intensities and frequencies, are set to maximize the count rate of the fluorescence light while

maintaining sufficient laser cooling.

Fluorescence photons from both ions are collected using the previously described HALO lenses (chapter 4.1.2) and then coupled into the two input ports of a single-mode fiber beam splitter. The best strategy to couple the stream of single photons generated by the ions into the fiber is to produce a "fake ion" on the camera screen. More details about this procedure are described in appendix B.

A polarizer before the input coupler projects onto horizontal polarization. A $\lambda/2$ plate placed before the polarizer maximizes the transmission. Thereafter, fiber polarization controllers give full and independent control over the polarizations arriving at the two beam splitter inputs. The polarizing beam splitter (PBS) after one of the fiber outputs (see fig. 7.3) is used to set the polarization either parallel or orthogonal to create indistinguishable or distinguishable photons, respectively. For the indistinguishable photons, both input ports are blocked separately and the count rate after the PBS is maximized in an empirical way with the respective fiber polarization controller. For distinguishable photons, the count rate is maximized for one ion and minimized for the other. Since the light from the two ions propagates through the same output port and hence experiences the same polarization distortion in this port, adjusting to equal (orthogonal) polarization at the output also assures equal (orthogonal) polarization at the beam splitter. The use of a fiber beam splitter instead of a free-space setup ensures optimum spatial overlap of the photon wave-packets at the beam splitter. The contrast of the interference is very sensitive to the spatial overlap and achieving good overlap in a free space configuration is very challenging.

At the outputs of the fiber beam splitter, two photomultipliers¹ with specified $\eta \approx 0.25$ quantum efficiency detect the arriving photons. Their arrival times are recorded with picosecond resolution². The transit time spread of the photomultipliers sets the overall time resolution in this experiment to about 1.5 ns.

7.4. Experimental results

Figure 7.4 presents the second order correlation function, $g_{\text{tot}}^{(2)}$, when photons emitted by the two ions are made fully distinguishable by setting $\phi = 90^\circ$. The coincidence rate is such that $g_{\text{tot}}^{(2)}(0, 90^\circ) \approx 0.5$, as expected from equation (7.5). Indeed, for input photons with orthogonal polarization, the last term in Equation (7.5) reduces to 1/2 independent of τ . This reflects that among all possible correlations, one half occurs between photons emitted by different ions. These are here rendered distinguishable by their orthogonal polarization such that interference is absent and their correlation is random. In Figure 7.4, the result of the theoretical model (Eq. (7.5)) is also presented. It is obtained solving the Bloch equations for our experimental parameters, including eight relevant Zeeman electronic levels for the ion's internal state while neglecting motional degrees of freedom [150]. There is reasonable agreement

¹Hamamatsu, H7360-02SEL

²PicoHarp 300 photon counting electronics

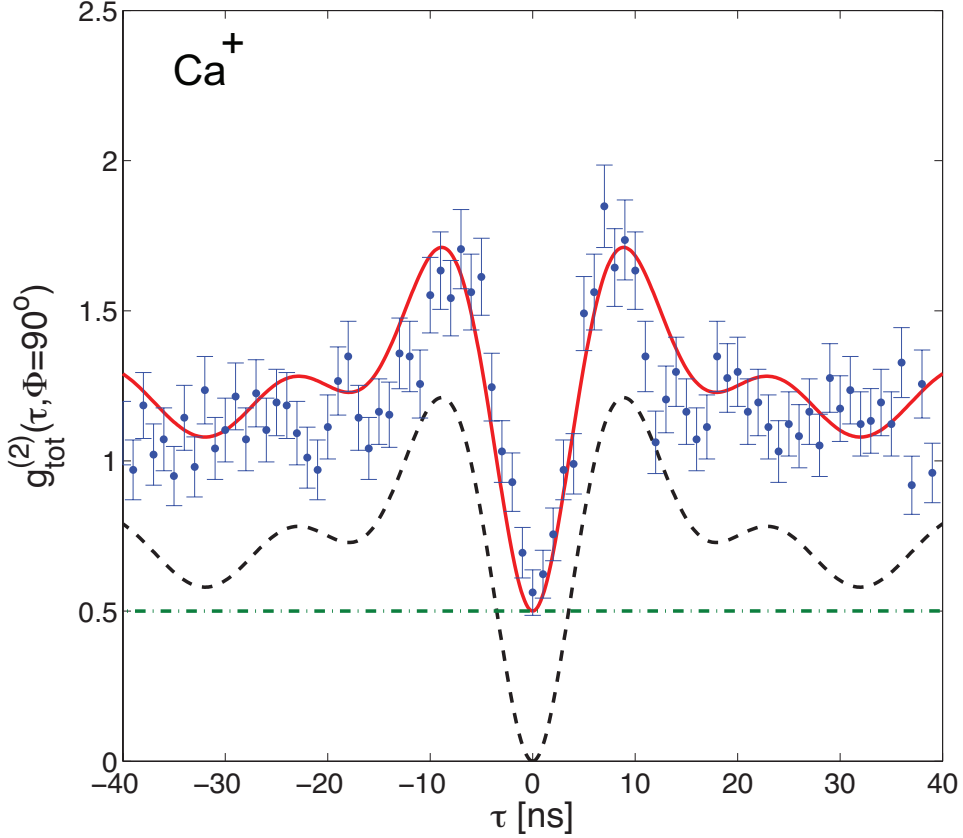


Figure 7.4.: Normalized second order correlation function for orthogonal polarization between I_1 and I_2 ($\phi = 90^\circ$, i.e the non-interfering case). Data are obtained after 2.5 hours of accumulation. Experimental data are presented with 1 ns resolution, without background subtraction, including the variance obtained from shot noise (Poisson statistics at all times τ). The result of the theoretical model (Eq. 7.5) is displayed by the solid line. It is obtained considering our experimental parameters, e.g. laser intensities and detuning, from a full 8-level Bloch equation model. The dashed and dash-dotted lines show the contributions of the first and second term of Eq. (7.5), respectively.

of measurement and model.

Figure 7.5 shows experimental results obtained for $\phi=0$ such that photons impinging at the two input ports of the beam-splitter are indistinguishable. As expected, the normalized number of coincidences strongly drops around $\tau=0$, which signals two-photon interference [144]. From the measured values of $g_{\text{tot}}^{(2)}(0, 90^\circ)$ and $g_{\text{tot}}^{(2)}(0, 0^\circ)$ we deduce that the two-photon interference contrast reaches $80(\pm 10)\%$. The contrast is limited by the time resolution of the photo-detectors³. Each photomultiplier has a electron transit time spread of 1.5 ns. Furthermore, the contrast is

³Hamamatsu H7422P-40SEL

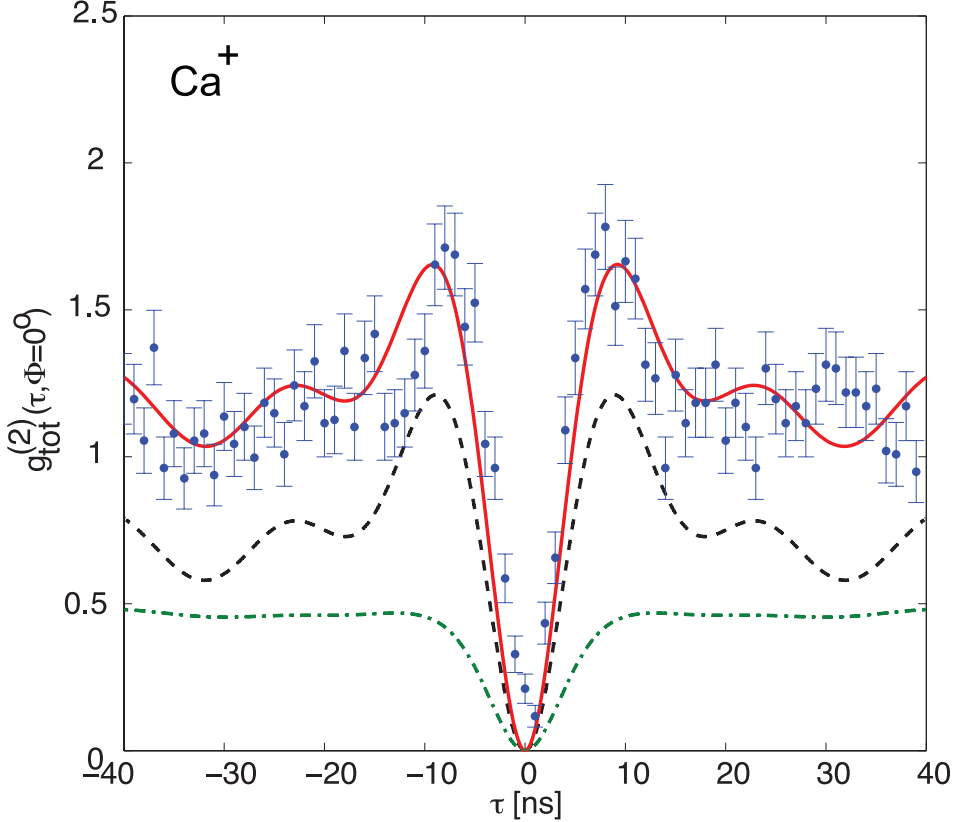


Figure 7.5.: Normalized second order correlation function for indistinguishable photons impinging at the input ports of the beam-splitter ($\phi = 0^\circ$). Experimental data are again presented with 1 ns resolution, without background subtraction, including the variance obtained from shot noise (Poisson statistics). The two-photon interference contrast deduced from these measurements reaches 80(10) %. As in Figure 7.4, the result of our theoretical model (Eq. 7.5) is displayed by the solid line, the dashed and dash-dotted lines showing the contributions of the first and second term of Eq. (7.5), respectively.

derived from raw experimental data, without correcting for accidental correlations induced by stray light photons or dark-counts of the photo-detectors. Subtracting the background correlations, which are calculated from the dark count rates observed during the experiment, an interference contrast of $83(\pm 12)\%$ is derived. If one assumes that the difference of the measured $g_{\text{tot}}^{(2)}(0, 90^\circ)$ after background subtraction from its theoretical value 0.5 is caused by the limited time resolution of the detectors, one can estimate the influence of this limitation on $g_{\text{tot}}^{(2)}(0, 0^\circ)$ by the same value and calculate an interference contrast of $88(\pm 12)\%$. The effect of a time jitter of 3 ns (twice the transit time spread of the detectors) on the theoretical value of

7. Two-photon interference

$g_{\text{tot}}^{(2)}(0, 90^\circ)$ is consistent with this assumption.

As previously mentioned, individual coherence properties of interfering fields modify the overall correlation function for $\phi = 0$. For $\tau = 0$, incident photons are detected simultaneously such that these are fully indistinguishable and therefore the amplitude of two-photon interference is maximal. By contrast, for $\tau \neq 0$ the degree of indistinguishability of the input photons is characterized by the temporal overlap of their wave-packets. The length of these wave-packets in fact corresponds to the photon coherence time which then governs the contrast of the interference [135]. This property is reflected by the last term of Eq. (7.5) which is also represented by a dash-dotted line in Fig. (7.5). It continuously increases before saturating to 1/2 for $|\tau| \approx 10$ ns. This reveals that the coherence time of the resonance fluorescence does not exceed 20 ns in our experiments and indicates that incoherent scattering is dominant, as otherwise much longer coherence times would be observed.

For the general case, i.e. for non orthogonal polarization, the number of coincidence counts is a function of the polarization angle, ϕ . The degree of distinguishability of interfering photons, and thus the amplitude of the two-photon interference, is smoothly tuned with ϕ . From Eq. (7.5) a $\frac{1}{2}[1 - \cos^2 \phi] = \frac{1}{2}\sin^2 \phi$ dependence is deduced.

To my knowledge the precise modeling of two-photon interference from remotely trapped ions, including the derivation of the coherence time of the resonance fluorescence, has not been shown up to now. The observation of two-photon interference presented in this section proves the suitability of the setup for the creation of remote entanglement. One technological step further towards this goal, two-photon interference under pulsed excitation, could also be realized during this thesis and is shown in chapter 10.2. The next chapter analyzes the efficiency of different protocols for remote entanglement depending on the detection efficiency.

8. Methods for remote entanglement

As mentioned in the previous chapter (7) two-photon interference and single-photon interference are two ways to establish distant entanglement. One goal is to study these different methods of remote entanglement with the experimental setup that has been created during the course of this thesis. This is why from the very beginning the setup was constructed to fulfill the requirements for both methods.

In parallel theoretical considerations about the efficiency of entanglement protocols have been conducted. In particular it was analyzed how their performance depends on the photon detection efficiency. The schemes based on measurement of one or two photons were compared in terms of the probability to obtain the detection event and of the conditional fidelity with which the desired entangled state is created.

In this chapter a summary of the quantitative analysis of the protocols for entangling two distant individual atomic systems [59, 92, 62, 63, 64] and how the photon detection efficiency affects their performance is presented. A detailed description of the analysis can be found in [68, 83].

In all the considered proposals, entanglement of the atomic internal states is achieved by interference of photons emitted from distant atoms and subsequent photo-detection projecting the atoms into a Bell state. These protocols are probabilistic in the sense that the expected result is conditioned on the successful detection of a photon.

In order to characterize the schemes two main criteria are applied, the success probability, P_{suc} , and the conditional fidelity, F . The success probability of a protocol measures which fraction of its executions leads to the desired photon detection,

$$P_{\text{suc}} = \frac{\# \text{ detection events}}{\# \text{ scheme executions}} . \quad (8.1)$$

After a successful detection event, the conditional fidelity measures with which probability the density matrix of the system, ρ_M , matches the density matrix of the desired target state, ρ_T ,

$$F = \text{Tr} \{ \rho_T \rho_M \} . \quad (8.2)$$

A more general (although less practical) quantity providing an overall comparison of the schemes is the average fidelity, \bar{F} , which is defined as

$$\bar{F} = P_{\text{suc}} F , \quad (8.3)$$

and which corresponds to the total probability to obtain the desired state in one execution of the entanglement protocol.

8. Methods for remote entanglement

Since all of the considered protocols are conditioned on the detection of photons, the fidelity and the success probability will depend on the efficiency, η , with which these photons are detected, as well as on the probability, p , with which they are emitted. Assuming that all optical elements perform perfect unitary local operation, and that the initial atomic state can be prepared with unit fidelity, the detection efficiency is determined by the finite photon-collection efficiency of the optical apparatus, χ , *i.e.*, the probability that an emitted photon reaches the detector, and by the quantum efficiency of the detector itself, η_d , through

$$\eta = \chi\eta_d . \quad (8.4)$$

8.1. One-photon schemes

A schematic of the one-photon scheme and the Λ -level scheme of the corresponding atoms are shown in 8.1. Initially both atoms are prepared in the ground state $|e\rangle$. The atoms are weakly driven by one laser on the $|e\rangle \rightarrow |r\rangle$ transition. The photons emitted by spontaneous emission into free space on the $|r\rangle \rightarrow |g\rangle$ transition are mixed on a 50:50 beam splitter. A click of a detector D_{\pm} ideally projects the atoms into a Bell state $|\Psi_{\pm}\rangle = \frac{1}{\sqrt{2}}(|e,g\rangle \pm e^{i\phi}|g,e\rangle)$. This scheme is the basis for the proposals [59, 92, 60] and relies on the fact that, due to the mixing at the beam splitter, the setup provides no information on which ion emitted the detected photon.

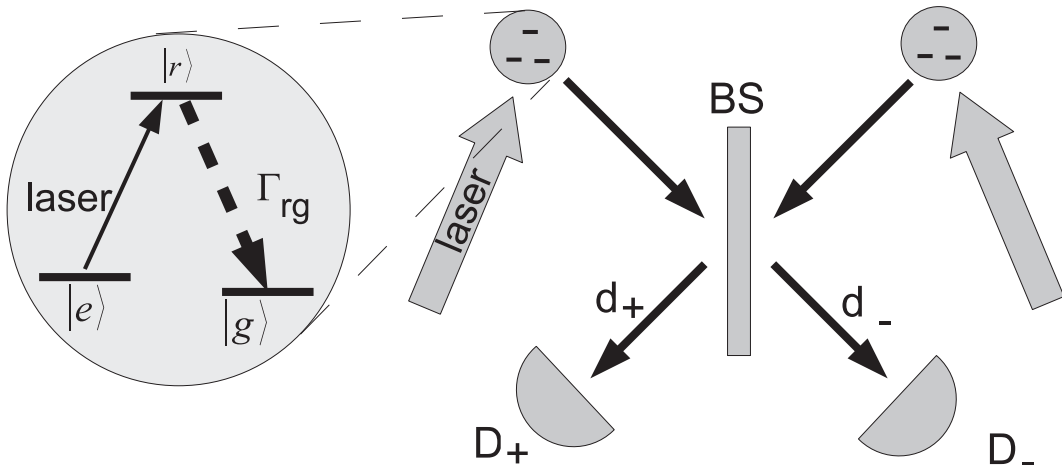


Figure 8.1.: Setups for entangling the internal degrees of freedom of two distant atoms by detection of one photon. The transition $|e\rangle \rightarrow |r\rangle$ in the level scheme shown on the left is driven by a laser, while photons emitted on the $|r\rangle \rightarrow |g\rangle$ transition are mixed on a 50:50 beam splitter (BS). A click of a detector D_{\pm} projects the atoms in a Bell state. The photon is emitted by spontaneous Raman scattering into free space [59].

8.2. Two-photon schemes

A sketch of the two-photon scheme is presented in figure 8.2. In the beginning both atoms are prepared in the excited state $|r\rangle$. Subsequent decay to the ground states $|e\rangle$ and $|g\rangle$ yields photons of orthogonal polarizations. The internal state of the atom is thus entangled with the polarization state of the photon [61]. The photons are overlapped on a beam splitter and a Bell state measurement projects the atoms partially into an entangled state, i.e. coincident clicks at D_{+e} and D_{+g} or D_{-e} and D_{-g} project the atoms into the state $|\Psi^+\rangle$. The state $|\Psi^-\rangle$ is found by coincident clicks at D_{+e} and D_{-g} or D_{+g} and D_{-e} . This scheme is the basis for the proposals [62, 63, 64].

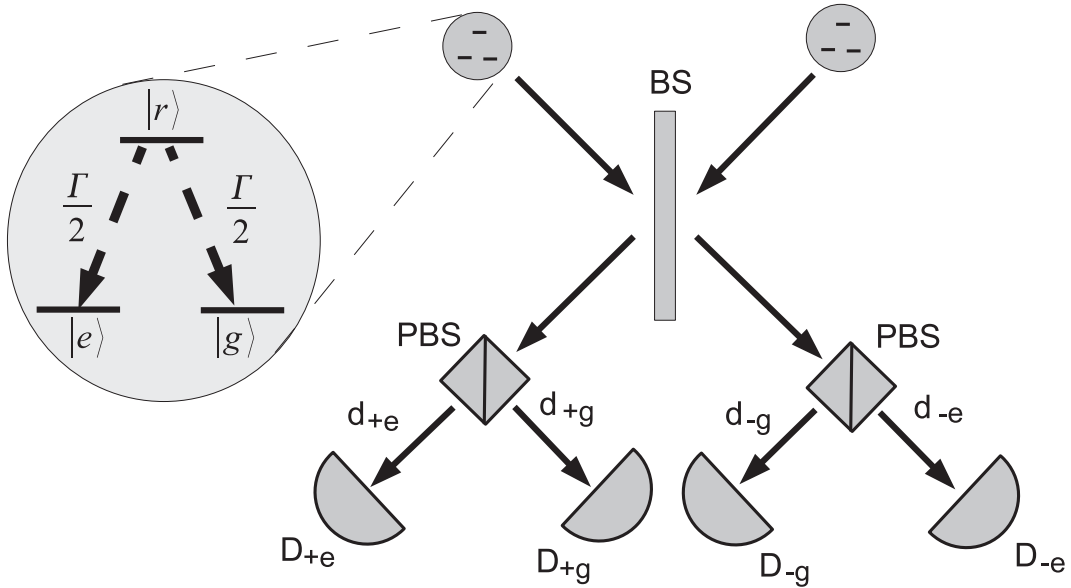


Figure 8.2.: Setup for entangling the internal states of two distant atoms by measurement of two photons [62, 63, 64]. The atoms are prepared in the state $|r_1, r_2\rangle$ and then decay spontaneously. The photon wavepackets overlap at a 50:50 beam splitter (BS). The detection apparatus at the output ports of the BS involves two polarizing beam splitters (PBS) and four detectors.

8.3. Comparison of one- and two-photon schemes

The analysis in [68] shows that the success probability of the two-photon scheme, that relies on the creation and detection of two photons, is

$$P_{2,suc} \propto \eta^2 p^2 \quad (8.5)$$

8. Methods for remote entanglement

yielding a conditional fidelity of $F = 1$, whereas the success probability of the one-photon scheme, that relies on the creation and detection of one photon, is

$$P_{1,suc} \propto \eta p \quad (8.6)$$

yielding a conditional fidelity of $F_1 \approx 1 - (1 - \eta)p$ for $p \ll 1$ or $\eta \ll 1$. Here, p is the probability that one photon is emitted by one atom during the detection time. It becomes clear that for low detection efficiencies η , due to the low probability for two photon coincidences, the success probability for the one-photon scheme is much higher.

If however the emphasis is on high fidelity, in the one-photon scheme this can only be reached for small probability of photon emission, $p \ll 1$. In the two-photon scheme, on the contrary, $F_2 = 1$ independently of the various parameters. In order to explore in a practical manner which scheme has larger success probability for equal fidelity, a threshold value F_{th} is fixed, such that if the measured fidelity $F_1 > F_{\text{th}}$, one can operationally consider the experiment successful.

In the practically relevant regime $\eta \ll 1$, one finds that fidelity values $F \leq 1 - \eta/4$ are reached with higher success probability by the one-photon scheme, while for $F > 1 - \eta/4$, the two-photon scheme shows higher P_{suc} . This limit can be shifted in favor of the one-photon scheme applying a possible purification protocol [151]. A full comparison, *i.e.*, for real experimental settings, also needs to take into account the time per execution which the considered protocols require.

To estimate what fidelities and success probabilities can be realistically achieved in experimental implementations of the proposals discussed, typical parameters of current ion trapping experiments were considered. To estimate a realistic average fidelity, benchmark values for the setup of this thesis are used. An emission probability for a single photon of $p_1 = 0.15$ can be achieved by choosing appropriate values for the detection time and the Rabi frequency. The detection efficiency of the setup is $\eta = \eta_d \chi \approx 0.5\%$, estimated from the detector quantum efficiency, $\eta_d \approx 0.25$, for photons emitted on the $P_{1/2} \rightarrow S_{1/2}$ transition (397 nm), and from the photon collection efficiency $\chi = (\Delta\Omega/4\pi)L \approx 2\%$. The latter is determined by the solid angle within which photons are collected with a high numerical aperture lens ($NA = 0.4$) and the transmission losses in optical elements and fiber coupling, $L \approx 0.5$. For these values of detection efficiency and emission probability one expects to obtain a conditional fidelity $F_1 = 85\%$ at a success probability $P_{\text{suc}:1} = 1.5 \times 10^{-3}$, leading to an average fidelity $\bar{F}_1 = 1.3 \times 10^{-3}$. It seems feasible to run the protocol at a rate of 10^5 experimental sequences per second, which provides sufficient time for state preparation, detection and cooling. Hence, about 150 entangled pairs per second of the above fidelity may be generated. Since the scheme relies on single photon interference for the creation of entanglement, interferometric stability of the setup is required, which is experimentally challenging.

One can even obtain better values when increasing the detection efficiency by placing the atoms in cavities and preparing entangled atom-cavity states by a short initial laser pulse. Using values based on an experimental implementation with a

8.3. Comparison of one- and two-photon schemes

single trapped calcium ion coupled to a high-finesse cavity in Innsbruck, one could hope to improve the average fidelity to $\bar{F}_1 = 5.3 \times 10^{-2}$. The higher detection efficiency due to the increased collection efficiency of fluorescence photons emitted from an atom coupled to a cavity, leads to higher success probabilities at similar values of the conditional fidelities as compared to the free-space scheme considered above. However, the experimental implementation of a single ion coupled to a high-finesse cavity is considerably more demanding than the free-space case.

Creation of entanglement through a two-photon scheme has been experimentally realized in Ref. [65, 66]. Two remotely located trapped $^{171}\text{Yb}^+$ ions were entangled with fidelity $F_2 = 81\%$. Considering the quantum efficiency of the used detectors, transmission through optical elements, fiber coupling, and the solid angle of photon collection, the detection efficiency was $\eta = 6.7 \times 10^{-4}$. At a typical experiment repetition rate of 5.2×10^5 per second, the generation of one entangled atom pair of the above fidelity every 39 seconds was reported, from which a success probability of $P_{\text{suc}:2} = \frac{1}{4}\eta^2 p_2^2 = 4.9 \times 10^{-8}$ is inferred. With a conditional fidelity F_2 of 81%, estimated from the density matrix obtained by state tomography, the average fidelity reads $\bar{F}_2 = 4 \times 10^{-8}$. The measured fidelity was limited by experimental imperfections in the generation of ion-photon entanglement and imperfect interference contrast of the photon modes at the beam splitter. Two-photon interference has the advantage that the requirements on the experimental setup are significantly relaxed as compared to the single-photon schemes, which require interferometric stability. This has certainly contributed to making the two-photon protocol the first one with which distant entanglement of single atoms was demonstrated.

To conclude it can be noted that for low detection efficiency, which is typical for current experiments, and when the fidelity is assumed to be similar in both methods, protocols based on the detection of a single photon exhibit larger success probability.

8. Methods for remote entanglement

9. Conditioned dynamics of photon emission

In this chapter an experiment that studies the conditioned dynamics of the emission of single photons by a single ion is presented. Under some conditions the probability that an continuously laser-irradiated ion emits a photon of a certain polarization depends on the polarization of the photon emitted right before it. In a quantum network where information is interchanged and encoded in the polarization degree of freedom of photons, this might be a useful effect, e.g., to tailor sources of single photons. Here conditioned correlations of such kind are investigated by means of second order correlation functions.

Introduction

One of the most relevant tools for characterizing the light field emitted by a quantum optical system is its intensity correlation function, the most prominent example being the observation of antibunching [152, 153] in the fluorescence of a single atom. Conditioned intensity correlation functions of the fluorescence light of a single ion excited by two light fields have been investigated before [154]. Here, the pair correlation conditioned on the wavelength of the photons scattered by a Ba^+ ion (eight-level structure) were investigated. The correlation function reveals the transient internal dynamics of the ion, which is characterized by optical pumping and the excitation of Raman coherence. In a detailed description of these experiments [150], it is shown that measuring the correlation function for only one polarization of one of the two light fields by adding a polarization filter can leave the ion in a coherent superposition of its energy eigenstates.

Other investigations of the resonance fluorescence of coherently driven single atoms comprise, e.g., a theoretical analysis of the effect of the quantized motion of a two-level atom in a harmonic trap on the second order correlation function [155], experimental measurements of photon correlations revealing single-atom dynamics [156, 157], the theoretical demonstration of nonclassical correlations in the radiation of two atoms [148], i.e. bunched and anti-bunched light is emitted in different spatial directions and the study of intensity-intensity correlations from a three-level atom damped by a broadband squeezed vacuum [158].

A good example of the usefulness of photon-photon correlations in the resonance fluorescence from single atoms is an experiment where, using a self homodyning configuration, the second order correlation function was used to characterize the secular motion of a trapped ion [159]. The experiment revealed the dynamics of both

9. Conditioned dynamics of photon emission

internal and external degrees of freedom of the ion's wave function, from nanosecond to millisecond timescales, in a single measurement run.

Polarization-correlated photon pairs in the fluorescence light from a bichromatically driven four-level atom have been predicted theoretically [160]. In a configuration that is similar to our experiment, photon correlations dependent on the polarization direction of the driving field and the interaction strength are considered. In this proposal a four-level atom ($J = 1/2$ to $J = 1/2$) with degenerate Zeeman sub-states is coupled to a bichromatic field consisting of two components which are symmetrically detuned from the resonance frequency of the atomic transition. In contrast, in the experiment presented in this chapter, the Zeeman degeneracy is lifted and the corresponding atomic transition (four-level system) is driven monochromatically. Furthermore, the effect of the coupling of the excited states to another manifold ($J = 3/2$) of four Zeeman sub-levels by a second light field is taken into account.

In the context of quantum optical information technologies, the entanglement protocols discussed in chapter 8 and the two-photon interference measured in chapter 7 strongly rely on a projective measurement, which is also the origin of the effect of antibunching. In fact, the degree of antibunching is a benchmark for single quantum emitters or ideal single photon sources that are suitable for quantum networking and communication.

Beyond proving that a source is a pure single quantum emitter, correlation functions can be used to characterize and develop useful applications for quantum communication. In [144], for example, part of the resonance fluorescence coming from a continuously excited single ion is delayed and then recombined with the other part on a beam splitter, thus creating an effective two-photon source. Here the measured correlation function reveals how well the two photons are overlapped on the beam splitter. Measuring and controlling the degree of second order correlation of a certain photon source is therefore a very important step in designing quantum optical tools in quantum information processing. This engineering of correlation functions is of special interest for quantum networks where single photons mediate information between nodes of single atoms [53, 52].

Correlation functions also reveal information about the internal degrees of freedom of the emitter (chapter 5.6, equation 5.45) and the properties of the photons. In some protocols for distant entanglement ([63, 62, 64]) the internal degrees of freedom of single atoms need to be entangled with the polarization state of an emitted photon. Although in most of this protocols pulsed excitation is required, it is nevertheless interesting to use correlation functions to study the dynamics of photon emission by a continuously driven single atom dependent on the polarization of the emitted photons. This chapter presents a polarization selective measurement of the correlation function of fluorescence photons from a single ion. In particular, the correlation function of the emitted σ^- and σ^+ polarized photons was measured conditioned on the previous detection of a σ^- photon and it is shown that the system can be designed such that the polarization of a photon depends strongly on the polarization of a previous one.

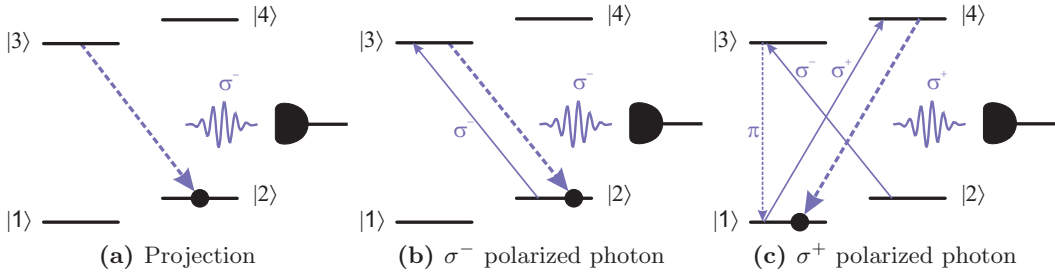


Figure 9.1.: Detection of σ^- (b) and σ^+ (c) polarized photons, conditioned on the previous detection of a σ^- (a) polarized photon. Excitation happens with $\sigma^+ - \sigma^-$ -polarized light, i.e. linear polarization perpendicular to the magnetic field. (a) Detection of a σ^- polarized photon projects the ion into the state $|2\rangle = |S_{1/2}, m_j = 1/2\rangle$. (b) To detect a subsequent σ^- polarized photon, the ion has to be re-excited under the absorption of a σ^- polarized photon. (c) To detect a σ^+ polarized photon, the ion has to be re-excited under the absorption of a σ^- polarized photon, then decay to state $|1\rangle$ under emission of a π polarized photon and then be excited to the state $|4\rangle$ by reabsorbing a σ^+ polarized photon from the exciting beams.

9.1. Model

In chapter 5.6 it was shown that in a stationary process, i.e. under continuous laser excitation, the second order correlation function $g^{(2)}(\tau)$ is proportional to the population of the excited state at time τ . For the realistic 8 level scheme of ${}^{40}\text{Ca}^+$ (figure 5.2), equation 5.45 allows to predict $g^{(2)}$ by solving the optical Bloch equations (5.19). Figure 9.1 shows a sketch of the four levels involved in the emission of blue (397 nm) photons on the $P_{1/2}$ to $S_{1/2}$ transition. The detection of a σ^- polarized photon projects the ion into state $|2\rangle = |S_{1/2}, m_j = 1/2\rangle$ (figure 9.1a). If the ion is continuously illuminated by linearly polarized light at 397 and 866 nm with polarization perpendicular to the magnetic field, no π transitions are excited. The ion effectively sees a superposition of σ^- and σ^+ polarized light. After the emission of a σ^- photon and the corresponding projection into state $|2\rangle$, a subsequent excitation can thus only occur to state $|3\rangle = |P_{1/2}, m_j = -1/2\rangle$ by absorbing a σ^- polarized photon. From state $|3\rangle$ the ion can either decay back to state $|2\rangle$ under emission of a second σ^- polarized photon (figure 9.1b), or it can decay to state $|1\rangle = |S_{1/2}, m_j = -1/2\rangle$ under emission of a π polarized photon. Thus the next emitted photon after a σ^- photon can not be σ^+ polarized. In order to emit a σ^+ polarized photon, the ion must first be excited to state $|4\rangle = |P_{1/2}, m_j = 1/2\rangle$, which can only happen out of state $|1\rangle$ by absorbing a σ^+ polarized photon from the exciting beams (figure 9.1c). The probability of detecting a σ^+ polarized photon after the time τ conditioned on the previous detection of a σ^- polarized photon is therefore much lower than the probability of detecting a σ^- polarized photon for the same condition. Since the correlation function is a measure for the photon-photon waiting time distribution, the $g^{(2)}$ derived from correlating σ^- with σ^+ photons should be suppressed with respect to the $g^{(2)}$ derived from correlating σ^- with σ^- .

9. Conditioned dynamics of photon emission

photons. In fact both correlations are expected to exhibit almost ideal antibunching, with the difference that for the first case the dip around $\tau=0$ is expected to be much wider. In other words, and taking into account also the case where σ^+ and σ^- are exchanged, there will be a much stronger antibunching for the correlation of photons with opposite σ polarization than for photons with the same σ polarization. The same considerations are applicable for excitation with pure π -polarized light. In that case the correlation of subsequent photons is much stronger for opposite than for equal σ polarization.

A short theoretical consideration reveals how the conditioned $g^{(2)}$ can be modeled using the Bloch equations. Following section 5.6, new transition operators for the eight-level system are defined as

$$\hat{\sigma}_1 = |1\rangle\langle 4|, \quad \hat{\sigma}_1^\dagger = |4\rangle\langle 1|, \quad (9.1)$$

$$\hat{\sigma}_2 = |2\rangle\langle 3|, \quad \hat{\sigma}_2^\dagger = |3\rangle\langle 2|, \quad (9.2)$$

and

$$\hat{\pi} = |2\rangle\langle 4| + |1\rangle\langle 3| \quad (9.3)$$

$$\hat{\pi}^\dagger = |4\rangle\langle 2| + |3\rangle\langle 1|. \quad (9.4)$$

If $\hat{\rho}_{ss}$ is the density matrix of the system at steady state, i.e. under continuous excitation, then the detection of a σ^- -polarized photon at time $t=0$ projects into the initial state

$$\hat{\rho}_{\text{init}} = \frac{\hat{\sigma}_2(0) \hat{\rho}_{ss} \hat{\sigma}_2^\dagger(0)}{\text{Tr}[\hat{\sigma}_2(0) \hat{\rho}_{ss} \hat{\sigma}_2^\dagger(0)]} = \frac{\rho_{33}(\infty) |2\rangle\langle 2|}{\rho_{33}(\infty)} = |2\rangle\langle 2|, \quad (9.5)$$

where $\hat{\sigma}_i(t)$ (and analogously $\hat{\sigma}_i^\dagger(t)$) is defined through

$$\langle \hat{\sigma}_i(t) \rangle = \text{Tr}[\hat{\sigma}_i(t) \hat{\rho}(0)] = \text{Tr}[\hat{\sigma}_i \hat{\rho}(t)], \quad (9.6)$$

with $\hat{\rho}(t) = e^{\mathcal{L}t} \hat{\rho}(0)$ (see equation 5.16) and equations 9.1 and 9.2 for $\hat{\sigma}_i$ and $\hat{\sigma}_i^\dagger$. Using equation 5.39, the second order correlation function for the case of the detection of σ^- photons conditioned on the detection of a σ^- photon at time $t=0$ is then written as

$$g_{\sigma^-}^{(2)}(\tau) = \frac{\langle \hat{\sigma}_2^\dagger(0) \hat{\sigma}_2^\dagger(\tau) \hat{\sigma}_2(\tau) \hat{\sigma}_2(0) \rangle}{\langle \hat{\sigma}_2^\dagger(0) \hat{\sigma}_2(0) \rangle^2} \quad (9.7)$$

$$= \frac{\text{Tr}[\hat{\sigma}_2^\dagger(0) \hat{\sigma}_2^\dagger(\tau) \hat{\sigma}_2(\tau) \hat{\sigma}_2(0) \hat{\rho}_{ss}]}{\text{Tr}[\hat{\sigma}_2^\dagger(0) \hat{\sigma}_2(0) \hat{\rho}_{ss}]^2}. \quad (9.8)$$

Permutation inside the traces yields

$$g_{\sigma^-}^{(2)}(\tau) = \frac{\text{Tr}[\hat{\sigma}_2(\tau) \hat{\sigma}_2(0) \hat{\rho}_{ss} \hat{\sigma}_2^\dagger(0) \hat{\sigma}_2^\dagger(\tau)]}{\text{Tr}[\hat{\sigma}_2(0) \hat{\rho}_{ss} \hat{\sigma}_2^\dagger(0)]^2} \quad (9.9)$$

9.1. Model

and with equation 9.5

$$g_{\sigma^-}^{(2)}(\tau) = \frac{\text{Tr}[\hat{\sigma}_2(\tau) \hat{\rho}_{\text{init}} \hat{\sigma}_2^\dagger(\tau)]}{\text{Tr}[\hat{\rho}_{\text{init}}]} \quad (9.10)$$

$$= \frac{\text{Tr}[\hat{\sigma}_2^\dagger(\tau) \hat{\sigma}_2(\tau) \hat{\rho}_{\text{init}}]}{\rho_{33}(\infty)} \quad (9.11)$$

$$= \frac{\text{Tr}[\hat{\sigma}_2^\dagger(0) \hat{\sigma}_2(0) e^{\mathcal{L}\tau} \hat{\rho}_{\text{init}}]}{\rho_{33}(\infty)} \quad (9.12)$$

$$= \frac{\text{Tr}[\hat{\sigma}_2^\dagger \hat{\sigma}_2 \hat{\rho}(\tau)]}{\rho_{33}(\infty)} \quad (9.13)$$

$$= \frac{\rho_{33}(\tau)}{\rho_{33}(\infty)}, \quad (9.14)$$

where $\rho_{33}(\tau)$ is calculated under the condition $\hat{\rho}(0) = \hat{\rho}_{\text{init}} = |2\rangle\langle 2|$. Here, from equation 9.11 to 9.12 the definition of the time dependent creation and annihilation operator (equation 9.6) and the formal solution of the master equation (5.16) were used. In contrast to the general case (equation 5.45) the conditioned second order correlation function is given by only one of the excited state populations at time τ .

The corresponding expression for the case of the detection of σ^+ photons conditioned on the previous detection of a σ^- photon is found by replacing the $\hat{\sigma}_2$ and $\hat{\sigma}_2^\dagger$ operators in 9.13 by the respective transition operators, $\hat{\sigma}_1$ and $\hat{\sigma}_1^\dagger$, for the projection into state $|1\rangle$. The correlation function $g_{\sigma^+}^{(2)}$ for the second case reads thus

$$g_{\sigma^+}^{(2)}(\tau) = \frac{\text{Tr}[\hat{\sigma}_1^\dagger \hat{\sigma}_1 \hat{\rho}(\tau)]}{\rho_{33}(\infty)} = \frac{\rho_{44}(\tau)}{\rho_{33}(\infty)}. \quad (9.15)$$

The expected correlation function can thus be modeled by the solutions of the optical Bloch equations under stationary and time dependent conditions. The difference of the correlation functions for equal and orthogonal polarization arises from the different time dependent solutions of the two emission processes. Due to the intuitive description given above, under excitation with only σ^+ and σ^- light the population of $\rho_{44}(\tau)$ for times τ close to zero will be smaller than the one of $\rho_{33}(\tau)$.

In figure 9.2 and 9.3 the correlation functions calculated according to equations 9.14 and 9.15 are plotted for typical weak and strong excitation parameters, respectively. The upper curves, in blue, show $g_{\sigma^-}^{(2)}(\tau)$, while the lower ones, in red, represent $g_{\sigma^+}^{(2)}(\tau)$. As expected $g_{\sigma^-}^{(2)}(\tau)$ and $g_{\sigma^+}^{(2)}(\tau)$ show very different behaviors. For both weak and strong excitation, $g_{\sigma^-}^{(2)}(\tau)$ rises to high values with a steep slope. For weak excitation a maximum $g^{(2)}$ of 15.6 is reached at $\tau = \pm 29$ ns. For longer time differences the correlation function is falling monotonously until it reaches one. For strong excitation $g_{\sigma^-}^{(2)}(\tau)$ reaches a maximal value of 2.8 at $\tau = \pm 13$ ns. For $\tau > 13$ ns the correlation function is falling to 1 after 200 ns showing some coherent oscillations.

9. Conditioned dynamics of photon emission

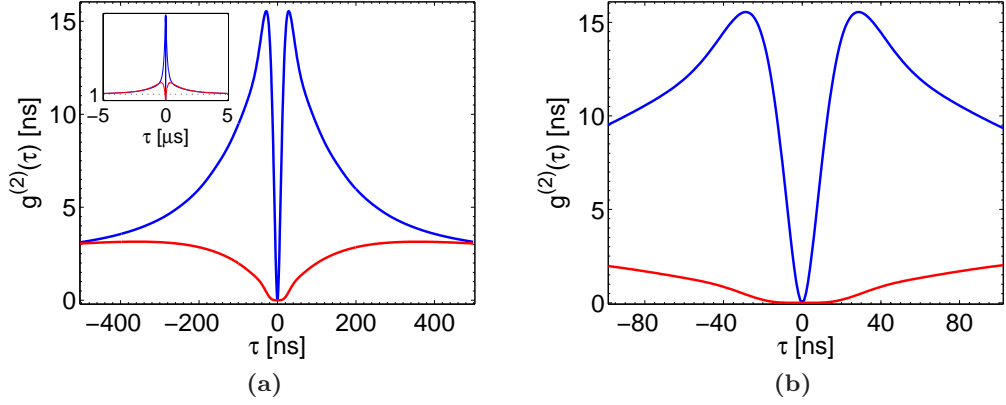


Figure 9.2.: (a) Conditioned second order correlation functions $g_{\sigma_-}^{(2)}(\tau)$ (top, blue) and $g_{\sigma_+}^{(2)}(\tau)$ (bottom, red) for weak excitation. The functions have been calculated with a eight level Bloch equation model for Rabi frequencies of $\Omega_{397} = 2\pi \cdot 9.2$ MHz, $\Omega_{866} = 2\pi \cdot 1.3$ MHz, detunings $\Delta_{397}/2\pi = -15$ MHz, $\Delta_{866}/2\pi = 5.8$ MHz and a magnetic field of $B = 3.5$ G. (b) Zoom into the data set for times -80 ns $> \tau < 80$ ns.

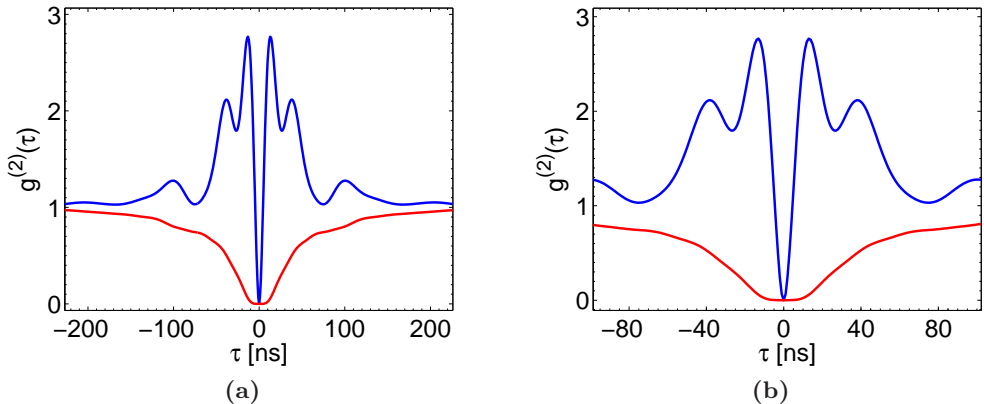


Figure 9.3.: (a) Conditioned second order correlation functions $g_{\sigma_-}^{(2)}(\tau)$ (top, blue) and $g_{\sigma_+}^{(2)}(\tau)$ (bottom, red) for strong excitation. The functions have been calculated with a eight level Bloch equation model for Rabi frequencies of $\Omega_{397} = 2\pi \cdot 20.2$ MHz, $\Omega_{866} = 2\pi \cdot 20.3$ MHz, detunings $\Delta_{397}/2\pi = -15$ MHz, $\Delta_{866}/2\pi = 5.8$ MHz and a magnetic field of $B = 3.5$ G. (b) Zoom into the data set for times -80 ns $> \tau < 80$ ns.

The two $g_{\sigma+}^{(2)}(\tau)$ functions, on the contrary, show a flat behavior on short time scales before they rise with a moderate slope to their maximum value, which is reached at approximately 400 ns for the weak excitation and 200 ns for the strong excitation. In the latter case $g_{\sigma+}^{(2)}(\tau)$ rises directly to 1 without a transient overshoot, while for weak excitation it reaches a value of 3.1 before it falls to 1 for $\tau > 400$ ns.

The shape of $g_{\sigma-}^{(2)}(\tau)$ in figure 9.2a is characterized by large correlation values and a long decay time (compared to the lifetime of the $P_{1/2}$ state) to the asymptotic value and can be attributed to optical pumping into the $D_{3/2}$ state [150]. The excitation on the $S_{1/2} - P_{1/2}$ transitions is much stronger than the one on the $D_{3/2} - P_{1/2}$ transitions. As a result, a large fraction of the population is transferred to the $D_{3/2}$ state after long delay times and the observed fluorescence is weak. This small flux of fluorescence, caused by a small steady-state population of the state $|3\rangle$, determines the normalization factor for long time intervals $\rho_{33}(\infty)$. At short time delays after the projection into state $|2\rangle$, however, i.e. during the first 30-40 ns, a large fraction of the population is excited to state $|3\rangle$ and the optical pumping to the $D_{3/2}$ states is negligible. Since the correlation function is the ratio of the population of state $|3\rangle$ at time τ and in the steady state, high values are reached, which then decay to one revealing the time scale of the optical pumping. The characteristics of $g_{\sigma+}^{(2)}(\tau)$ can be explained with an analogous argumentation. Here, excitation to state $|4\rangle$ during the first 30-40 ns is even smaller than the steady state population $\rho_{33}(\infty)$ for long time delays. After the projection into $|2\rangle$, it takes several scattering events and therefore more time until the population of state $|4\rangle$ exceeds $\rho_{33}(\infty)$. As the inset of figure 9.2a shows, for large time intervals $g_{\sigma+}^{(2)}(\tau)$ decays to the asymptotic value with the same time constant as $g_{\sigma-}^{(2)}(\tau)$.

The correlation functions shown in figure 9.3a are calculated for equal excitation strength on the $S_{1/2} - P_{1/2}$ and $D_{3/2} - P_{1/2}$ transitions. Consequently, the correlation values of $g_{\sigma-}^{(2)}(\tau)$ are smaller and the decay to the asymptotic value is much faster. The exciting fields are strong enough to cause some damped oscillations at the generalized Rabi frequency $\Omega_G = \sqrt{|\Omega_{397}|^2 + \Delta_{397}^2}$ in the correlation function. Due to the complex eight-level structure of the ion, the oscillations do not occur at only one generalized Rabi frequency, but each transition between the Zeeman sub-levels contributes a Fourier component depending on the intensity and detuning of the driving field. In figure 9.3a this becomes noticeable by comparing the frequency of the strongly suppressed oscillations of $g_{\sigma+}^{(2)}(\tau)$ with the ones from $g_{\sigma-}^{(2)}(\tau)$. Due to the Zeeman splitting, the detunings of the $|1\rangle$ to $|4\rangle$ and the $|2\rangle$ to $|3\rangle$ transitions with respect to the exciting laser give rise to different generalized Rabi frequencies.

The zooms in figures 9.2b and 9.3b show the correlation functions in more detail for times τ close to zero. The most interesting feature is that $g_{\sigma+}^{(2)}(\tau)$ shows a flat plateau of values very close to zero for $-15 \text{ ns} > \tau < 15 \text{ ns}$ in the case of weak and for $-10 \text{ ns} > \tau < 10 \text{ ns}$ in the case of strong excitation. The ratio $g_{\sigma-}^{(2)}(\tau)/g_{\sigma+}^{(2)}(\tau)$ of the probabilities to emit a σ^- and a σ^+ photon after having emitted a σ^- photon diverges for $\tau \rightarrow 0$ (at $\tau = 1 \text{ ns}$ it is $> 10^5$) in both excitation regimes. This is because

9. Conditioned dynamics of photon emission

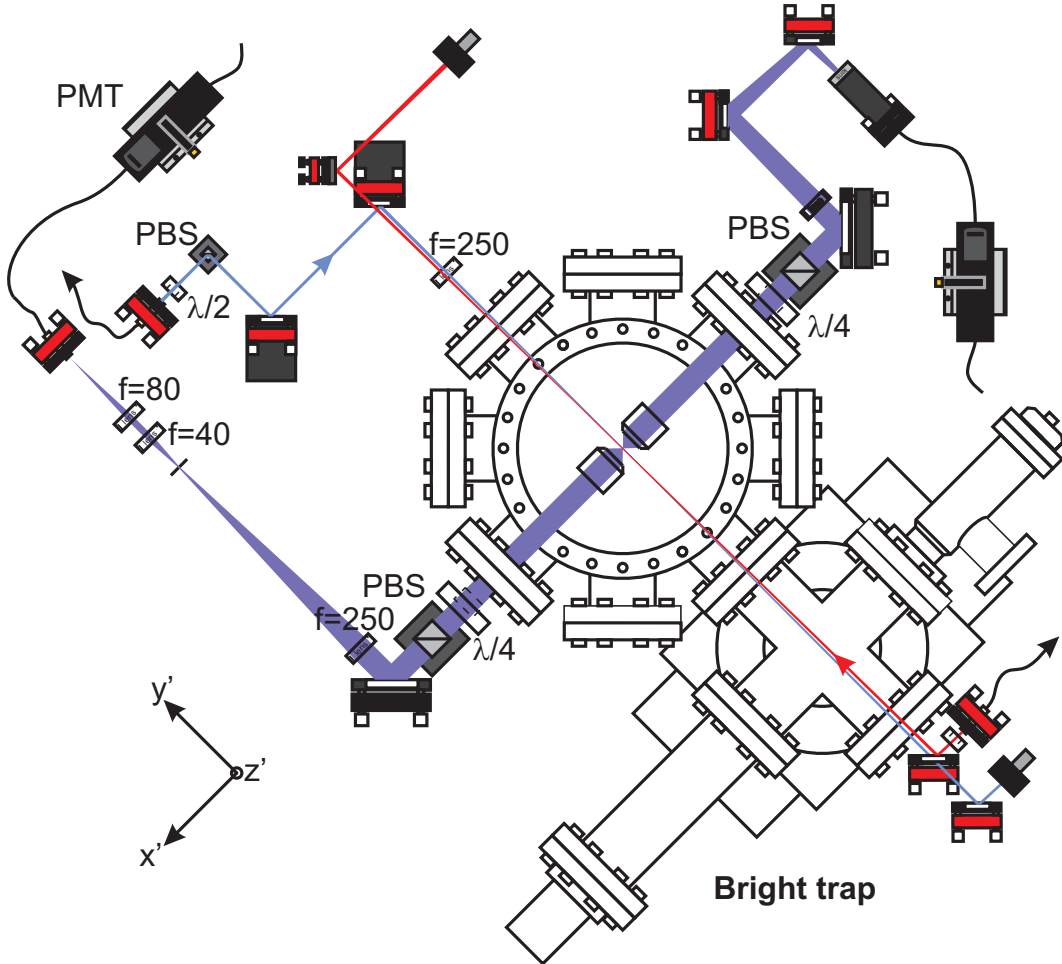


Figure 9.4.: Setup for the measurement of polarization-conditioned correlation functions. The fluorescence light is split in to two parts by collecting it with the two HALO lenses. Multimode fibers are used to couple the light to two PMTs.

$\rho_{33}(\tau)$ increases quadratically in time from $\tau = 0$, while $\rho_{44}(\tau)$ increases with τ^4 . In other words, if a second photon is emitted within a short time interval after a first σ^- -polarized one, then with very high probability (that can be chosen by limiting the time interval) it will also be σ^- -polarized. The correlations of the polarization of subsequent photons emitted by a single ion in the configuration discussed here are thus very strong. By exciting the ion with π -polarized light it is possible to generate equally strongly correlated photon pairs of σ^- - and σ^+ -polarized photons.

9.2. Experiment

Figure 9.4 shows the setup of the measurement that has been conducted with the bright trap. Instead of using a classical Hanbury-Brown and Twiss setup, the fluo-

rescence light is split in to two parts by collecting it with the two HALO lenses. Both lenses collect the fluorescence light at 397 nm and direct it to two photo multipliers (PMT) through multimode fibers. In each beam path a $\lambda/4$ plate and a polarizing beam splitter are used to select the respective polarization. The arrival times of the signals from the PMTs are recorded with picosecond resolution by commercial counting electronics¹. The correlation function is obtained by postprocessing the data. This has the advantage that the time binning of the correlation function can be selected and varied after the measurement.

Calibration

Before measurement of the correlation functions, an excitation spectrum was recorded. The spectrum that shows four dark resonances provides a calibration of the experimental parameters. The experimental parameters extracted from this spectrum are used as the starting point to fit the conditioned correlation functions. In figure 9.5 this excitation spectrum is plotted. The Rabi frequencies, detunings and the magnetic field which are deduced from a fit to the data are indicated in the caption. The number of background counts has also been fitted, with 89 counts per second it is consistent with the background observed during the experiment. Furthermore, to account for experimental deviations in the polarization angle of the excitation lasers from the ideal vertical polarization, this parameter was also varied in the fit. The angles of the polarizations of the two laser beams with the magnetic field, as used in the model shown in figure 9.5, are $\alpha_{397} = 0.46 \cdot \pi$ for the blue laser and $\alpha_{866} = 0.4 \cdot \pi$ for the infrared laser (rather than $\pi/2$ in the ideal case).

Conditioned correlation functions

Figure 9.6 shows the data for the two measured conditioned correlation functions plotted in one graph. Data for $g_{\sigma+}^{(2)}$ are presented in red (bottom) and data for $g_{\sigma-}^{(2)}$ in blue (top). The data are normalized to a long-time value of one and presented without background subtraction. The solid lines are the expected $g^{(2)}$ functions obtained by a fit of the Rabi frequencies to the experimental data using the model discussed in section 9.1. The background extracted from the fit to the excitation spectrum has been included in this model. The parameters have been fitted to both curves at the same time and agree well with the experiment. For large τ (> 400 ns) both functions overlap and slowly decay to one. The correlation functions are very similar to the ones for the case of weak excitation in figure 9.2. The characteristic behavior of large (small) correlation values and the slow decay to the asymptotic value for $g_{\sigma-}^{(2)}$ ($g_{\sigma+}^{(2)}$), explained in section 9.1, are very clearly observed in the measurement.

Figure 9.7 shows a zoom into the region for small time differences. At $\tau = 0$ both curves reach a value close to zero. With increasing τ $g_{\sigma-}^{(2)}$ rises with a very steep

¹Pico Harp 300, Pico Quant

9. Conditioned dynamics of photon emission

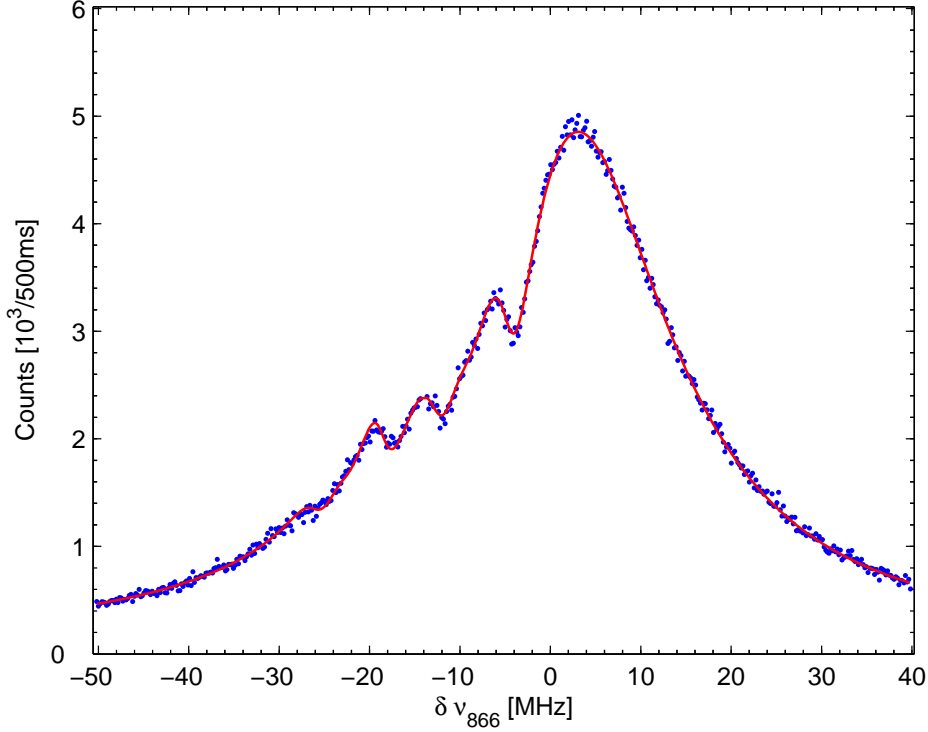


Figure 9.5.: Excitation spectrum of a single ion in the bright trap. The 397 and 866 nm lasers are approximately vertically polarized and propagate under 90° to the quantization axis (see figure 9.4). The solid line (red) is the calculated spectrum for the Rabi frequencies $\Omega_{397} = 2\pi \cdot 9.9$ MHz, $\Omega_{866} = 2\pi \cdot 1.5$ MHz, the detuning $\Delta_{397}/2\pi = -15$ MHz and a magnetic field of $B = 3.5$ G. The data points shown have Poissonian errors.

quadratic slope and reaches a value as large as 12, whereas $g_{\sigma+}^{(2)}$ stays approximately flat for ~ 5 ns, before it rises with a moderate slope to a maximum value of 2.9. The fitted model agrees very well with the data, proving the good control over the conditioned creation of single photons obtained experimentally.

The main difference between the theoretical $g^{(2)}$ in figure 9.2 and experimental data in figure 9.6 is the absence of the predicted τ^4 -like plateau of $g_{\sigma+}^{(2)}(\tau)$ in the measurement. Simulations with the model from section 9.1 show that this is explained by small errors in the polarization of the exciting lasers and in the detection setup. As mentioned before, the polarizations of the exciting lasers have been fitted to the excitation spectrum (fig 9.5), and these results have been used in the model of the correlation functions. To achieve an agreement of the quality as it is shown in figure 9.6 and 9.7, also deviations from the ideal polarizations in the detection were accounted for in the model. These deviations occur when the polarization is not filtered perfectly, and consequently the measured $g^{(2)}$ function contain some coinci-

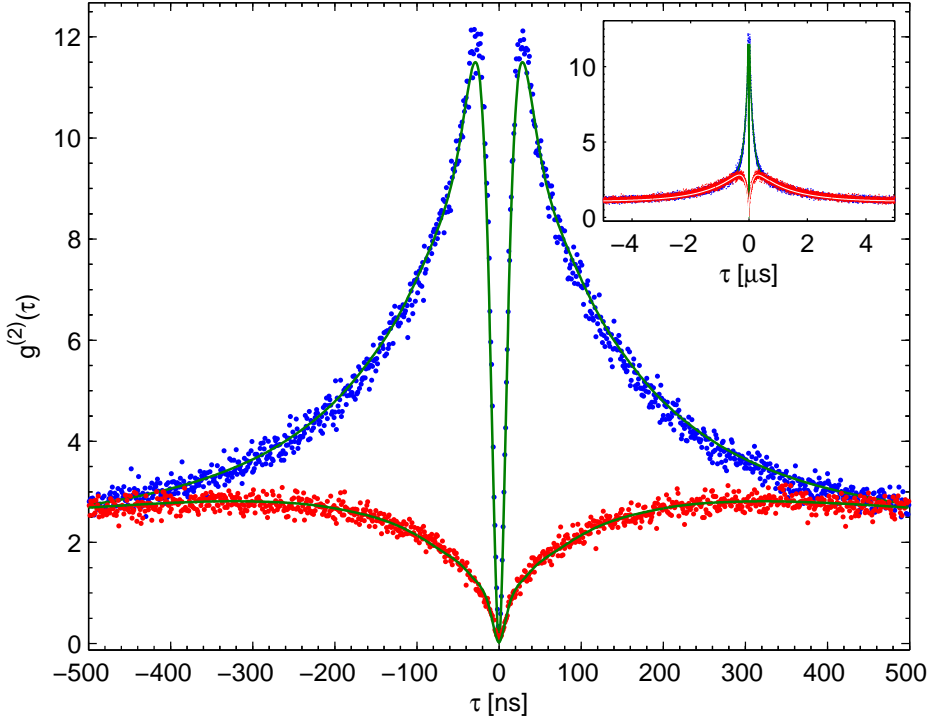


Figure 9.6.: Blue (top): $(g_{\sigma^-}^{(2)})$. Red (bottom): $(g_{\sigma^+}^{(2)})$. The solid lines (green) are the correlation functions expected from the theoretical model for the Rabi frequencies $\Omega_{397} = 2\pi \cdot 9.2$ MHz, $\Omega_{866} = 2\pi \cdot 1.3$ MHz, the detunings $\Delta_{397}/2\pi = -15$ MHz, $\Delta_{866}/2\pi = 5.8$ MHz, and a magnetic field of $B = 3.5$ G. The inset shows data and model for time scales up to $5\ \mu\text{s}$.

dences that are caused by the respective orthogonal polarization. The theoretical model in figures 9.6 and 9.7 has been calculated using 2.5 % of wrong σ^+ polarized photons for the initial detection events in both curves. For $g_{\sigma^-}^{(2)}$ the conditioned detection of the second σ^- polarized photon has an error of 5%, while for $g_{\sigma^+}^{(2)}$ the detection of the σ^+ polarized photon has an error of 1.8%. One sees that $g_{\sigma^+}^{(2)}$, in particular its τ^4 characteristic, is very sensitive to small polarization errors at times τ close to zero. These errors are within the precision with which the polarization filtering was controlled in the experiment, given the low light levels and imperfections of the optics. Another reason for these errors may be a slightly tilted quantization axis caused by stray magnetic fields at the trap center.

The deviation of the Rabi frequencies between the fitted correlation functions and the fitted excitation spectrum lies within the statistical errors of these observables².

²Since the parameters used in fitting the spectrum as well as the $g^{(2)}$ functions are not fully independent from each other, various sets of parameters are consistent with the data, in the

9. Conditioned dynamics of photon emission

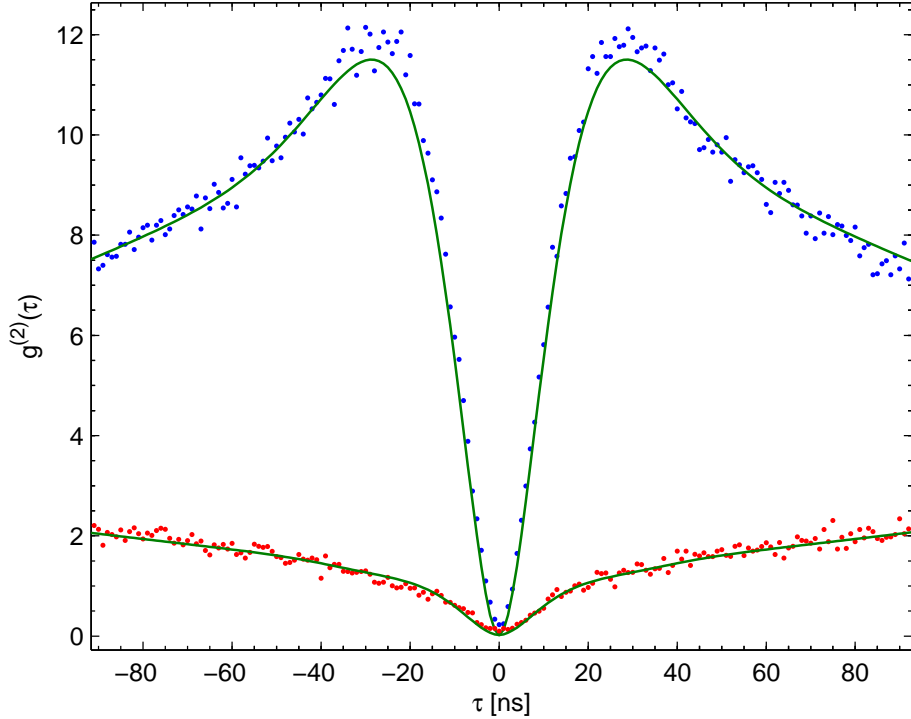


Figure 9.7.: Red (bottom): Normalized second order correlation function for σ^+ light ($g_{\sigma^+}^{(2)}$), conditioned on the previous detection of a σ^- photon. Blue (top): Normalized second order correlation function for σ^- light ($g_{\sigma^-}^{(2)}$), conditioned on the previous detection of a σ^- photon. The solid lines (green) are the expected $g^{(2)}$ functions for the Rabi frequencies $\Omega_{397} = 2\pi \cdot 9.2$ MHz, $\Omega_{866} = 2\pi \cdot 1.3$ MHz, the detunings $\Delta_{397}/2\pi = -15$ MHz, $\Delta_{866}/2\pi = 5.8$ kHz, and a magnetic field of $B = 3.5$ G.

Summarizing, it could be shown that the second order correlation function of the fluorescence light of a single ion can be engineered by polarization-sensitive detection. The $g^{(2)}$ function for σ^+ and σ^- light conditioned on the previous detection of a σ^- photon show a characteristic behavior that might be useful for applications in quantum networks, e.g. for heralding a single photon polarization. Moreover, Bell- or EPR-type correlated photon pairs could be generated as it is proposed in [160].

sense that the whole set of parameters for the spectrum fits the correlations within 1 of the χ^2 deviation and vice versa.

10. Towards networking

The experiments presented until now focus on the tailoring of single photon sources in quantum networks and the creation of remote entanglement by projective measurements. They comprise strong correlations of the polarization of photon pairs emitted by a single ion and interference of the single photons emitted by two distant atoms. In the first case, detecting a single photon of a certain polarization provides information of the internal dynamics of the atom. In the second case the interference of two photons emitted by two atoms gives first evidence for a correlation of the electronic states of the atoms. The common goal of the conducted experiments is to realize basic applications for quantum networking and to study the limits of experimental control over single quantum systems.

In this chapter experiments that indicate the future prospects of the apparatus following the outlined approach towards quantum networking and quantum control are presented. All experiments discussed so far have been done under continuous excitation. After the completion of the pulse sequencer HYDRA and the achievement of its full functionality (chapter 4.2.10), single photons could be generated by pulsed optical pumping. A two-photon interference similar to the one in chapter 7 was measured under pulsed operation and is presented at the end of this section. After the proof-of-principle experiment under continuous excitation, this constitutes an important technological step towards remote entanglement.

In the first part of this chapter an experiment that studies single-photon single-atom interfaces is presented. The absorption of a single photon by a single atom is not only one of the most fundamental processes of our physical environment, it is also an essential ingredient of quantum networks based on atoms as quantum memories and photons as information carriers. Here, we study this process under ideal lab conditions by performing single-photon spectroscopy on a single ion.

The two additional experiments presented in this chapter will not be discussed in full detail, rather a brief overview will be given. Their comprehensive description will be provided in other thesis reports [83, 84] from coworkers who participated in this experiments.

10.1. Single-ion single-photon interaction

As mentioned in the introduction (chapter 1) all fundamental building blocks for quantum information processing have been experimentally realized with trapped ions. The natural further step is to interconnect such quantum processors and to embed or expand this technology into a quantum network [161]. In such a quantum network, based on atoms as nodes that generate, process, and store information,

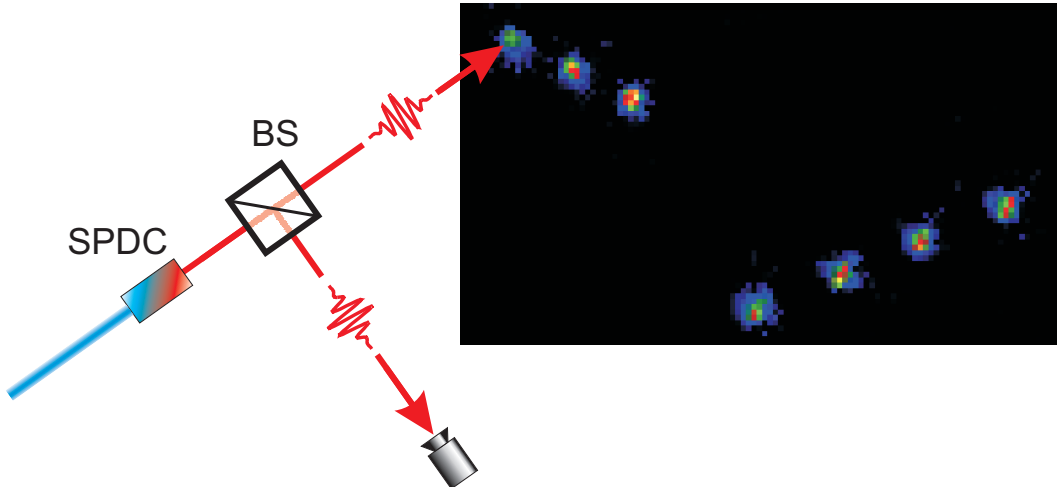


Figure 10.1.: Sketch of the heralded absorption of a down-converted photon by an ion string in one of the two traps.

and photons as long distance information carriers, a fully coherent and efficient state transfer between atoms and photons is required.

The process of the controlled emission of a single photon by a single atom has been subject to extensive research in the recent years. Several groups have developed single photon sources based on trapped atoms. Examples of different realizations are neutral single atoms trapped in strongly focused dipole traps [142], single trapped ions [61, 144] or single trapped atoms and ions in high finesse cavities [162, 163, 139].

However, the reverse process, i.e. the controlled absorption of a single photon by a single atom, could not yet be shown. With the purpose of studying such a controlled absorption, a Spontaneous Parametric Down Conversion (SPDC) source has been build up in parallel to the double ion trap setup [164]. The goal is to realize the heralded absorption of a single down conversion photon by a single ion and ultimately to establish a transfer of the entanglement of these photons onto the ions. A sketch of the heralded absorption is shown in figure 10.1. One of the polarization-entangled photons from the SPDC is detected with a PMT, thereby heralding the possible absorption of the second photon that is focused onto one single ion being part of a string of ions.

In this chapter the first step towards the realization of heralded absorption, i.e. performing single-photon single-ion spectroscopy, is summarized. A detailed description of the performed experiments will be found in [83].

10.1.1. The Down-Conversion source

The source is based on type II collinear spontaneous parametric down-conversion in periodically poled KTiOPO₄ [164]. It is a tunable, frequency-stabilized, narrow-bandwidth source of frequency degenerate, entangled photon pairs. The wavelength can be stabilized to 850 or 854 nm, thus allowing to address the D_{3/2} → P_{3/2} and

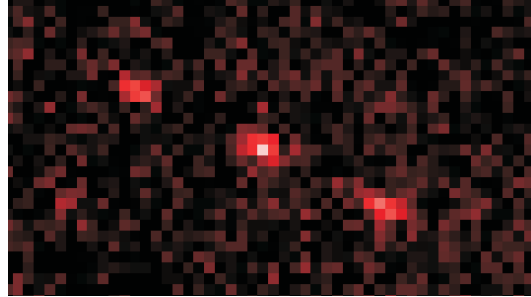


Figure 10.2.: False color image of three-ion-crystal imaged with a HALO collecting 866 nm light. The picture was taken with an integration time of 2 s.

$D_{5/2} \rightarrow P_{3/2}$ transitions in ${}^{40}\text{Ca}^+$. The pump of the KTiOPO₄-crystal is a commercial frequency doubled diode laser¹. The fundamental of the frequency doubling stage is locked to the 852 nm reference laser by a transfer lock similar to the one discussed in chapter 4.2.4. The output bandwidth of 22 MHz coincides with the absorption bandwidth of the mentioned transitions. The spectral output density is 1.0 generated pair/(s MHz mW). The fidelity of the singlet state was measured to be $F = \langle \Psi^- | \rho | \Psi^- \rangle = 97.6 \pm 1.1$ % by polarization state tomography.

The polarization-entangled photons are split by a polarizing beam splitter thus providing pairs of time-correlated photons of fixed, opposite, linear polarization. While one photon is send through a single mode fiber to the ion trap setup, the other one passes through a filter stage consisting of two cavities. These cavities with different bandwidths are locked to the fundamental of the frequency doubling stage and filter out the 22 MHz band from the 143 GHz wide spectrum of the photon pairs. The first photon is send through the incoming channel mentioned in chapter 4.1.6. As sketched in figure 4.9, after the fiber out-coupler the incoming beam is expanded by a telescope and then sent through the dichroic mirror and the HALO onto the ion (the PBS is removed for this experiment).

Alignment

Focussing single photons onto a single ion is a very challenging alignment task. In order to achieve optimal coupling the following procedure has been used. In analogy with the mode matching of the fluorescence light to a single mode fiber from chapter 7.3, a "fake ion" is produced on the CCD camera. 866 nm light is coupled through the incoming channel and imaged (using both HALOs) onto the camera chip using the second imaging path (figure 4.9). Focussing the "fake ion" and overlapping it with the real ion on the camera couples the incoming 866 nm light to the ion. Figure 10.2 shows an image taken with the infrared fluorescence light.

After overlapping the 866 nm fake ion with the real ion, the next step was to send a weak laser beam (derived from the fundamental of the source) at 850 nm

¹Toptica TA-SHG 110

10. Towards networking

through the HALO. When exciting with 397 nm light and repumping with the 850 and 854 nm laser via the $P_{3/2}$ state (without 866 nm light), the ion is bright. The 850 nm beam can thus be aligned maximizing the fluorescence on the camera. This is achieved by moving the HALO to the focal position for 850 nm and iterative alignment of the HALO and in-coupling mirrors in the $y'z'$ -plane.

10.1.2. Quantum jump spectroscopy

Hans Dehmelt suggested in 1975 the concept of quantum amplification [165]. In this scheme, the resonance fluorescence of a strong transition in a single ion is used as a monitor whether or not the ion is in its electronic ground state. If the ground state is coupled in a V-level arrangement to two excited states with vastly different transition rates, this serves as a millionfold amplifier of the very weak transition rate to and from the weakly coupled state. In $^{40}\text{Ca}^+$, for example, one would scatter many photons on the $S_{1/2} \rightarrow P_{1/2}$ transition and apply a very weak excitation to the $D_{5/2}$ state at the same time. If an excitation to the $D_{5/2}$ state takes place, also called shelving, the fluorescence light from the strong transition breaks down immediately and even for a very poor detection efficiency an easily observable signal is produced. The ion stays dark for the lifetime of the excited state until it decays back to the ground state and gets bright again. From the statistics of the dark times the lifetime of the excited state can be measured. In 1986 these quantum jumps were observed for the first time with a Ba^+ ion, which has the same level structure as Ca^+ [25, 24, 26]. The lifetime of the $D_{5/2}$ state of Ba^+ was thereby measured to a degree of precision that was previously not accessible at that time.

This demonstrates that quantum amplification is a very good method to detect very weak signals or rare events. In this chapter it is summarized how quantum jumps are used to detect the absorption of single down-conversion photons by a single trapped ion.

The ion is continuously excited and cooled on the $S_{1/2} \rightarrow P_{1/2}$ electronic transition by the laser at 397 nm. The laser at 866 nm resonant with the $P_{1/2} \rightarrow D_{3/2}$ transition prevents optical pumping into the metastable $D_{3/2}$ state. However, the ion spends significant time in the $D_{3/2}$ state, from where it is eventually excited to the $P_{3/2}$ state by absorbing an 850 nm photon coming from the SPDC source. The $P_{3/2}$ state has three possible decay channels. According to the branching ratios from table 5.2 the atom will decay back to the ground state with a probability of 94 % and with a probability of 0.6 % it will decay back to $D_{3/2}$. In both cases the ion stays bright. In 5.4 % of the cases it will decay to $D_{5/2}$, causing a dark period in the fluorescence of 1 s on average, before it decays to the ground state (figure 10.3a). Figure 10.3b shows the 397 nm count rate exhibiting three quantum jumps.

For a rough estimate of the expected rate of quantum jumps, it is assumed that the absorption cross section for photons from a single mode fiber is equivalent to the coupling efficiency of emitted photons into a single mode fiber (50 %). With the HALOs collecting light from a solid angle of 4 %, the geometrical cross section is estimated to be 2 %. The absorption probability due to the oscillator strength

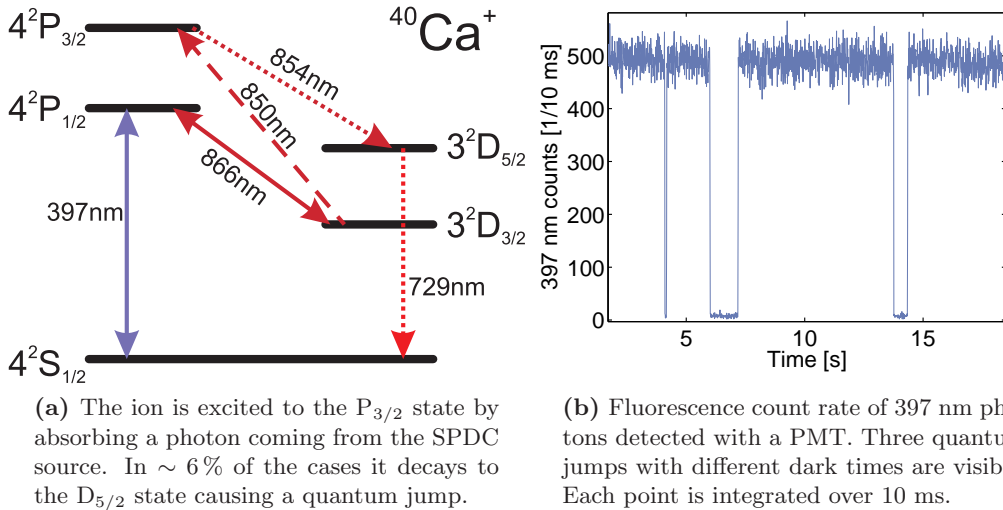


Figure 10.3.: Quantum jumps

from the $D_{5/2}$ state to the $P_{3/2}$ state is equal to the decay probability for the reverse process. This reduces the expected absorption by a factor of approximately $\frac{1}{150}$. Around 3000 photons per second are focused onto the ion. Based on this numbers a rate of close to one quantum jump per minute is expected. Under optimal conditions, i.e. right after alignment of source and HALO's, a rate of 40 quantum jumps per hour is observed. Thermal drifts in the setup might affect the long term rates. However the statistics are too low for reliable conclusions.

Before quantum jumps are recorded, the frequency fine tuning of the photons is assured. The 850 nm fundamental is locked to the 852 nm reference laser via the transfer scheme and is roughly set to the resonance frequency using the wavemeter. Like in section 10.1.2 the ion is illuminated by 397 and 866 nm light of a power corresponding to measurement conditions. Additionally very little power (to avoid light shifts) of 850 and 854 nm is sent to the ion. By the 850 nm light, the steady state population of the $D_{3/2}$ level is slightly reduced and transferred to the $P_{3/2}$ and $D_{5/2}$ levels. The 854 nm laser avoids optical pumping into the $D_{5/2}$ state in which the ion would be dark. By scanning the 850 nm laser over the resonance an inverse excitation spectrum is recorded. Such "dip" spectroscopy is performed prior to each measurement with the SPDC photons to assure that they are resonant (figure 10.4).

The lower part of figure 10.4 shows an analogous scan of the 850 nm detuning, not recording the 397 nm fluorescence but the quantum jumps caused by the laser that is send through the HALO. The 850 nm laser was set to a power (≈ 30000 photons/s) resulting in a high rate of quantum jumps, that were counted for an integration time of 5 minutes in steps of 5 MHz. The solid line is a fitted Lorentzian and the error bars represent Poissonian errors. Both curves in figure 10.4 agree very

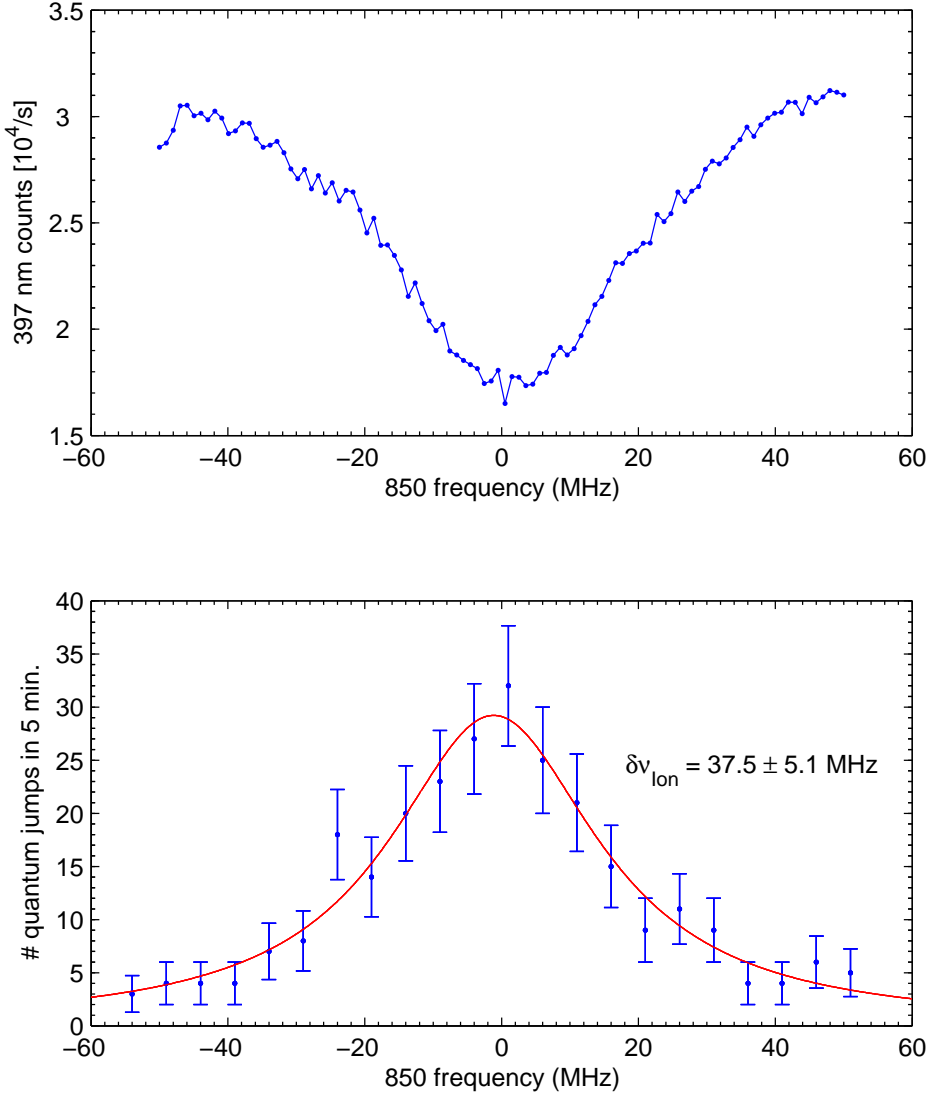


Figure 10.4.: Top: 397 nm fluorescence light for a scan of the 850 nm laser with the 397, 866 and 854 nm lasers additionally coupled to the ion. 850 and 854 nm powers are very weak resulting in a slight reduction of $|D_{3/2}\rangle$ population and 397 nm fluorescence when scanned over the resonance. Bottom: Number of quantum jumps introduced by a weak 850 nm laser beam for a certain frequency. Each point is integrated over 5 minutes. The solid line is a fitted lorentzian and the error bars represent poissonian errors.

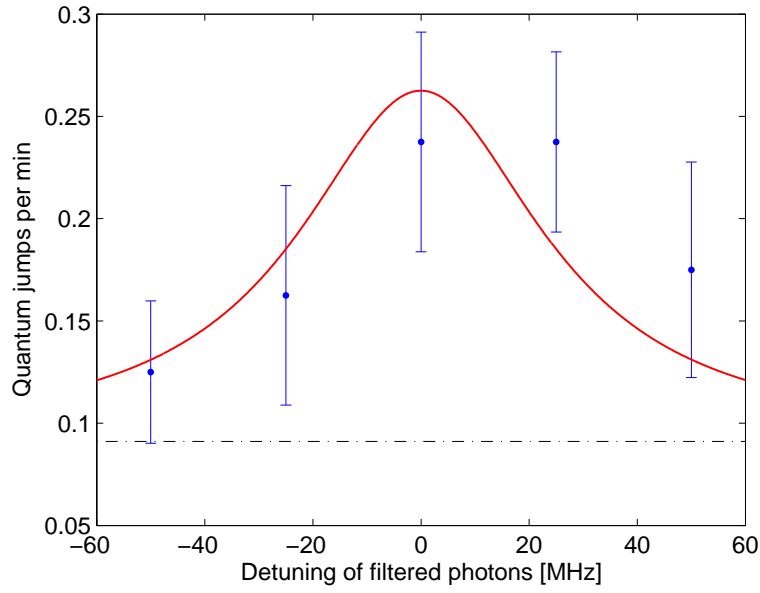


Figure 10.5.: Number of quantum jumps measured as a function of the detuning of the filter cavities. Each point has been integrated over 3 hours distributing the acquisition time for each detuning in fractions of 30 minutes. The error bars represent Poissonian errors and the solid red line is obtained by convoluting the measured transition bandwidth and the measured bandwidth of the down-converted photons .The background level of quantum jumps is indicated with the dashed dotted line.

well and show a linewidth of 37.5 ± 5.1 MHz attributed to the complex 18 level scheme resulting from the involved Zeeman levels.

To prove that the observed quantum jumps (figure 10.3b) are really caused by the absorption of photons coming from the SPDC source two spectroscopy experiments have been performed. In the first experiment the filtered photons were send onto the ion and the number of quantum jumps was measured as a function of the detuning of the filter cavities. Figure 10.5 shows a plot of the quantum jumps for five different detunings. Due to losses in the filter cavities and the fiber that brings the filtered photons to the ion, the count rate is as low as 0.25 quantum jumps per minute on resonance. The error bars in figure 10.5 are Poissonian errors and the solid red line is the expected curve obtained by convoluting the measured transition bandwidth (37 MHz, figure 10.4) and the measured bandwidth of the down-converted photons (22 MHz, 10.1.1). The dashed-dotted line is the background level of quantum jumps attributed to collision with the background gas in the vacuum chamber.

In a second experiment the bandwidth of the down-conversion photons was recorded by tuning the temperature of the KTiOPO₄-crystal and recording the number of filtered photons as well as the number of quantum jumps of the ion. Both curves agree very well and are discussed in [83].

Even at the low observed count rate the measurements confirm that the quantum

jumps are caused by down-converted photons. Single-photon single-ion interaction was hence observed, making an important step towards a single-photon single-atom interface. The next step will be to measure time correlations between trigger photons and quantum jumps (heralded absorption). First experiments show promising results [83]. Alternatives for the realization of a heralded absorption that are being studied in parallel, include pulsed schemes that rely on the detection of single photons rather than quantum jumps and schemes involving absorption on the transition from $D_{5/2}$ to $P_{3/2}$. The future goal is to study the transfer from photon-photon- to atom-photon- or even atom-atom-entanglement (see outlook in chapter 11).

10.2. Pulsed two-photon interference

As mentioned in the introduction of this chapter, two-photon interference under pulsed excitation is an important technological step towards remote entanglement. This is because rather than relying on statistical two-photon coincidences like in the continuous interference shown in chapter 7, in the pulsed case the emission of photons is triggered simultaneously for both ions. After each pulse one can thus check for a possible detection event heralding the entanglement of the two ions, and in case of a positive outcome, perform the necessary state detection or utilize the entanglement.

The indistinguishability of two single photons is essential for the observation of quantum interference between them. For pulsed two-photon interference, the two single ions therefore first need to be transformed into two identical single-photon sources. This was achieved by designing a pulse sequence that first optically pumps the ion into the $D_{3/2}$ state and subsequently excites it into the $P_{1/2}$ state, from where the ion decays by spontaneous emission. The single photon emitted by this process is collected with the HALO lenses and coupled into a single- or multimode fiber.

The characterization of the single photon source will be discussed in detail elsewhere [84] and shall be summarized here only briefly. The pulse sequence to generate single photons starts with a cooling phase in which the 397 and 866 nm lasers are switched on for 500 ns. The repump laser at 866 nm is then switched off for another 500 ns. This efficiently transfers all population of the ion into the state $D_{3/2}$. The last phase, also lasting 500 ns, is the single photon emission and detection phase. The 397 nm laser is switched off and after a short waiting time the 866 nm laser is switched back on. The excitation probability to the $P_{1/2}$ state depends on the applied power of the infrared laser. By varying this power, the temporal shape and bandwidth of the photon produced by the spontaneous Raman process is tuned. It was possible to efficiently create photons with temporal wave packet widths from 70 ns to 2 μ s. The brightness of the source was measured to be 2000 detected photons per second when using a multi-mode fiber and 100 detected photons per second when using a single-mode fiber.

Using these photons their pulsed two-photon interference was measured using the

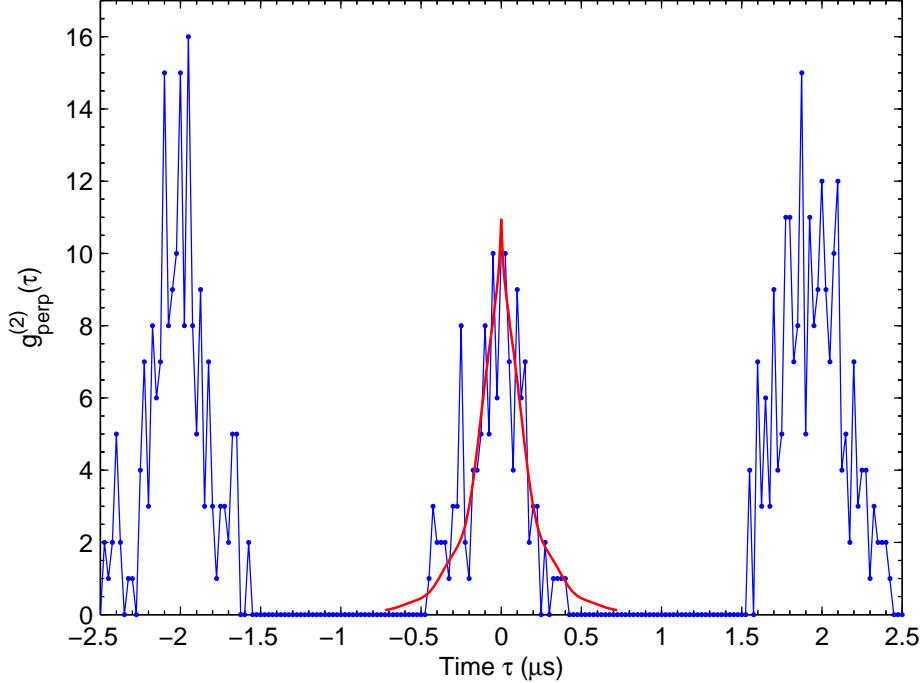


Figure 10.6.: Correlations for distinguishable photons ($g_{\text{perp}}^{(2)}(\tau)$) for a time binning of 25 ns. The single photons are created by a pulse sequence with a repetition rate of 500 kHz, yielding single photon pulses of 250 ns duration.

exact same setup as for the continuous case (figure 7.3). The only difference is that the excitation of the two ions is done using the channels under 90° to the magnetic field (figure 4.9). Moreover, the two $\lambda/2$ plates were replaced by $\lambda/4$ plates, which, in combination with the beam splitters, are set to transmit only σ^+ polarized light. Like in the continuous two-photon interference experiment, the fiber polarization controllers are used to assure indistinguishability of the photons at the fiber beam splitter by maximizing the signal of the PMT after the third PBS.

In order to create fully distinguishable photons, all PBSs and waveplates were removed, thus overlapping photons with arbitrary polarization. Figure 10.6 shows the measured correlation function for distinguishable photons ($g_{\text{perp}}^{(2)}(\tau)$) for a time binning of 25 ns. As discussed in chapter 7.2, the $g^{(2)}$ that is measured in a Hanbury-Brown and Twiss setup, when the light from a single ion is coupled to each input port of a beam splitter respectively, is expected to be 0.5 for time $\tau=0$. Figure 10.6 shows this behavior for the pulsed emission. The PMT is gated to be on only during the detection phase. As expected, the peak at time $\tau=0$ has half the height as the surrounding peaks and its width is twice the gating time of the detectors.

In the case of indistinguishable photons ($g_{\text{par}}^{(2)}(\tau)$), shown in figure 10.7, the peak

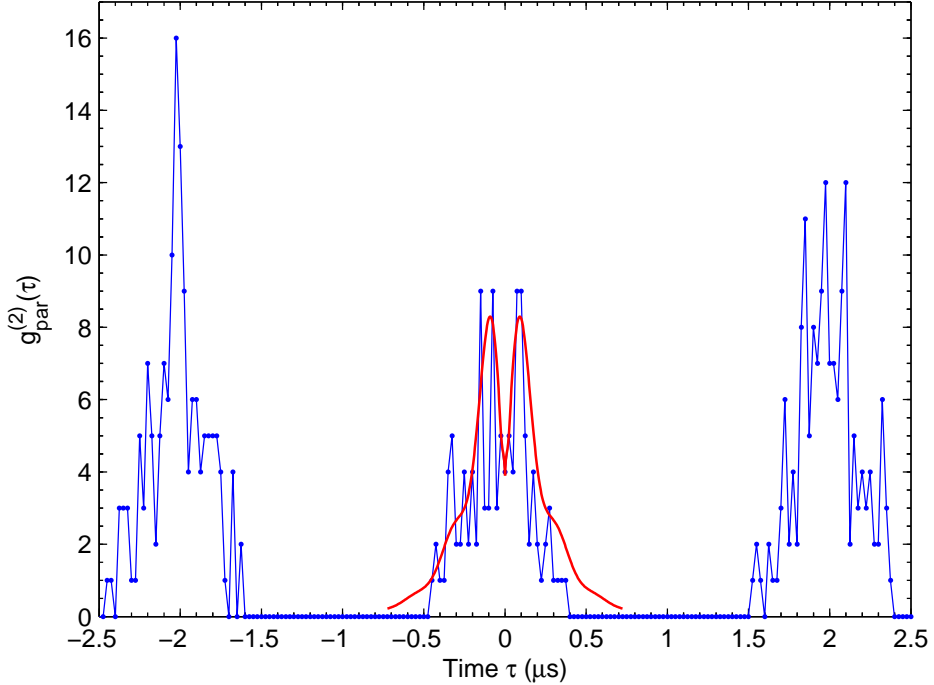


Figure 10.7.: Correlations for indistinguishable photons ($g_{\text{par}}^{(2)}(\tau)$) for a time binning of 25 ns. The single photons are created by a pulse sequence with a repetition rate of 500 kHz, yielding single photon pulses of 250 ns duration.

around time $\tau=0$ exhibits a dip in the center that reveals the interference of the photons. The central peak does not disappear fully because the time resolution of the photon detection is more precise than the temporal spread single photon wave packet. The coherence time of the single photons can be extracted from the time constant of the dip, while the width of the full peak at $\tau = 0$ is determined by the pulse length of the single photon wave packet. In fact the photons that are generated are not fully indistinguishable. The 866 nm pulse during the emission phase is vertically polarized, thus avoiding π transitions. Due to the Zeeman splitting of the $D_{3/2}$ state the σ^+ and σ^- transitions are not frequency degenerate anymore. The blue Raman photons created by this process split up by the corresponding frequency difference. This gives rise to a quantum beat that is observed in the correlation function of the indistinguishable photons [135]. This arises because photons that are overlapping on the beam splitter and that are coming from two different ions, can either have the same frequency or the frequency difference defined by the Zeeman splitting of the $D_{3/2}$ state. The solid lines in both figures take this quantum beat into account and are derived from a model presented with its first observation, using photons generated by a single Rb atom in a high finesse cavity [166]. In theory the central

10.2. Pulsed two-photon interference

dip is supposed to reach zero. The remaining coincidences for $\tau=0$ in figure 10.7 arise from dark counts of the detectors and the limited switching time of the AOM used for the sequence. The residual amplitude of the 397 nm laser in the detection phase leads to a non vanishing probability to create a second photon within this phase. This limitation will be circumvented in the future by the use of an EOM instead of an AOM.

After the realization of the pulsed two-photon interference, the next step towards remote entanglement is atom-photon entanglement. The only remaining technological challenge to do this is the implementation of the state detection of the ions. With the necessary 729 nm laser stabilized and the full functional pulse sequencer it is a realistic goal for the near future of the experiment. Implementing atom-photon entanglement in both traps and the appropriate photon detection setup, leads then to remote entanglement.

10. Towards networking

11. Summary and Outlook

The construction and completion of a new experimental setup, dedicated to the study of quantum networking with trapped and laser cooled $^{40}\text{Ca}^+$ ions is described and first experiments are reported. Two independent linear Paul traps were mounted in two vacuum chambers at a distance of one meter. The coupling of light fields to the trapped ions is optimized through the use of two high numerical aperture in-vacuum lenses in each chamber. A robust, scalable laser stabilization scheme relying on actively stabilized open transfer cavities referenced to an atomic spectroscopy line has been developed and characterized. The completed setup was characterized and calibrated by analyzing excitation spectra.

Two-photon interference of the fluorescence light from two single distant ions, one in each trap, under continuous excitation was realized. A model analysis of the data using eight-level Bloch equations revealed the individual coherence properties of the interfering single photons. The coherence time of the fluorescence light is around 20 ns, indicating that incoherent scattering is dominant. The same measurement was extended to pulsed excitation. This proves the suitability of the setup for remote entanglement and constitutes a significant technological step towards this goal.

At the conceptional level, an analysis of the efficiency of methods for remote entanglement relying on two-photon and single-photon interference was conducted, focussing on the role of the photon detection efficiency. It shows that single-photon schemes are more efficient if the detection efficiency is low (like in present experiments). The created setup is suitable for the realization of both types of protocols, based on single- and on two-photon interference.

Furthermore, the conditioned dynamics of photon emission of a single ion were studied using correlation functions. Second order correlation functions were engineered using polarization dependent detection. This offers a tool in quantum information processing, for example to generate polarization-correlated or anti-correlated photon pairs.

In the near future the apparatus will be used to create network operations such as remote entanglement. After the realization of the pulsed tow-photon interference, the next step is to establish atom-photon entanglement in both traps [61]. To prove atom-photon entanglement, the implementation of state detection of the electronic state of the ion is necessary. This requires the ability to coherently transfer the population of the ion to the $D_{5/2}$ state (shelving) in order to distinguish the two qubit states of the ion (these can be either implemented in the Zeeman sub-states of the $S_{1/2}$ ground state or in the $S_{1/2}$ and $D_{5/2}$ state, respectively). Once atom-photon entanglement has been shown, the creation of remote entanglement is achieved by

11. Summary and Outlook

overlapping the photons from both ions on a beam splitter and implementing the appropriate Bell state measurement at the output of the beam splitter like in [65]. The 729 nm laser, used for shelving, has already been stabilized to the Cs cell via the transfer scheme. Linewidth (150 kHz) and available power should allow for Rabi flopping on the μs scale. All necessary tools are available, the realization of remote entanglement with the apparatus is thus a realistic goal for the next months.

As mentioned, the setup also allows for the realization of remote entanglement based on single-photon interference. The major technical challenge in this case is to achieve interferometric stability of the setup. Although difficult, this was achieved with a similar setup in the past [85]. Interference of the fluorescence light from a single ion with its mirror image was observed by stabilizing the macroscopic path difference between the ion and the piezo-mounted mirror to sub-wavelength stability. Using the same technique, the realization of single-photon interference from two distant atoms seems feasible. Furthermore, the emission properties of the single photons, and therefore their coherence time, can be controlled through the applied laser pulse sequence, as described in chapter 10.2. This is crucial, because for the method to work the photons have to be coherent along the two paths from the ions to the detector. Also for this scheme, with the implementation of state detection, all necessary tools are available. The general perspective for the future is to study the different entanglement methods quantitatively as discussed in chapter 8.

With the purpose to study single-photon single-ion interfaces, one of the two traps could be linked to a Spontaneous Parametric Down-Conversion source resonant with an electronic transition in $^{40}\text{Ca}^+$. The absorption of a single photon from this source by a single ion was shown by detecting quantum jumps of the electronic state of the ion (chapter 10.1). After the accomplishment of single-photon single-atom interaction, the possibility of realizing heralded absorption of a single photon by a single atom seems particularly interesting. Other groups have recently presented single-atom single-photon interfaces [167], however this work does not bear the potential of entanglement transfer from photons to atoms. The implementation of heralded absorption that our setup is capable of, offers this alternative way of establishing remote entanglement.

In fact first evidence of a correlation between the quantum jumps induced by the SPDC signal photon and the filtered idler photon have been observed in the laboratory. Due to high dark count background in the trigger arm and an unexpected low quantum efficiency of the detector, these correlation were difficult to distinguish from the noise. By implementing a scheme that makes use of the enhanced absorption probability from the $D_{5/2}$ to the $P_{3/2}$ state, the statistics will be improved. This scheme, and upgrading to a better detector are expected to increase the rate of correlation events by two orders of magnitude. The only changes that have to be introduced to the setup are the tuning of the SPDC source to 854 nm and the 854 nm laser to 850 nm. Operating this scheme in a pulsed fashion, i.e. to enhance the absorption probability of the photon by repeated optical pumping into the $D_{5/2}$ state, can further increase the efficiency. The perspective of realizing heralded absorption

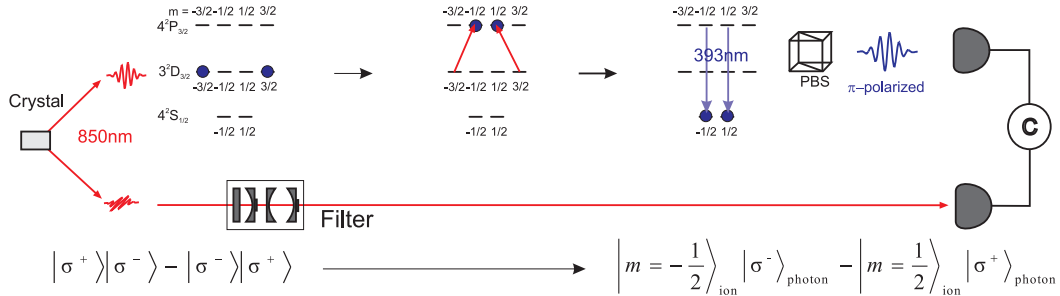


Figure 11.1.: Sketch of the transfer from the photon-photon entanglement of a SPDC source to atom-photon entanglement using $^{40}\text{Ca}^+$. A coincidence detection at the two detectors heralds the transfer of entanglement producing the state $\psi'^- = \frac{1}{\sqrt{2}}(|m = -1/2\rangle_{\text{ion}}|\sigma^-\rangle_{\text{photon}} - |m = 1/2\rangle_{\text{ion}}|\sigma^+\rangle_{\text{photon}})$.

very soon, makes it a primary goal for the immediate future.

Controlling the absorption of down-converted photons by a single ion would be a first important step towards entanglement transfer from photons to atoms. Figure 11.1 illustrates how the transfer from photon-photon entanglement to atom-photon entanglement could work. A single $^{40}\text{Ca}^+$ ion is prepared in a coherent superposition of the $D_{3/2}$, $m_f = -3/2$ and $m_f = 3/2$ state. The SPDC source generates the polarization entangled state $\psi^- = \frac{1}{\sqrt{2}}(|\sigma^+\rangle|\sigma^-\rangle - |\sigma^-\rangle|\sigma^+\rangle)$ at 850 nm. One of the down-converted photons is sent to the ion and the other one through the filtering stage onto a detector. If the first photon gets absorbed by the ion, its population is transferred to a coherent superposition of the $P_{3/2}$, $m_f = -1/2$ and $m_f = 1/2$ state. From the $P_{3/2}$ state the ion decays with a high probability to the $S_{1/2}$ ground state. Only the π polarized photons that are emitted by this process are filtered and detected by a second detector. A coincidence event at both detectors then heralds the transfer from photon-photon to atom-photon entanglement producing the state $\psi'^- = \frac{1}{\sqrt{2}}(|m = -1/2\rangle_{\text{ion}}|\sigma^-\rangle_{\text{photon}} - |m = 1/2\rangle_{\text{ion}}|\sigma^+\rangle_{\text{photon}})$.

Sending the second photon to a second ion, thereby applying this scheme in both arms, would ultimately yield the transfer from photon-photon entanglement to atom-atom entanglement. The observation of the heralded absorption would prove the feasibility of these schemes with our setup.

The setup constructed during this thesis is one of the first pioneering devices that are suitable to study the principles of quantum networking with single atoms. The results summarized in this chapter prove its full functionality. The outlined perspectives show that interesting contributions to the field of quantum information processing are expected in the near future.

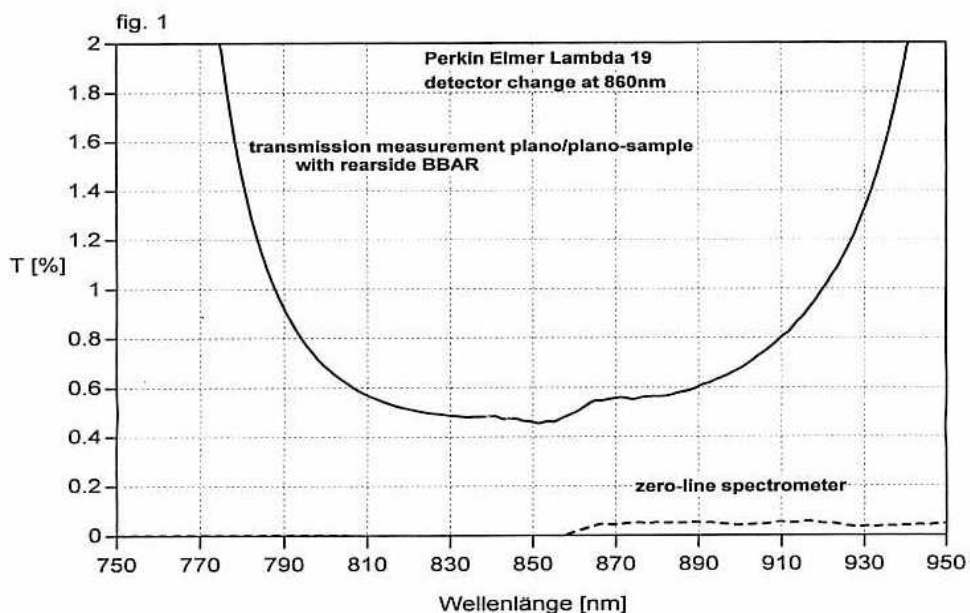
11. Summary and Outlook

A. Transmission of cavity mirrors

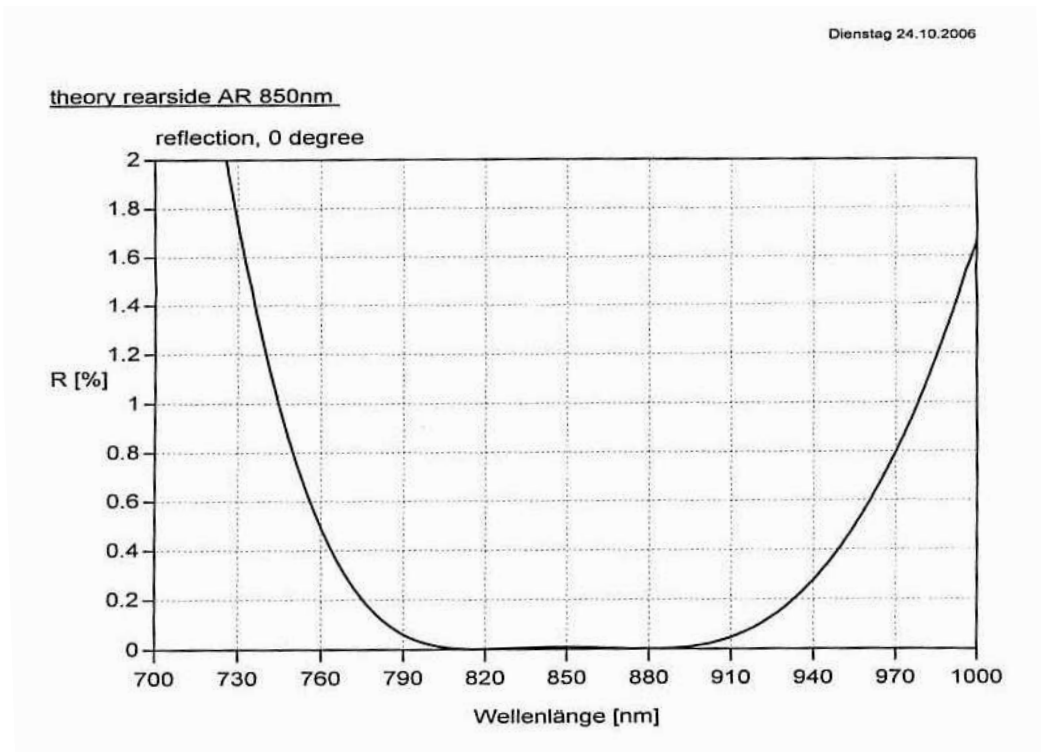
The following plots show the specifications of the mirrors used for the transfer-cavities.

Dienstag 24.10.2006

batch Z1006038 low loss mirror with R=99.5% 850nm and T=0.5% 850nm



A. Transmission of cavity mirrors



B. Practical advice

This appendix collects practical advice for readers who intent to operate the presented setup. The remarks are structured according to the chapter that they belong to.

4.2.6 Cavity Locker

PT100 temperature sensor

The PT100 temperature sensor, which is compared to the potentiometer setting is very sensitive. Therefore already very small pick up in the sensor cables can disturb the stabilization and lead to temperature oscillations. No radio frequency sources, such as mobile phones or walkie talkies, should be operated in the close vicinity of the cavities.

PDH error signal

The error signal generated by the PDH module of the cavity locker has to be sufficiently big for the magic button function to work. Having the set point at 1.25 V the maximum of the error signal has to be bigger then 2 V and the minimum lower then 0.5 V. Otherwise the cavity locker can not identify the next mode. This thresholds, like all compensator gains and the scanning speed, can be changed via software.

Temperature stabilization

The temperature stabilization tends to regulate to either very high or very low temperatures if the cavity falls out of lock but is left in control mode. This happens because, if the piezo is not able to keep the cavity locked it will however try to do so by regulating over its full range. Since the temperature is programmed to follow the piezo it will try to compensate and regulate to higher or lower temperature depending on the sign of the amplitude of the piezo. Although there is a software limitation, it is advisable not to leave the cavity locker in control mode if it is out of lock at any time.

7.3 Two-photon interference setup

To produce a "fake ion" on the CCD camera, a weak laser beam, derived from the zero order transmission of the 397 nm AOM, is coupled to one of the output ports (I_3 , I_4) of the fiber beam splitter. The blue laser light is thus focussed into each trap by the first HALO and collected by the second one on the other side of the

B. Practical advice

trap (see figure 4.9). If the second HALO is aligned in a way that the trapped ion is well focussed onto the camera, then focussing the 397 nm laser light ("fake ion") onto the camera and overlapping it with the real ion image also couples the counter-propagating fluorescence light into the fiber beam splitter. The focussing and overlapping of fake and real ion is achieved by aligning the fiber out-coupler and the first HALO in all directions. Once the first signal of the fluorescence light is detected with the PMTs, maximizing the signal is straightforward.

C. Matlab code for Allan variance

If $y(t)$ is a data set of subsequent time averaged frequency values $\bar{y}_{i,\tau}$, the following matlab code calculates the Allan variance $\sigma_y^2(\tau)$ for the averaging time τ .

```
for t=1:size(y,1)/2
z=zeros(floor(size(y,1)/t),1);
for i=1:size(y,1)/t
    z(i)=sum(y((i-1)*t+1:t*i))./t;
end
sigma_y^2(t)=1/2*mean(((z(2:end)-z(1:end-1))./377106090562990).^ 2);
end
```

C. Matlab code for Allan variance

D. Derivation of PDH fit function

The electric field incident on the cavity for weak current modulation, can be written as

$$E_{in}(t) \propto (1 + 2N \cos(\Omega t + \Phi)) e^{i(\omega t + 2M \sin \Omega t)} \quad (\text{D.1})$$

$$\propto e^{i\omega t} + N \left[e^{i(\omega t + \Omega t + \Phi)} + e^{i(\omega t - \Omega t - \Phi)} \right] \quad (\text{D.2})$$

$$+ M \left[e^{i(\omega t + \Omega t)} - e^{i(\omega t - \Omega t)} \right] + c.c., \quad (\text{D.3})$$

with N being the amplitude of the amplitude modulation, M being the amplitude of the phase modulation, ω the laser frequency, Ω the frequency of the current modulation and Φ the relative phase between the amplitude and phase modulation. Modulating the current of a diode laser always yields both amplitude and phase modulation. To account for this the factor $(1 + 2N \cos(\Omega t + \Phi))$ has to be included with respect to the usual phase modulation approach [105].

According to [105] the reflected field E_{ref} can be found by using

$$f(\omega) = \frac{E_{ref}}{E_{in}} = \frac{r(\exp(i\frac{\omega}{\Delta\nu_{fsr}}) - 1)}{1 - r^2 \exp(i\frac{\omega}{\Delta\nu_{fsr}})}. \quad (\text{D.4})$$

The photodiode in reflection detects the intensity $I \propto |E_{ref}|^2$ of the reflected beam. The Pound-Drever module detects only the part of the electric signal proportional to $\propto e^{\pm i\Omega t}$. Using this the signal can be written as

$$\begin{aligned} I &\propto e^{\pm i\Omega t} \\ &\propto N f(\omega) \left[f^*(\omega + \Omega) e^{-i(\Omega t + \Phi)} + f^*(\omega - \Omega) e^{+i(\Omega t + \Phi)} \right] \\ &\quad + M f(\omega) \left[f^*(\omega + \Omega) e^{-i(\Omega t)} - f^*(\omega - \Omega) e^{+i(\Omega t)} \right] + c.c.. \end{aligned}$$

Using $e^{-i\Omega t} = \cos \Omega t - i \sin \Omega t$ and rearranging yields

$$\begin{aligned} I &\propto N \left[f(\omega) f^*(\omega + \Omega) e^{-i\Phi} + f^*(\omega) f(\omega - \Omega) e^{-i\Phi} \right] (\cos \Omega t - i \sin \Omega t) \\ &\quad + N \left[f^*(\omega) f(\omega + \Omega) e^{+i\Phi} + f(\omega) f^*(\omega - \Omega) e^{+i\Phi} \right] (\cos \Omega t + i \sin \Omega t) \\ &\quad + M \left[f(\omega) f^*(\omega + \Omega) - f^*(\omega) f(\omega - \Omega) \right] (\cos \Omega t - i \sin \Omega t) \\ &\quad + M \left[f^*(\omega) f(\omega + \Omega) - f(\omega) f^*(\omega - \Omega) \right] (\cos \Omega t + i \sin \Omega t). \end{aligned}$$

D. Derivation of PDH fit function

We can now express the intensity I in terms of the function $K(\omega, \Omega)$

$$I \propto 2 \cdot \Re [K(\omega, \Omega)] \cos \Omega t + 2 \cdot \Im [K(\omega, \Omega)] \sin \Omega t \quad (\text{D.5})$$

with

$$K(\omega, \Omega) = Ne^{-i\Phi} [f(\omega)f^*(\omega + \Omega) + f^*(\omega)f(\omega - \Omega)] \quad (\text{D.6})$$

$$+ Me^{-i\Phi} [f(\omega)f^*(\omega + \Omega) - f^*(\omega)f(\omega - \Omega)] \quad (\text{D.7})$$

E. Matlab codes for fit to PDH error signal

E.1. find_b0.m

To find the initial starting parameters for the fit of $K(\omega, \Omega)$ to the data the matlab file find_b0.m is used.

find_b0.m:

```
% initial fit parameters
b0(1)=0.9862; % reflectivity r
b0(2)=0.0542; % FSR
b0(3)=0.0014; % amplitude of AM
b0(4)=0.0436; % amplitude of PM
b0(5)=-0.2330; % AM-PM relative phase
b0(6)=1.3199; % phase of detection
b0(7)=0.0026; % b(7)=modulation
b0(8)=-0.0003; % b(8)=x-offset
b0(9)=-0.0216; % b(9)=y-offset
```

```
yi=K_apm(b0,error_t);
```

```
figure(1)
plot(error_t,error)
hold on
plot(error_t,yi,'r')
hold off
```

E.2. $K(\omega, \Omega)$

K_apm.m:

```
function K=K_apm(b,x)
echo off;
```

E. Matlab codes for fit to PDH error signal

```
% Parameters:
%b(1)=reflectivity r,
%b(2)=FSR,
%b(3)=amplitude of AM,
%b(4)=amplitude of PM,
%b(5)=AM-PM relative phase,
%b(6)=phase of detection,
%b(7)=modulation,
%b(8)=x-offset,
%b(9)=y-offset,

x = x + b(8);
f0 = b(1).*(exp(i*2*pi*x./b(2))-1.0)./(1.0-b(1)^2
.*exp(i*2*pi*x./b(2)));
fp = b(1).*(exp(i*2*pi*(x+b(7))./b(2))-1.0)./(1.0-b(1)^2
.*exp(i*2*pi*(x+b(7))./b(2)));
fm = b(1).*(exp(i*2*pi*(x-b(7))./b(2))-1.0)./(1.0-b(1)^2
.*exp(i*2*pi*(x-b(7))./b(2)));

K = real(exp(i*b(6))*(b(3)*exp(i*b(5))*(f0.*conj(fp)+conj(f0).*fm)
+b(4).*(f0.*conj(fp)-conj(f0).*fm)))+ b(9);
```

E.3. fit_PDH.m

When a reasonable good overlap between the data and $K(\omega, \Omega)$ has been achieved with find_b0.m, the b0's are entered into fit_PDH.m as initial values.
fit_PDH.m fits the function $K(\omega, \Omega)$ to the data.

```
fit_PDH.m:
function pph = fit_PDH(xdata,ydata);

% initial fit parameters
b0(1)=0.9862; % reflectivity r
b0(2)=0.0542; % FSR
b0(3)=0.0014; % amplitude of AM
b0(4)=0.0436; % amplitude of PM
b0(5)=-0.2330; % AM-PM relative phase
b0(6)=1.3199; % phase of detection
b0(7)=0.0026; %b(7)=modulation
b0(8)=-0.0003; %b(8)=x-offset
b0(9)=-0.0216; %b(9)=y-offset
```

```

yi=K_apm(b0,xdata);
pph = nlinfit(xdata,ydata,@K_apm,b0); % fit of a error function to the data
yfit=K_apm(pph,xdata);

figure(2),
% subplot(2,4),
plot(xdata,ydata)
hold on
plot(xdata,yfit,'r');
grid;
hold off
pph
%pause

```

E.4. slope.m

slope.m calculates the slope of the fit of the error signal, plots it and returns position and value of the maximum and minimum slope.

slope.m:

```

% initial fit parameters
b0(1)=0.9862; % reflectivity r
b0(2)=0.0542; % FSR
b0(3)=0.0014; % amplitude of AM
b0(4)=0.0436; % amplitude of PM
b0(5)=-0.2330; % AM-PM relative phase
b0(6)=1.3199; % phase of detection
b0(7)=0.0026; %b(7)=modulation
b0(8)=-0.0003; %b(8)=x-offset
b0(9)=-0.0216; %b(9)=y-offset

error_tm1=error_t(1:length(error_t)-1); %reduces dimension of error_t to fit dim of
d
error_m1=error(1:length(error)-1); %reduces dimension of error to be plotted

yi=K_apm(b0,error_t); %calculate K_apm with b0
d=diff(yi); %difference of yi_2-yi_1 .... yi_n-yi_(n-1)
t=diff(error_t); %same for error_t
d=d./t; %derivative or slope of signal

```

E. Matlab codes for fit to PDH error signal

```
figure(3)
plot(error_tm1,errorm1)
hold on
plot(error_tm1,d,'r')
%hold off

%[s,i]=max(d) %returns maximum value and it's indice of d
%[s,i]=min(d)
ts=error_tm1(i)

z=-s;
X=[ts,ts];
Y=[z,s];
line(X,Y,'Color','k')
hold off
```

Bibliography

- [1] R. P. Feynman. Simulating physics with computers. *Int. J. Theor. Phys.*, 21:467–488, 1982.
- [2] R. P. Feynman. Quantum mechanical computers. *Found. Phys.*, 16:507–531, 1986.
- [3] D. Deutsch. Quantum theory, the church-turing principle and the universal quantum computer. *Proceedings of the Royal Society of London; Series A, Mathematical and Physical Sciences*, 400 (1818):97–117, 1985.
- [4] D. Deutsch. Quantum computational networks . . . *Proc. Roy. Soc.*, 425(1868):73–90, 1989.
- [5] D. Deutsch and R. Jozsa. Rapid solutions of problems by quantum computation. *Proceedings of the Royal Society of London, Series A*, 439:553, 1992.
- [6] S. Gulde, M. Riebe, G.P.T. Lancaster, C. Becher, J. Eschner, H. Häffner, F. Schmidt-Kaler, I. L. Chuang, and R. Blatt. Implementing the deutsch-jozsa algorithm on an ion-trap quantum computer. *Nature*, 421:48, 2003.
- [7] P. W. Shor. Algorithms for quantum computation: Discrete logarithms and factoring. *Proc. 35th Annual Symposium of Foundations of Computer Science*, 1994.
- [8] L. K. Grover. Quantum mechanics helps in searching for a needle in a haystack. *Phys. Rev. Lett.*, 79(2):325–328, Jul 1997.
- [9] R. Jozsa and N. Linden. On the role of entanglement in quantum computational speed-up. *arXiv:0201143v2 [quant-ph]*, 2002.
- [10] A. M. Steane. Error correcting codes in quantum theory. *Phys. Rev. Lett.*, 77(5):793–797, Jul 1996.
- [11] P. W. Shor. Scheme for reducing decoherence in quantum computer memory. *Phys. Rev. A*, 52(4):R2493–R2496, Oct 1995.
- [12] P. W. Shor. Fault-tolerant quantum computation. *37th Symposium on Foundations of Computing, IEEE Computer Society Press and arXiv.org:quant-ph/9605011*, pages 56–65, 1996.

Bibliography

- [13] J. Benhelm, G. Kirchmair, C.F. Roos, and R. Blatt. Towards fault-tolerant quantum computing with trapped ions. *Nature Physics*, 4:463 – 466, 2008.
- [14] H. J. Briegel, T. Calarco, D. Jaksch, J. I. Cirac, and P. Zoller. Quantum computing with neutral atoms. *Journal of Modern Optics*, 47, 2:415–451, 2000.
- [15] J. I. Cirac and P. Zoller. A scalable quantum computer with ions in an array of microtraps. *Nature*, 404:579–581, 2000.
- [16] N. A. Gershenfeld and I. L. Chuang. Bulk Spin-Resonance Quantum Computation. *Science*, 275(5298):350–356, 1997.
- [17] B. E. Kane. A silicon-based nuclear spin quantum computer. *Nature*, 393:133–137, 1998.
- [18] Y. Makhlin, G. Schön, and A. Shnirman. Quantum-state engineering with josephson-junction devices. *Rev. Mod. Phys.*, 73(2):357–400, May 2001.
- [19] J. M. Fink, M. Goppl, M. Baur, R. Bianchetti, P. J. Leek, A. Blais, and A. Wallraff. Climbing the jaynes-cummings ladder and observing its nonlinearity in a cavity qed system. *Nature*, 454:315–318, 2008.
- [20] R. Hanson, L. P. Kouwenhoven, J. R. Petta, S. Tarucha, and L. M. K. Vandersypen. Spins in few-electron quantum dots. *Reviews of Modern Physics*, 79(4):1217, 2007.
- [21] D. Loss and D. P. DiVincenzo. Quantum computation with quantum dots. *Phys. Rev. A*, 57(1):120–126, Jan 1998.
- [22] D. P. DiVincenzo. The physical implementation of quantum computation. *Fortschr. Phys.*, 48:771–783, 2000.
- [23] D. J. Wineland, J. C. Bergquist, W. M. Itano, and R. E. Drullinger. Double-resonance and optical-pumping experiments on electromagnetically confined, laser-cooled ions. *Opt. Lett.*, 5(6):245, 1980.
- [24] Th. Sauter, W. Neuhauser, R. Blatt, and P. E. Toschek. Observation of quantum jumps. *Phys. Rev. Lett.*, 57(14):1696–1698, Oct 1986.
- [25] W. Nagourney, J. Sandberg, and H. Dehmelt. Shelved optical electron amplifier: Observation of quantum jumps. *Phys. Rev. Lett.*, 56(26):2797–2799, Jun 1986.
- [26] J. C. Bergquist, Randall G. Hulet, W. M. Itano, and D. J. Wineland. Observation of quantum jumps in a single atom. *Phys. Rev. Lett.*, 57(14):1699–1702, Oct 1986.

- [27] J.J. Bollinger, D.J. Heinzen, W.M. Itano, S.L. Gilbert, and D.J. Wineland. A 303 mhz frequency standard based on trapped be^+ ions. *IEEE T. Instrum. Meas.*, 40:126–128.
- [28] J. I. Cirac and P. Zoller. Quantum computations with cold trapped ions. *Phys. Rev. Lett.*, 74(20):4091–4094, May 1995.
- [29] C. Monroe, D. M. Meekhof, B. E. King, W. M. Itano, and D. J. Wineland. Demonstration of a fundamental quantum logic gate. *Phys. Rev. Lett.*, 75(25):4714–4717, Dec 1995.
- [30] C. A. Sackett, D. Kielpinski, B. E. King, C. Langer, V. Meyer, C. J. Myatt, M. Rowe, Q. A. Turchette, W. M. Itano, D. J. Wineland, and Monroe C. Experimental entanglement of four particles. *Nature*, 404:256–259, 2000.
- [31] B. DeMarco, A. Ben-Kish, D. Leibfried, V. Meyer, M. Rowe, B. M. Jelenković, W. M. Itano, J. Britton, C. Langer, T. Rosenband, and D. J. Wineland. Experimental demonstration of a controlled-not wave-packet gate. *Phys. Rev. Lett.*, 89(26):267901, Dec 2002.
- [32] D. Leibfried, B. DeMarco, V. Meyer, D. Lucas, M. Barrett, J. Britton, W. M. Itano, B. Jelenkovic, C. Langer, T. Rosenband, and D. J. Wineland. Experimental demonstration of a robust, high-fidelity geometric two ion-qubit phase gate. *Nature*, 422:412–415, 2003.
- [33] P. C. Haljan, K.-A. Brickman, L. Deslauriers, P. J. Lee, and C. Monroe. Spin-dependent forces on trapped ions for phase-stable quantum gates and entangled states of spin and motion. *Phys. Rev. Lett.*, 94(15):153602, Apr 2005.
- [34] F. Schmidt-Kaler, H. Häffner, M. Riebe, S. Gulde, G.P.T. Lancaster, T. Deusdle, C. Becher, C.F. Roos, J. Eschner, and R. Blatt. Realization of the cirac-zoller controlled-not quantum gate. *Nature*, 422:408–411, 2003.
- [35] F. Schmidt-Kaler, H. Häffner, S. Gulde, M. Riebe, G. P. T. Lancaster, T. Deusdle, C. Becher, W. Hänsel, J. Eschner, C. F. Roos, and R. Blatt. How to realize a universal quantum gate with trapped ions. *Appl. Phys. B*, 77:789, 2003.
- [36] J.P. Home, M.J. McDonnell, D.M. Lucas, G. Imreh, B.C. Keitch, D.J. Szwer, N.R. Thomas, S.C. Webster, D.N. Stacey, and A.M. Steane. Deterministic entanglement and tomography of ion-spin qubits. *New J. Phys.*, 8:188, 2006.
- [37] M. Riebe, H. Häffner, C. F. Roos, W. Hänsel, J. Benhelm, G. P. T. Lancaster, T. W. Körber, C. Becher, F. Schmidt-Kaler, D. F. V. James, and R. Blatt. Deterministic quantum teleportation with atoms. *Nature*, 429:734–737, 2004.
- [38] M. D. Barrett, J. Chiaverini, T. Schaetz, J. Britton, J. D. tano, W. M. Iand Jost, E. Knill, C. Langer, D. Leibfried, R. Ozeri, and D. J. Wineland.

Bibliography

- Deterministic quantum teleportation of atomic qubits. *Nature*, 429:737–739, 2004.
- [39] J. Chiaverini, D. Leibfried, T. Schaetz, M. D. Barrett, R. B. Blakestad, J. Britton, W. M. Itano, J. D. Jost, E. Knill, C. Langer, R. Ozeri, and D. J. Wineland. Realization of quantum error correction. *Nature*, 432:602–605, 2004.
- [40] R. Reichle, D. Leibfried, E. Knill, J. Britton, R. B. Blakestad, J. D. Jost, C. Langer, R. Ozeri, S. Seidelin, and D. J. Wineland. Experimental purification of two-atom entanglement. *Nature*, 443:838–841, 2006.
- [41] C. F. Roos, M. Riebe, H. Haffner, W. Hansel, J. Benhelm, G. P. T. Lancaster, C. Becher, F. Schmidt-Kaler, and R. Blatt. Control and Measurement of Three-Qubit Entangled States. *Science*, 304(5676):1478–1480, 2004.
- [42] D. Leibfried, E. Knill, S. Seidelin, J. Britton, R. B. Blakestad, J. Chiaverini, D. B. Hume, W. M. Itano, J. D. Jost, C. Langer, R. Ozeri, R. Reichle, and D. J. Wineland. Creation of a six-atom ‘schrödinger cat’ state. *Nature*, 438:639–642, 2005.
- [43] H. Häffner, W. Hänsel, C. F. Roos, J. Benhelm, D. Chek-al-kar, M. Chwalla, T. Körber, U. D. Rapol, M. Riebe, P. O. Schmidt, C. Becher, O. Gühne, Dür W., and R. Blatt. Scalable multiparticle entanglement of trapped ions. *Nature*, 438:643–646, 2005.
- [44] K.-A. Brickman, P. C. Haljan, P. J. Lee, M. Acton, L. Deslauriers, and C. Monroe. Implementation of grover’s quantum search algorithm in a scalable system. *Phys. Rev. A*, 72(5):050306, Nov 2005.
- [45] D.J. Wineland, C. Monroe, W.M. Itano, D. Liebfried, B.E. King, and D.M. Meekhof. Experimental issues in coherent quantum-state manipulation of trapped atomic ions. *J. Res. Natl. Inst. Stand. Technol.*, 103(3), 1998.
- [46] D. Kielpinski, C. Monroe, and D. J. Wineland. Architecture for a large-scale ion-trap quantum computer. *Nature*, 417:709–711, 2002.
- [47] M. M. Salomaa and M. Nakahara. Divincenzo criteria and beyond.
- [48] W.-Y. Hwang. Quantum key distribution with high loss: Toward global secure communication. *Phys. Rev. Lett.*, 91(5):057901, Aug 2003.
- [49] V. Scarani, A. Acín, G. Ribordy, and N. Gisin. Quantum cryptography protocols robust against photon number splitting attacks for weak laser pulse implementations. *Phys. Rev. Lett.*, 92(5):057901, Feb 2004.
- [50] F. Grosshans, G. V. Assche, J. Wenger, R. Brouri, N. J. Cerf, and P. Grangier. Quantum key distribution using gaussian-modulated coherent states. *Nature*, 421:238–241, 2002.

- [51] A. Beveratos, R. Brouri, T. Gacoin, A. Villing, J.-P. Poizat, and P. Grangier. Single photon quantum cryptography. *Phys. Rev. Lett.*, 89(18):187901, Oct 2002.
- [52] H.-J. Briegel, W. Dür, J. I. Cirac, and P. Zoller. Quantum repeaters: The role of imperfect local operations in quantum communication. *Phys. Rev. Lett.*, 81(26):5932–5935, Dec 1998.
- [53] P. Zoller et al. Quantum information processing and communication. *Eur. Phys. J. D*, 36:203, 2005.
- [54] B. Julsgaard, Alexander Kozhekin, and Eugene S. Polzik. Experimental long-lived entanglement of two macroscopic objects. *Nature*, 413:400–403, 2001.
- [55] B. Julsgaard, J. Sherson, J. I. Cirac, J. Fiurásek, and E. S. Polzik. Experimental demonstration of quantum memory for light. *Nature*, 432:482–486, 2004.
- [56] C. W. Chou, H. de Riedmatten, D. Felinto, S. V. Polyakov, S. J. van Enk, and H. J. Kimble. Measurement-induced entanglement for excitation stored in remote atomic ensembles. *Nature*, 438:828–832, 2005.
- [57] T. Chanelière, D. N. Matsukevitch, S. D. Jenkins, S. Y. Lan, T. A. B. Kennedy, and A. Kuzmich. Storage and retrieval of single photons transmitted between remote quantum memories. *Nature*, 438:833, 2005.
- [58] M. D. Eisaman, A. Andra, F. Massou, M. Fleischhauer, A. S. Zibrov, and M. D. Lukin. Electromagnetically induced transparency with tunable single-photon pulses. *Nature*, 438:837, 2005.
- [59] C. Cabrillo, J. I. Cirac, P. García-Fernández, and P. Zoller. Creation of entangled states of distant atoms by interference. *Phys. Rev. A*, 59(2):1025–1033, Feb 1999.
- [60] S. Bose, P. L. Knight, M. B. Plenio, and V. Vedral. Proposal for teleportation of an atomic state via cavity decay. *Phys. Rev. Lett.*, 83(24):5158–5161, Dec 1999.
- [61] B. B. Blinov, D. L. Moehring, L. M. Duan, and C. Monroe. Observation of entanglement between a single trapped atom and a single photon. *Nature*, 428:153, 2004.
- [62] X.-L. Feng, Z.-M. Zhang, X.-D. Li, S.-Q. Gong, and Z.-Z. Xu. Entangling distant atoms by interference of polarized photons. *Phys. Rev. Lett.*, 90(21):217902, May 2003.
- [63] L.-M. Duan and H. J. Kimble. Efficient engineering of multiatom entanglement through single-photon detections. *Phys. Rev. Lett.*, 90(25):253601, Jun 2003.

Bibliography

- [64] C. Simon and W. T. M. Irvine. Robust long-distance entanglement and a loophole-free bell test with ions and photons. *Phys. Rev. Lett.*, 91(11):110405, Sep 2003.
- [65] D. L. Moehring, P. Maunz, S. Olmschenk, K. C. Younge, D. N. Matsukevich, Duan L. M., and C. Monroe. Entanglement of single-atom quantum bits at a distance. *Nature*, 449:68, 2007.
- [66] D. N. Matsukevich, P. Maunz, D. L. Moehring, S. Olmschenk, and C. Monroe. Bell inequality violation with two remote atomic qubits. *Physical Review Letters*, 100(15):150404, 2008.
- [67] S. Olmschenk, D. N. Matsukevich, P. Maunz, D. Hayes, L.-M. Duan, and C. Monroe. Quantum teleportation between distant matter qubits. *Science*, 323(5913):486–489, 2009.
- [68] S. Zippilli, G. A. Olivares-Renteria, G. Morigi, C. Schuck, F. Rohde, and J. Eschner. Entanglement of distant atoms by projective measurement: The role of detection efficiency. *New J. Phys.*, 10:103003, 2008.
- [69] W. Paul, O. Osberghaus, and E. Fischer. Ein ionenkäfig. *Forschungsberichte des Wirtschafts- und Verkehrsministeriums Nordrhein-Westfalen 415, Westfälischer Verlag*, 1958.
- [70] W. Neuhauser, M. Hohenstatt, P. E. Toschek, and H. Dehmelt. Localized visible Ba^+ mono-ion oscillator. *Phys. Rev. A*, 22(3):1137–1140, Sep 1980.
- [71] R. P. Gosh. *Ion traps*. Clarendon Press, 1995.
- [72] C. Roos. *Controlling the Quantum State of Trapped Ions*. PhD thesis, Leopold-Franzens-Universität Innsbruck, 2000.
- [73] M. Riebe. *Preparation of entangled states and quantum teleportation with atomic qubits*. PhD thesis, Leopold-Franzens-Universität Innsbruck, 2005.
- [74] C. Raab. *Interference experiments with the fluorescence light of Ba^+ ions*. PhD thesis, Leopold-Franzens-Universität Innsbruck, 2001.
- [75] S. Gulde. *Experimental realization of quantum gates and the deutsch-josza algorithm with trapped 40Ca^+ ions*. PhD thesis, Universität Innsbruck, 2003.
- [76] H. C. Nägerl. *Ion Strings for Quantum Computation*. PhD thesis, Leopold-Franzens-Universität Innsbruck, 1998.
- [77] D. Rotter. *Quantum feedback and quantum correlation measurements with a single Barium ion*. PhD thesis, Leopold-Franzens-Universität Innsbruck, 2008.
- [78] M. Drewsen and A. Brøner. Harmonic linear paul trap: Stability diagram and effective potentials. *Phys. Rev. A*, 62(4):045401, Sep 2000.

- [79] F. Riehle. *Frequency Standards*. Wiley-Vch, 2004.
- [80] D. W. Allan. Statistics of atomic frequency standards. *Proc. IEEE*, 54:221–230, 1966.
- [81] J. A. Barnes, A. R. Chi, L. S. Cutler, D. J. Haeley, D. B. Leeson, T. E. McGuigan, J. A. Mullan, W. L. Smith, R. L. Sydnor, R. F. C. Vessot, and G. M. R. Winkler. Characterization of frequency stability. *IEEE Trans. Instrum. Meas.*, IM-20:105–120, 1971.
- [82] J. Rutman. Characterization of phase and frequency instabilities in precision frequency sources: Fifteen years of progress. *Proceedings of the IEEE*, 66(9):1048–1075, Sept. 1978.
- [83] C. Schuck. *in preparation*. PhD thesis, ICFO - The institute of photonic Science, 2009.
- [84] M. Almendros. *in preparation*. PhD thesis, ICFO - The institute of photonic Science, 2009.
- [85] J. Eschner, Ch. Raab, F. Schmidt-Kaler, and R. Blatt. Light interference from single atoms and their mirror images. *Nature*, 413:495–498, 2001.
- [86] J. Javanainen and S. Stenholm. Laser cooling of trapped particles iii: The lamb-dicke limit. *Applied Physics A*, 24:151–162, 1981.
- [87] W. Neuhauser, M. Hohenstatt, P. Toschek, and H. Dehmelt. Optical-sideband cooling of visible atom cloud confined in parabolic well. *Phys. Rev. Lett.*, 41(4):233–236, Jul 1978.
- [88] S. Gerber, D. Rotter, M. Hennrich, R. Blatt, F. Rohde, C. Schuck, M. Almendros, R. Gehr, F. Dubin, and J. Eschner. Quantum interference from remotely trapped ions. *New J. Phys.*, 11(1):013032 (13pp), 2009.
- [89] D. Rotter. Photoionisation von kalzium. Master's thesis, Leopold-Franzens-Universität Innsbruck, 2003.
- [90] W. W. Macalpine and R. O. Schildknecht. Coaxial resonators with helical inner conductor. *Proc. IEEE*, 47:2099–2105, 1959.
- [91] Gerthsen and Vogel. *Physik*. Springer, 17. edition, 1993.
- [92] D. E. Browne, M. B. Plenio, and S. F. Huelga. Robust creation of entanglement between ions in spatially separate cavities. *Phys. Rev. Lett.*, 91(6):067901, Aug 2003.
- [93] W. Demtröder. *Laser Spektroskopie*. Springer, 1993.
- [94] R. V. Pound. Electronic frequency stabilization of microwave oscillators. *Review of Scientific Instruments*, 17(11):490–505, 1946.

Bibliography

- [95] R.W.P. Drever and J.L. Hall. Laser phase and frequency stabilisation using an optical resonator. *Applied Physics B*, 31:97, 1983.
- [96] G.C. Bjorklund, M.D. Levenson, W. Lenth, and C. Ortiz. Frequency modulation (fm) spectroscopy. *Applied Physics B*, 32:145–152, 1983.
- [97] D. A. Steck. Cesium d line data. <http://steck.us/alkalidata>, 1998.
- [98] M. Alloing. Frequency stabilization of a 732 nm diode laser. Master thesis, ICFO, August 2008.
- [99] C. Raab, J. Bolle, H. Oberst, J. Eschner, F. Schmidt-Kaler, and R. Blatt. Diode laser spectrometer at 493 nm for single trapped ba+ ions. *Appl. Phys. B*, 67:683–688, 1998.
- [100] E. Riedle, S. H. Ashworth, Jr. J. T. Farrell, and D. J. Nesbitt. Stabilization and precise calibration of a continuous-wave difference frequency spectrometer by use of a simple transfer cavity. *Review of Scientific Instruments*, 65(1):42–48, 1994.
- [101] Metrology toolbox. <http://emtoolbox.nist.gov/Main/Main.asp>.
- [102] B. Edlén. The refractive index of air. *Metrologia*, 2:71, 1966.
- [103] P. T. Pham and P. Schindler. Pulse programmer. <http://pulse-programmer.org/index.php>.
- [104] T. Meyrath and F. Schreck. A laboratory control system for cold atom experiments. <http://george.ph.utexas.edu/control/>.
- [105] Eric D. Black. An introduction to pound–drever–hall laser frequency stabilization. *American Journal of Physics*, 69(1):79–87, 2001.
- [106] A. Banerjee, D. Das, and V. Natarajan. Precise frequency measurements of atomic transitions by use of a rb-stabilized resonator. *Opt. Lett.*, 28(17):1579–1581, 2003.
- [107] Daniel A. Steck. Rubidium 87 d line data. <http://steck.us/alkalidata>, 2008.
- [108] Daniel A. Steck. Rubidium 85 d line data. <http://steck.us/alkalidata>, 2008.
- [109] G. Thalhammer. Frequenzstabilisierung von diodenlasern bei 850, 854 und 866 nm mit linienbreiten im khz bereich. Master’s thesis, Institut für Experimentalphysik, Leopold-Franzens-Universität Innsbruck, 1999.
- [110] K. Matsubara, S. Uetake, H. Ito, Y. Li, K. Hayasaka, and M. Hosokawa. Precise frequency-drift measurement of extended-cavity diode laser stabilized with scanning transfer cavity. *Japanese Journal of Applied Physics*, 44(1A):229–230, 2005.

- [111] A. Banerjee, D. Das, and V. Natarajan. Absolute frequency measurements of the d1 lines in 39k, 85rb, and 87rb with 0.1 ppb uncertainty. *Europhys. Lett.*, 65:172, 2004.
- [112] G. P. Barwood, P. Gill, and W. R. C. Rowley. Frequency measurements on optically narrowed rb-stabilised laser diodes at 780 nm and 795 nm. *Applied Physics B*, 53:142–147, 1991.
- [113] M. Maric, J. J. McFerran, and A. N. Luiten. Frequency-comb spectroscopy of the d1 line in laser-cooled rubidium. *Physical Review A*, 77(3):032502, 2008.
- [114] R. Loudon. *The Quantum Theory of Light*. Oxford University Press, 2000.
- [115] C. C. Tannoudji, J. Dupont-Roc, and G. Grynberg. *Atom-Photon Interaction*. Wiley-Interscience, 1998.
- [116] J. Benhelm, G. Kirchmair, C. F. Roos, and R. Blatt. Experimental quantum-information processing with $^{43}\text{ca}^+$ ions. *Physical Review A (Atomic, Molecular, and Optical Physics)*, 77(6):062306, 2008.
- [117] S.-S. Liaw. Ab initio calculation of the lifetimes of 4p and 3d levels of ca^+ . *Phys. Rev. A*, 51(3):R1723–R1726, Mar 1995.
- [118] C. Cohen-Tannoudji, B. Diu, and F. Laloë. *Quantum Mechanics, volume 2*. John Wiley & sons, 1977.
- [119] H. Oberst. Resonance fluorescence of single barium ions. Master's thesis, Institut für Experimentalphysik, Leopold-Franzens-Universität Innsbruck, 1999.
- [120] L. Mandel and E. Wolf. *Optical Coherence and Quantum Optics*. Cambridge University Press, 1995.
- [121] D. F. Walls and G. J. Milburn. *Quantum Optics*. Springer, 1995.
- [122] M. Lax. *Brandeis University Summer Institute Lectures*, volume 2. Gordon and Breach, New York, 1966.
- [123] D. J. Berkeland, J. D. Miller, J. C. Bergquist, W. M. Itano, and D. J. Wineland. Minimization of ion micromotion in a paul trap. *Journal of Applied Physics*, 83(10):5025–5033, 1998.
- [124] D. Rotter. Private communication.
- [125] T. Young. *Lectures on Natural Philosophy*, volume 1. Johnson, 1807.
- [126] C. K. Hong, Z. Y. Ou, and L. Mandel. Measurement of subpicosecond time intervals between two photons by interference. *Phys. Rev. Lett.*, 59(18):2044–2046, Nov 1987.

Bibliography

- [127] Z. Y. Ou and L. Mandel. Violation of bell's inequality and classical probability in a two-photon correlation experiment. *Phys. Rev. Lett.*, 61(1):50–53, Jul 1988.
- [128] D. Bouwmeester, J.-W. Pan, K. Mattle, M. Eibl, H. Weinfurter, and A. Zeilinger. Experimental quantum teleportation. *Nature*, 390:575–579, 1997.
- [129] D. Bouwmeester, J.-W. Pan, M. Daniell, H. Weinfurter, and A. Zeilinger. Observation of three-photon greenberger-horne-zeilinger entanglement. *Phys. Rev. Lett.*, 82(7):1345–1349, Feb 1999.
- [130] J.-W. Pan, D. Bouwmeester, M. Daniel, and A. Weinfurter, H. and Zeilinger. Experimental test of quantum nonlocality in three-photon greenberger-horne-zeilinger entanglement. *Nature*, 403:515–519, 2000.
- [131] E. Knill, R. Laflamme, and G. J. Milburn. A scheme for efficient quantum computing with linear optics. *Nature*, 409:46–52, 2001.
- [132] D. Fattal, E. Diamanti, K. Inoue, and Y. Yamamoto. Quantum teleportation with a quantum dot single photon source. *Phys. Rev. Lett.*, 92(3):037904, Jan 2004.
- [133] J. I. Cirac, P. Zoller, H. J. Kimble, and H. Mabuchi. Quantum state transfer and entanglement distribution among distant nodes in a quantum network. *Phys. Rev. Lett.*, 78(16):3221–3224, Apr 1997.
- [134] T. Wilk, S. C. Webster, A. Kuhn, and G. Rempe. Single-atom single-photon quantum interface. *Science*, 317(5837):488–490, 2007.
- [135] T. Legero, T. Wilk, A. Kuhn, and G. Rempe. Time-resolved two-photon quantum interference. *Appl. Phys. B*, 77, 8, 2003.
- [136] S. Nussmann, M. Hijlkema, B. Weber, F. Rohde, G. Rempe, and A. Kuhn. Submicron positioning of single atoms in a microcavity. *Physical Review Letters*, 95(17):173602, 2005.
- [137] Barak Dayan, A. S. Parkins, Takao Aoki, E. P. Ostby, K. J. Vahala, and H. J. Kimble. A Photon Turnstile Dynamically Regulated by One Atom. *Science*, 319(5866):1062–1065, 2008.
- [138] A. D. Boozer, A. Boca, R. Miller, T. E. Northup, and H. J. Kimble. Reversible state transfer between light and a single trapped atom. *Physical Review Letters*, 98(19):193601, 2007.
- [139] M. Keller, B. Lange, K. Hayasaka, W. Lange, and H. Walther. Continuous generation of single photons with controlled waveform in an ion-trap cavity system. *Nature*, 431:1075, 2004.

- [140] D. N. Matsukevich, T. Chanelière, M. Bhattacharya, S.-Y. Lan, S. D. Jenkins, T. A. B. Kennedy, and A. Kuzmich. Entanglement of a photon and a collective atomic excitation. *Phys. Rev. Lett.*, 95(4):040405, Jul 2005.
- [141] J. K. Thompson, J. Simon, H. Loh, and V. Vuletic. A high-brightness source of narrowband, identical-photon pairs. *Science*, 313(5783):74–77, 2006.
- [142] J. Beugnon, M. P. A. Jones, J. Dingjan, B. Darquiere, G. Messin, A. Browaeys, and P. Grangier. Quantum interference between two single photons emitted by independently trapped atoms. *Nature*, 440:779, 2006.
- [143] P. Maunz, D. L. Moehring, S. Olmschenk, K. C. Younge, D. N. Matsukevich, and C. Monroe. Quantum interference of photon pairs from two remote trapped atomic ions. *Nat. Phys.*, 3:538, 2007.
- [144] F. Dubin, D. Rotter, M. Mukherjee, S. Gerber, and R. Blatt. Single-ion two-photon source. *Physical Review Letters*, 99(18):183001, 2007.
- [145] U. Eichmann, J. C. Bergquist, J. J. Bollinger, J. M. Gilligan, W. M. Itano, D. J. Wineland, and M. G. Raizen. Young’s interference experiment with light scattered from two atoms. *Phys. Rev. Lett.*, 70(16):2359–2362, Apr 1993.
- [146] U. Dorner and P. Zoller. Laser-driven atoms in half-cavities. *Phys. Rev. A*, 66(2):023816, Aug 2002.
- [147] Z. Y. Ou, Hong C. K., and L. Mandel. Relation between input and output states for a beam splitter. *Optics Com.*, 63:118, 1987.
- [148] C. Skornia, J. von Zanthier, G. S. Agarwal, E. Werner, and H. Walther. Non-classical interference effects in the radiation from coherently driven uncorrelated atoms. *Phys. Rev. A*, 64(6):063801, Nov 2001.
- [149] F. Dubin, D. Rotter, M. Mukherjee, C. Russo, J. Eschner, and R. Blatt. Photon correlation versus interference of single-atom fluorescence in a half-cavity. *Physical Review Letters*, 98(18):183003, 2007.
- [150] M. Schubert, I. Siemers, R. Blatt, W. Neuhauser, and P. E. Toschek. Transient internal dynamics of a multilevel ion. *Phys. Rev. A*, 52(4):2994–3006, Oct 1995.
- [151] D. Deutsch, A. Ekert, R. Jozsa, C. Macchiavello, S. Popescu, and A. Sanpera. Quantum privacy amplification and the security of quantum cryptography over noisy channels. *Phys. Rev. Lett.*, 77(13):2818–2821, Sep 1996.
- [152] H. J. Kimble, M. Dagenais, and L. Mandel. Photon antibunching in resonance fluorescence. *Phys. Rev. Lett.*, 39(11):691–695, Sep 1977.
- [153] F. Diedrich and H. Walther. Nonclassical radiation of a single stored ion. *Phys. Rev. Lett.*, 58(3):203–206, Jan 1987.

- [154] M. Schubert, I. Siemers, R. Blatt, W. Neuhauser, and P. E. Toschek. Photon antibunching and non-poissonian fluorescence of a single three-level ion. *Phys. Rev. Lett.*, 68(20):3016–3019, May 1992.
- [155] M. Jakob and G. Yu. Kryuchkyan. Photon correlation in an ion-trap system. *Phys. Rev. A*, 59(3):2111–2119, Mar 1999.
- [156] V. Gomer, F. Strauch, B. Ueberholz, S. Knappe, and D. Meschede. Single-atom dynamics revealed by photon correlations. *Phys. Rev. A*, 58(3):R1657–R1660, Sep 1998.
- [157] V. Gomer, B. Ueberholz, S. Knappe, F. Strauch, D. Frese, and D. Meschede. Decoding the dynamics of a single trapped atom from photon correlations. *Appl. Phys. B*, 67(6):689–697, 1998.
- [158] F. Carreño, M. A. Antón, and O. G. Calderón. Intensity-intensity correlations in a v-type atom driven by a coherent field in a broadband squeezed vacuum. *Journal of Optics B*, 6(7):315, 2004.
- [159] D. Rotter, M. Mukherjee, F. Dubin, and R. Blatt. Monitoring a single ion’s motion by second-order photon correlations. *New J. Phys.*, 10(4):043011, 2008.
- [160] M. Jakob and J. A. Bergou. Polarization-correlated photon pairs in the fluorescence from a bichromatically driven four-level atom. *J. Opt. B*, 4:308–315, 2002.
- [161] H. J. Kimble. The quantum internet. *Nature*, 453:1023–1030, 2008.
- [162] T. Wilk, S. C. Webster, H. P. Specht, G. Rempe, and A. Kuhn. Polarization-controlled single photons. *Physical Review Letters*, 98(6):063601, 2007.
- [163] M. Hijlkema, B. Weber, H.P. Specht, S.C. Webster, A. Kuhn, and G. Rempe. A single-photon server with just one atom. *Nature Physics*, 3:253–255, 2007.
- [164] A. Haase, N. Piro, J. Eschner, and M. W. Mitchell. Tunable narrowband entangled photon pair source for resonant single-photon single-atom interaction. *Opt. Lett.*, 34(1):55–57, January 2009.
- [165] H.G. Dehmelt. Proposed $10^{14} \delta\nu < \nu$ laser fluorescence spectroscopy on tI^+ mono-ion oscillator ii (spontaneous quantum jumps). *Bull. Am. Phys. Soc.*, 20:60, 1975.
- [166] T. Legero, T. Wilk, A. Kuhn, and G. Rempe. Characterization of single photons using two-photon interference. *arXive:quant-ph/0512023v1*, 2005.
- [167] M. K. Tey, Z. Chen, S. A. Aljunid, B. Chng, F. Huber, G. Maslennikov, and C. Kurtsiefer. Strong interaction between light and a single trapped atom without the need for a cavity. *Nature Physics*, 4:924–927, 2008.

Acknowledgements

The experiments presented in this thesis are the result of a joint effort and the dedication of a team of many people. I'd like to thank everyone who contributed to the success of this work over the past five years. It would not have been possible to make this project come alive without the help of every single one of you.

I thank Jürgen Eschner for taking me onto the adventure of setting up a new experiment in a brand new institute. It was a great experience being one of his first students and helping to build up a new research group. His door was always open and thanks to the great proximity that we all enjoyed with him, I have learned a lot about physics and science.

I'd like to express special gratitude to the people who started the ion trap project together with me and experienced the early days of our group and ICFO. Markus Hennrich was a post-doc with a sheer infinite technical background, who did not leave any theoretical question unanswered either. Although he left us before the achievement of the first results, he played a central role in the success of the experiment. Many thanks to my office mate Carsten Schuck for triggering interesting discussions fostering our precise understanding of the things we did. Special thanks to Marc Almendros who gave me some insight into the world of analog and digital electronics. He build some marvelous devices such as HYDRA and the Cavity Locker, which I hope will not only make history in our research group but also prove useful for others.

Many thanks also to Francois Dubin for joining the experiment at the right moment and for his constant initiative to push us and the experiment forward. He also contributed to the lab-work with drive and enthusiasm and moreover he was able to spice up long night shifts with interesting discussions about non-scientific subjects. The ion traps were built up in collaboration with Daniel Rotter, who also provided the very useful access to the infrastructure in Innsbruck. Thanks a lot!

Albrecht Haase and Nicolas Piro built the SPDC source which is producing wonderful results while I write these lines. Thank you for teaming up with us and working so hard to connect the two experiments. I also enjoyed life outside the lab very much with the two of you.

Thanks to Jan Huwer and Joyee Ghosh for continuing our work. I know the experiment is in good hands with you.

Roger Gehr, Brice Dubost, Mathieu Alloing, Leif Vogel, Stefan Palzer, Daniel Salart and Daniel Lambisto Castro shall be thanked for their help throughout different stages of the experiment.

I wish all the best to the other group members working on the Atom experiment.

Thank you Matteo Cristiani, Tristán Valenzuela and Hannes Gothe for being so patient during our long group meetings and for giving me insight into the neutral atom business.

Thanks to Giovanna Morigi for advice concerning the theoretical part of this thesis and for the fruitful interaction with her group, which culminated in the article together with Stefano Zippilli and Georgina A Olivares-Rentería.

I'd also like to thank my ultimate frisbee team "Patatas Bravas" for having introduced me to this most beautiful of all sports. Your company provided me with lots of pleasure and distraction outside of the lab. I will certainly never forget those wonderful Sunday evenings we spent together chasing a flying plastic disc at the beach in Castelldefels while the sun set over Sitges.

Thanks to my family, especially my parents, for providing me with all the chances I've had in life and my brother who played a big part in my decision to become a physicist.

More than to anyone I owe everything to my love, Stephanie. Thank you for being so loving and supportive especially during difficult times, but also during our many happy moments. I am looking forward to our future.